COMPUTATION OF UNSTEADY VISCOUS INCOMPRESSIBLE FLOW AROUND AN OBLIQUELY OSCILLATING CIRCULAR CYLINDER USING A PARALLELIZED FINITE DIFFERENCE ALGORITHM

KARL P. LAWRENCE

COMPUTATION OF UNSTEADY VISCOUS INCOMPRESSIBLE FLOW AROUND AN OBLIQUELY OSCILLATING CIRCULAR CYLINDER USING A PARALLELIZED FINITE DIFFERENCE ALGORITHM

by

Karl P. Lawrence

SUBMITTED IN PARTIAL FULFILLMENT OF THE
REQUIREMENTS FOR THE DEGREE OF
MASTERS OF SCIENCE (COMPUTATIONAL SCIENCE)
AT
MEMORIAL UNIVERSITY OF NEWFOUNDLAND
ST. JOHN'S, NEWFOUNDLAND
JULY 2004

Your file Votre référence
ISBN: 0-494-02351-1
Our file Notre référence
ISBN: 0-494-02351-1

Table of Contents

List of Tables

List of Figures

Abstract

The objective of the thesis is to numerically investigate the near wake structure and fluid forces generated by a circular cylinder oscillating obliquely in a uniform stream of a viscous incompressible fluid. A numerical series expansion solution valid for small values of the time is used to verify the accuracy of the fully numerical scheme in the initial stages of motion. In this latter scheme, the governing Navier-Stokes equations in vorticity-stream function formulation are solved using a parallelized finite difference algorithm which utilizes global conditions of an integral character. A non-inertial coordinate transformation is used to conformally map the unbounded domain outside the cylinder to a rectangular domain which may be discretized by a set of uniformly spaced grid points. Thus, implicitly, the equations are solved on a time-dependent adaptive mesh. The parallel implementation of the algorithm, which is considered for the first time in this thesis, produces nearly optimal speedup results on 8 processors of a Silicon Graphics Onyx shared memory architecture computer. Numerical simulations are conducted at a Reynolds number of $R = 200$ to first determine fundamental and super-harmonic lock-on ranges. The effect of the amplitude and angle of oscillation on the flow characteristics at several forcing frequencies is then addressed. Whereas inline and transverse oscillations of a circular cylinder have been the focus of many articles, previous work on this problem is limited to a single experimental study by Ongoren and Rockwell (1988b) and three numerical studies by Kocabiyik and Al-Mdallal (2003a,b) and Kocabiyik, Mahfouz, and Al-Mdallal (2004). Therefore, the results of this thesis represent the most comprehensive analysis of the problem to date. Whenever possible, verifications of the method with previous experimental and numerical findings are presented and agreement between the results is excellent.

Acknowledgements

For suggesting this problem, and for her support and patience during my graduate program, I would like to thank Dr. Serpil Kocabiyik. I would also like to thank:

- the computer support staff, Mr. Craig Squires, Mrs. Marian Wissink, Mr. Paul Price, and Mr. Dwayne Hart, of the Computer Science department for their countless hours of assistance;

- Mr. Fred Perry and Mr. Darryl Reid of Memorial University's Computational Visualization Centre for their software, hardware, and programming expertise;

- the administrative and secretarial staff of the Department of Mathematics, Ms. Leonce Morrissey, Ms. Wanda Heath, Ms. Ros English, Ms. Jackie Costello, and Ms. Philomena Kavanagh, for their patience;

- Dr. George Miminis and Mrs. Gail Kenny of the Computational Science Programme for their guidance and support;

- Mr. Qasem Al-Mdallal for his discussions, support, and true friendship.

Funding for this research was provided by the Natural Sciences and Engineering Research Council of Canada (NSERC), the School of Graduate Studies at Memorial University, and Petro Canada.

Nomenclature

a	cylinder radius
$\mathbf{a}$	dimensionless non-inertial acceleration term
A	dimensionless amplitude of oscillation ($= Y_m^*/2a$)
α	dimensionless maximum velocity of oscillations ($= \pi S_f A$)
C_D	dimensionless drag coefficient ($= D/a\rho U^2$)
C_L	lift coefficient ($= L/a\rho U^2$)
D	drag force per unit length
$\mathbf{e}$	unit vector
f	dimensionless oscillation frequency ($= af^*/U$)
S_f	forced Strouhal number ($= 2f$)
f_0	dimensionless natural vortex shedding frequency
S_0	natural Strouhal number ($= 2f_0$)
F_n, f_n	Fourier coefficients for stream function
G_n, g_n	Fourier coefficients scalar vorticity
h_x	spatial discretization step-size (boundary-layer coordinate)
h_ξ	spatial discretization step-size (physical coordinate)
k	boundary-layer parameter
L	lift force per unit length
N	order of truncation in Fourier index
M	number of interior spatial gridpoints
p	dimensionless pressure

p_0	pressure coefficient
R	Reynolds number
r	dimensionless radial coordinate ($= r^*/a$)
$r_{\max}$	dimensionless maximum radial polar gridpoint
S_w	near wake frequency
t	dimensionless time ($= t^*U/a$)
T	period of oscillation ($= 1/f$)
t_c	critical switching time
Δt	dimensionless time step
(x^*, y^*, z^*)	dimensional Cartesian coordinates
x	boundary-layer coordinate
U	uniform flow magnitude
U_m^*	dimensional maximum velocity of oscillation
(u, v)	dimensionless radial and transverse velocity vector components
$\mathbf{v}$	dimensionless velocity vector ($= \mathbf{v}^*/U$)
V	dimensionless harmonic velocity function
Y_m^*	dimensional amplitude of oscillation
Y	dimensionless harmonic displacement function

Greek Symbols

δ	Kronecker delta function
ϵ	iteration tolerance
η	cylinder oscillation angle
ξ	dimensionless logarithmic coordinate ($\ln r$)
ν	kinematic viscosity
θ	angular coordinate
ρ	fluid density

ψ	dimensionless stream function ($= aU\psi^*$)
ϕ	transformation variable
χ	numerical algorithm selection variable ($= x$ or ξ)
ζ	dimensionless negative scalar vorticity

Subscripts

0	cylinder surface
∞	an infinite distance from the surface
$M+1$	grid point approximating ∞
n	Fourier coeffient index
θ_0	angular reference value

Superscripts

$*$	dimensional quantity
m	iteration counter

Chapter 1

The Problem Fundamentals and Mathematical Formulation

1.1 Introduction

Fluid mechanics has served as a rich resource for researchers in search of computationally intense problems over the past few decades. Flow past a circular cylinder is one of many problems included in this extensive repertoire which is dated back to experimental observations almost a century ago by famous physicists/mathematicians like Theodore von Kármán (1911) and Vincent Strouhal (1878). Since then, experimental studies have been conducted (see Griffin and Ramberg (1976), Williamson and Roshko (1988), and Ongoren and Rockwell (1988a,b)) to determine the effect of forcing the cylinder to oscillate in a direction normal and parallel to the flow. With the advent and worldwide distribution of the personal computer, however, these particular cases of cylinder oscillation were computationally simulated using numerical solutions to the governing Navier-Stokes equations, without ever entering an experimental lab. Consequently, many accurate numerical schemes are continuously being developed and applied to these flow problems by Badr and Dennis (1985), Chang and Chern (1991), Sphaier (1991), Menegheni (1993), Nguyen and Kocabiyik (1997), Rengel and Sphaier (1999), Blackburn and Henderson (1999), Anagnostopoulos (2000),

Cetiner and Rockwell (2001), and Stojkovic, Breuer, and Durst (2002) to name a few.

In this thesis, we consider the unsteady flow of a viscous incompressible fluid past a circular cylinder which is forced to oscillate at a prescribed oblique angle η to the positive horizontal axis. The cylinder displacement from the origin is of the form $A\sin(\pi S_f t)$ where A is the amplitude, and S_f is the frequency, of oscillation. In the case of oblique oscillations, the cylinder displacement may be viewed as a combination of a symmetric and asymmetric disturbance to the flow field. Individually, the symmetric and asymmetric disturbances have been studied via streamwise ($\eta = 0°$) and transverse ($\eta = 90°$) oscillations of the cylinder, respectively, as discussed in the review articles of Griffin (1971), Sarpkaya (1979), Griffin and Hall (1991), Hall and Griffin (1993), Matsumoto (1999), and Williamson and Govardhan (2004) and in the representative text on offshore hydrodynamics by Sumer and Fredsøe (1997). Although these two case have been studied extensively, only three numerical studies (Kocabiyik and Al-Mdallal (2003a,b), Kocabiyik, Mahfouz, and Al-Mdallal (2004)) and one experimental study (Ongoren and Rockwell (1988b)) discuss oblique oscillations of a circular cylinder. Therefore, the results which follow in this thesis represent the most comprehensive analysis of the problem to date.

The numerical method used in this thesis is due Professor S . C. R. Dennis and has been used by other researchers over the past 30 years [Collins and Dennis (1973b); Badr and Dennis (1985); Badr, Dennis, and Kocabiyik (1995); Dennis, Nguyen and Kocabiyik (2000)]. A complete discussion of how the spectral finite difference scheme, with implicit Crank-Nicolson time-stepping and Gauss-Seidel iterations, is employed in two distinct zones, is given in this thesis. In the first zone, an appropriate scaling of the dependent variables and an exponentially-spaced adaptive mesh allows us to capture the boundary layer development of the flow. The first stage ends, and the second one begins, at the instant when this scaling is no longer appropriate as suggested from boundary-layer theory. By implementing the scheme in these two separate zones, we

are able to accurately capture the physics of the problem as is suggested by the good agreement with experimental findings. Moreover, due to the sequential process of the Gauss-Seidel iterative scheme which was implemented, parallelization was not considered in any of the previous studies. This thesis addresses the computational efficiency of this method for the first time by investigating the advantages of parallel processing on a Silicon Graphics Onyx shared memory computer consisting of 28 MIPS R12000 processors located in the Computational Visualization Centre at Memorial University. Using the modified algorithm, numerical simulations are conducted for a wide range of parameter values. Throughout this thesis, we fix the Reynolds number at $R = 200$ and vary the three parameters controlling the oscillation to investigate:

(i) the bounds on synchronization regimes as we vary the forcing frequency, $0.3 \leq S_f/S_0 \leq 3.2$, when $A = 0.5$, $\eta = 45°$. Bounds are derived on the various regimes accurate to two-decimal places where possible and admissible vortex shedding modes in the various regions of sub-harmonic, super-harmonic, and fundamental excitation are discussed;

(ii) the effect of intermediate angles of oscillation ($\eta = 15°$, $30°$, $45°$, $60°$, $75°$) on the fluid properties at $A = 0.2$, 0.6, 1.0 and $S_f/S_0 = 0.5$, 1.0, 2.0;

(iii) the effect of increasing the forced oscillation amplitude A on the near wake structure and hydrodynamic forces in conjunction with (ii).

The numerical algorithm, implementation, and verification of results is presented in Chapter 2. The verifications completed in this thesis include numerical and experimental comparisons for (i) the initial flow past an obliquely oscillation cylinder; (ii) uniform flow past a fixed cylinder; (iii) flow past a transversely oscillating cylinder and; (iv) flow past an obliquely oscillating cylinder. It is also noted that we use the Computational Fluid Dynamics (CFD) package FLUENT to verify one case of uniform flow at $R = 500$. The results are in excellent agreement with previous experimental and numerical studies. The modified parallel processing algorithm applied to the

problem is then discussed in Chapter 3. In Chapter 4, we discuss the lock-on phenomenon via a spectral analysis of the lift coefficient for a particular instance of the flow parameters. Then, the effect of the amplitude and angle of oscillation on the near wake structure and force coefficients is discussed in Chapter 5.

1.2 Problem description

The present thesis considers the uniform flow of a viscous incompressible fluid past an infinitely long circular cylinder. The flow is assumed to be unsteady, laminar, and two-dimensional so that the longitudinal axis of the cylinder coincides with the z^*-axis of the cartesian coordinate system. The constant two-dimensional cross-section of the

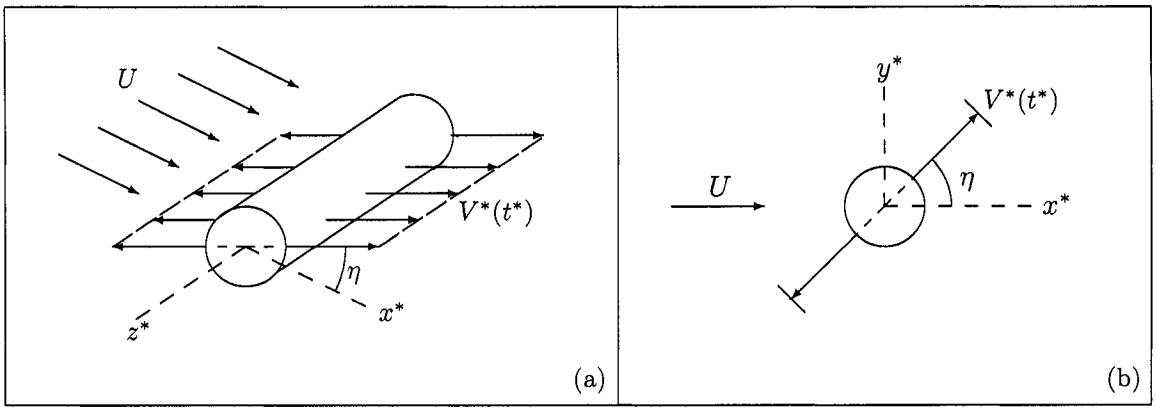

Figure 1.1: (a) Three-dimensional view of problem configuration; (b) Cross-sectional view of problem configuration

rigid cylinder is represented by the circle of radius a in the (x^*, y^*)-plane. We assume that the cylinder is initially at rest in a uniform flow with velocity U and then, at $t^* = 0$, the cylinder is abruptly forced to perform harmonic translational oscillations about an axis which forms an angle of η with the positive x^*-axis as shown in Figure 1.1. The simple harmonic motion of the cylinder is represented by

$$Y^*(t^*) = Y_m^* \sin(2\pi f^* t^*) \tag{1.2.1}$$

where Y_m^* is the maximum displacement of the oscillatory motion measured from the original position of the center of the cylinder at the origin, and f^* is the frequency of the forced oscillation. Since the cylinder is oscillated sinusoidally in time t^* at forcing frequency f^*, the dimensional translational cylinder velocity is expressed as

$$V^*(t^*) = \frac{d}{dt^*}\left[Y^*(t^*)\right] = U_m^* \cos(2\pi f^* t^*) \tag{1.2.2}$$

where $U_m^* = 2\pi f^* Y_m^*$ is the maximum dimensional oscillatory velocity.

1.3 The governing equations and boundary conditions

The equations describing the motion of a viscous incompressible fluid are the well-known Navier-Stokes equations and can be obtained by considering the forces acting on a fluid particle and applying Newton's Laws. The two-dimensional governing equations for unsteady flow are

$$\frac{\partial \mathbf{v}^*}{\partial t^*} + (\mathbf{v}^* \cdot \nabla)\mathbf{v}^* = -\frac{1}{\rho}\nabla p^* + \nu \nabla^2 \mathbf{v}^* + \mathbf{a}^*, \tag{1.3.1}$$

$$\nabla \cdot \mathbf{v}^* = 0 \tag{1.3.2}$$

in polar (r^*, θ) coordinates where $\nabla = \left(\frac{\partial}{\partial r^*}, \frac{1}{r^*}\frac{\partial}{\partial \theta}\right)$, $\mathbf{v}^*$ is the dimensional velocity vector in the non-inertial frame of reference defined in terms of the unit vectors as

$$\mathbf{v}^* = u^*\, \mathbf{e}_{r^*} + v^*\, \mathbf{e}_\theta + (0)\, \mathbf{e}_{z^*} = (u^*,\ v^*,\ 0),$$

p^* is the pressure, and ρ and ν are the density and coefficient of kinematic viscosity of the fluid. The acceleration term

$$\mathbf{a}^* = \begin{bmatrix} a_r^* \\ a_\theta^* \end{bmatrix} = \begin{bmatrix} \dot{V}^*(t^*)\cos(\eta)\cos(\theta) + \dot{V}^*(t^*)\sin(\eta)\sin(\theta) \\ -\dot{V}^*(t^*)\cos(\eta)\sin(\theta) + \dot{V}^*(t^*)\sin(\eta)\cos(\theta) \end{bmatrix} \tag{1.3.3}$$

in (1.3.1) enters as a result of the non-inertial frame of reference employed and the dot in (1.3.3) indicates differentiation with respect to the dimensional time t^*. In

Appendix A the transformation of the governing equations from the non-inertial to inertial frames of reference is summarized. We now define a group of dimensionless variables given by

$$\mathbf{v} = \frac{\mathbf{v}^*}{U}, \qquad p = \frac{p^*}{\frac{1}{2}\rho U^2}, \qquad t = \frac{Ut^*}{a}, \qquad r = \frac{r^*}{a}, \qquad R = \frac{2Ua}{\nu}$$

where R is the Reynolds number and a is the cylinder radius. Equations (1.3.1) and (1.3.2) are then

$$\frac{\partial \mathbf{v}}{\partial t} + (\mathbf{v}\cdot\nabla)\mathbf{v} = -\frac{1}{2}\nabla p + \frac{2}{R}\nabla^2\mathbf{v} + \mathbf{a}, \tag{1.3.4}$$

$$\nabla\cdot\mathbf{v} = 0 \tag{1.3.5}$$

where

$$\mathbf{a} = \begin{bmatrix} a_r \\ a_\theta \end{bmatrix} \begin{bmatrix} \dot{V}(t)\cos(\eta)\cos(\theta) + \dot{V}(t)\sin(\eta)\sin(\theta) \\ -\dot{V}(t)\cos(\eta)\sin(\theta) + \dot{V}(t)\sin(\eta)\cos(\theta) \end{bmatrix}. \tag{1.3.6}$$

In this thesis, the dimensionless harmonic oscillatory velocity is given by

$$\begin{aligned} V(t) &= \pi A S_f \cos(\pi S_f t) \\ &= \alpha\cos(\pi S_f t), \end{aligned} \tag{1.3.7}$$

where α is the dimensionless maximum oscillatory velocity, and S_f and A are the dimensionless forcing frequency and amplitude of oscillation, respectively, defined as

$$S_f = 2af^*/U \text{ and } A = Y_m^*/a. \tag{1.3.8}$$

Consequently, the period of cylinder oscillation, T, may be calculated from $T = 2/S_f$. The nature of the flow is characterized by a set of four dimensionless parameters: R, S_f, A, and η. Equations (1.3.4) and (1.3.5) are the momentum and conservation of mass equations, respectively. In this thesis, the governing equations are expressed in terms of the dimensionless stream function ψ and (negative) vorticity ζ defined as

$$u = e^{-\xi}\frac{\partial\psi}{\partial\theta}, \qquad v = -e^{-\xi}\frac{\partial\psi}{\partial\xi}. \tag{1.3.9}$$

$$\zeta(\xi,\theta,t) = e^{-\xi}\left(\frac{\partial u}{\partial\theta} - \frac{\partial v}{\partial\xi} - v\right), \tag{1.3.10}$$

in modified polar coordinates (ξ, θ) where $r = e^{\xi}$, with the dimensional stream function and vorticity given by

$$\psi^* = a\,U\,\psi \quad \text{and} \quad \zeta^* = -\frac{U\,\zeta}{a}.$$

The stream function defined in (1.3.9) is introduced so that the continuity equation is satisfied. Then taking the curl of the momentum equation (1.3.4) and introducing ψ and ζ we obtain

$$e^{2\xi}\left(\frac{\partial \zeta}{\partial t}\right) = \frac{2}{R}\left(\frac{\partial^2 \zeta}{\partial \xi^2} + \frac{\partial^2 \zeta}{\partial \theta^2}\right) + \frac{\partial \psi}{\partial \xi}\frac{\partial \zeta}{\partial \theta} - \frac{\partial \psi}{\partial \theta}\frac{\partial \zeta}{\partial \xi}, \tag{1.3.11}$$

$$\frac{\partial^2 \psi}{\partial \xi^2} + \frac{\partial^2 \psi}{\partial \theta^2} = e^{2\xi}\zeta. \tag{1.3.12}$$

It is noted that when performing the curl operation on (1.3.4), to eliminate the pressure gradient term ∇p, the acceleration term $\mathbf{a}$ also vanishes since this term is completely confined to the two-dimensional (r, θ)-plane and independent of the z-coordinate.

We are now in a position to discuss boundary conditions for ψ and ζ. The no-slip and impermeability conditions to be implemented on the cylinder surface are given by

$$\psi = \frac{\partial \psi}{\partial \xi} = 0 \quad \text{when} \quad \xi = 0, \tag{1.3.13}$$

and the condition that the velocity approaches uniform flow at large distances from the cylinder, which takes a more complicated form due to the use of the non-inertial frame of reference, is

$$\frac{\partial \psi}{\partial \theta} \to (1 + V(t)\cos(\eta))\cos(\theta) + V(t)\sin(\eta)\sin(\theta) \tag{1.3.14a}$$

$$\text{as } \xi \to \infty.$$

$$\frac{\partial \psi}{\partial \xi} \to (1 + V(t)\cos(\eta))\sin(\theta) - V(t)\sin(\eta)\cos(\theta) \tag{1.3.14b}$$

Implicit in (1.3.14) using (1.3.12) is that

$$\zeta(\xi, \theta, t) \to 0 \text{ as } \xi \to \infty. \tag{1.3.15}$$

In addition, ψ and ζ must be periodic in θ with period 2π as a result of the coordinate system employed, and thus

$$\psi(\xi,\theta,t) = \psi(\xi,\theta+2\pi,t), \quad \zeta(\xi,\theta,t) = \zeta(\xi,\theta+2\pi,t). \tag{1.3.16}$$

It is noted that the conformal transformation

$$x + iy = e^{\xi+i\theta} \tag{1.3.17}$$

maps the surface of the circular cylinder to the contour $\xi = 0$, and the region outside the cylinder, $r > 0$, $0 \leq \theta \leq 2\pi$ to the semi-infinite rectangular domain $\xi > 0$, $0 \leq \theta \leq 2\pi$. The transformed domain is advantageous in numerical work since it can be discretized using a set of horizontal and vertical lines. The intersection of these lines represent the grid points at which numerical solutions are desired, as illustrated in Figure 1.2. The set of conditions (1.3.13)-(1.3.16) must be satisfied for all $t > 0$

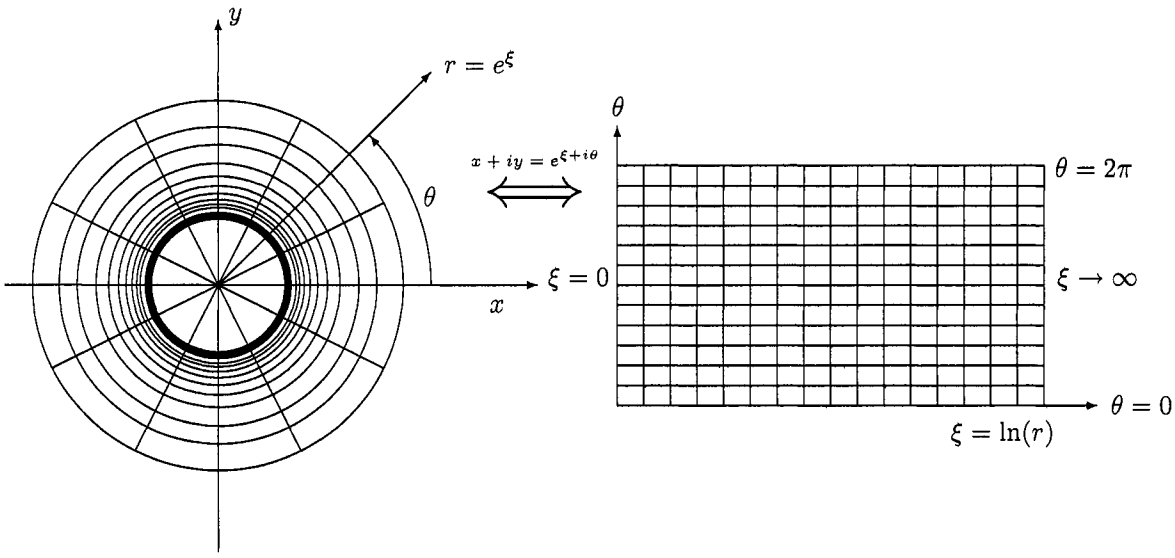

Figure 1.2: Coordinate transformation

and everywhere in the flow domain D given by

$$D = \{(\xi,\theta) : \ 0 \leq \xi < \infty, \ 0 \leq \theta \leq 2\pi\}.$$

By inspecting the boundary conditions we see that there are two conditions for the stream function on the cylinder surface and none for the vorticity. In this thesis this

situation shall be handled using integral conditions for the vorticity, following the work of Dennis and Quartepelle (1989), in which a set of global integral conditions

$$\int_0^{\infty}\int_0^{2\pi} e^{2\xi}\,\zeta\,d\theta\,d\xi = 0, \tag{1.3.18}$$

$$\int_0^{\infty}\int_0^{2\pi} e^{(2-n)\xi}\,\zeta\cos n\theta\,d\theta\,d\xi = -2\pi\,V(t)\,\sin\eta\,\delta_{n,1}, \tag{1.3.19}$$

$$\int_0^{\infty}\int_0^{2\pi} e^{(2-n)\xi}\,\zeta\sin n\theta\,d\theta\,d\xi = 2\pi(1+V(t)\cos\eta)\,\delta_{n,1} \tag{1.3.20}$$

where $\delta_{n,1}$ is the Kronecker delta symbol defined by

$$\delta_{n,1} = 1 \text{ if } n = 1 \quad \delta_{n,1} = 0 \text{ if } n \neq 1.$$

are derived by application of one of Green's identities to the flow domain. It is noted that for symmetric flow problems when $\eta = 0°$ the set of integral conditions (1.3.18)-(1.3.20) reduce to (1.3.20) depending on the motion [Collins and Dennis (1973a,b), Badr, Dennis and Kocabiyik (1995; 1996)]. The use of integral conditions in asymmetric flow cases can also be found in the works of Nguyen and Kocabiyik (1997) and Kocabiyik and Nguyen (1999) in which the case of a circular cylinder under rectilinear oscillations in a transverse direction ($\eta = 90°$) to that of the uniform stream is considered. Because of the oblique oscillations ($0° < \eta < 90°$) of the cylinder, in this thesis, these conditions (1.3.18)-(1.3.20) differ from those previously used by Nguyen and Kocabiyik (1997), Kocabiyik and Nguyen (1999).

1.4 Problem background and motivation

The problem of uniform flow past a fixed circular cylinder has been studied extensively since the pioneering work of von Kármán (1911) due to its simple geometry. The formation of the Kármán vortex street in the wake of a circular cylinder, in which vortices are shed to the rear of the cylinder and persist in the wake as shown in Figure 1.3, has been a subject in the study of flow separation for the last 93 years. The persistence of these vortices in the wake causes pressure fluctuations and struc-

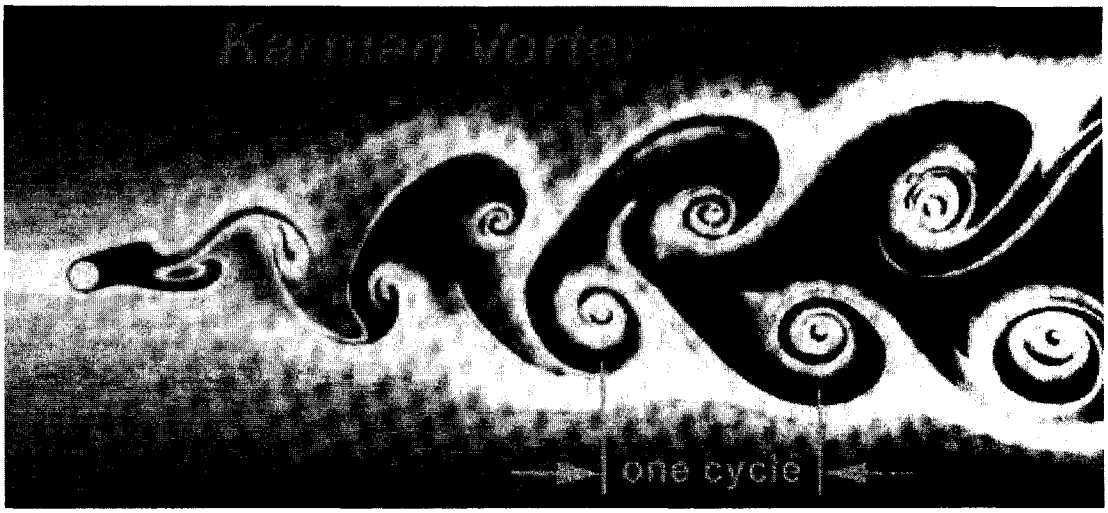

Figure 1.3: Depiction of Kármán vortex street past circular cylinder for $R =$ as shown by Irvine (2003).

tural vibrations which could severely damage engineering structures, or alternatively, could be used to enhance heat/mass transfer or to augment mixing, depending on the application.

This classical fluid mechanics problem is dependent solely on the value of the Reynolds number R, in the case of uniform flow, as summarized by Panton (1984). Below a Reynolds number of about $R \approx 40$, the cylinder wake is stable and thus vortex shedding is not present. The vortices have formed in the separated layer but remain attached to the cylinder surface. As the Reynolds number increases, however, there is a transition from a stable two-dimensional wake to a turbulent three-dimensional wake. From a Reynolds number of $R \approx 40$ to $R \approx 60$ there is a transition from the formation of the attached eddies, to the shedding of vortices from alternate sides of the circular cylinder, creating a Kármán vortex street in the far wake. The dimensionless frequency at which these vortices are shed, denoted $f_0 = af_0^*/U$, is referred to as the natural shedding frequency. When scaled by a factor of 2, to be consistent with the definition of the Strouhal number in (1.3.8), the natural shedding frequency

is $S_0 = 2af_0^*/U$. At $R \approx 190$, spanwise vortices start to develop in the far wake leading to a three dimensional effects as noted by Henderson (1997). As we increase the Reynolds number to $R \approx 200$, the first sign of turbulence appears in the downstream wake as a result of the onset of three-dimensionality. However, forcing the cylinder to oscillate within the flowing fluid is a form of wake control which suppresses some of these instabilities, leading to accurate numerical results for this problem using the present idealized two-dimensional model.

When a cylinder is forced to oscillate, the cylinder vibration and vortex shedding frequencies are the same under certain conditions. This resonance is referred to as lock-on or synchronization and has been observed both experimentally and numerically for streamwise [Armstrong, Barnes and Grant (1986, 1987), Barbi, Favier, Maresca and Telionis (1986), Griffin and Ramberg (1976)] and cross-flow oscillations [Koopman (1967), Griffin and Ramberg (1974), Ongoren and Rockwell (1988a)]. For streamwise oscillations, lock-on is observed when the forcing frequency is approximately twice the natural shedding frequency ($S_f \sim 2S_0$) since the calculated in-line drag force is parallel to the flow direction while for cross-flow oscillations the fundamental lock-on regime is at the natural shedding frequency ($S_f \sim S_0$). In these frequency ranges the near wake characteristics are modified dramatically. For frequencies less than S_0 (or $2S_0$ for the streamwise case), the longitudinal spacing of the vortices in the near wake expand, whereas for $S_f > S_0$, the spacing contracts. Further, increasing the amplitude of oscillation reduces the lateral spacing of the shed vortices until the vortices being shed from the upper and bottom portions of the cylinder are aligned laterally. Drastic shortening of the vortex formation length with increasing amplitude, which causes a faster generation of vorticity from the cylinder surface and lift enhancement, is also observed.

For a fixed amplitude, the different frequency excitation regimes are classified in terms of the ratio of the forcing frequency S_f to natural shedding frequency S_0 as

discussed by Krishnamoorthy, Price and Paidoussis (2001). The fundamental excitation regime is described as the region for which the forcing-to-natural frequency ratio, S_f/S_0, is at or about 1.0. However, lock-on may not occur if a strong competition between the natural and forcing frequencies cause irregular (non-periodic) vortex shedding and hydrodynamic force patterns as is the case for streamwise oscillations. Further, sub-harmonic and super-harmonic excitation regimes occur in regions at or about fractional and integer values of the natural shedding frequency, respectively. If lock-on occurs in one of these regions, then it is referred to as a lock-on regime instead of just an excitation regime. Common sub-harmonic regimes are the $\frac{1}{2}$- and $\frac{1}{3}$-subharmonic ($S_f/S_0 = 1/2,\ 1/3$) regimes and common super-harmonic regimes are the 2- and 3-superharmonic ($S_f/S_0 = 2, 3$). Evidence of these lock-on regimes in the near wake will appear in the spectra of the hydrodynamic forces and vortex shedding patterns.

One of the major characteristics addressed in this thesis is the shedding patterns which develop in the near wake summarized in terms of several asymmetric modes of vortex formation shown in Figure 1.4. In this figure, S indicates 'single' and P indicates 'pair'. Mode 2S depicted in Figure 1.4 is characterized by a single vortex of opposite rotation being alternately shed from each side of the cylinder over a single vortex shedding cycle; 2P means two vortices are alternately shed from each side of the cylinder per cycle; and mode P+S means two vortices are shed from one side of the cylinder and one vortex is shed from the other side over one cycle. The time interval required to complete one cycle of vortex shedding is recorded in terms of multiples/fractions of the cylinder oscillation frequency as pT where p is a rational number.

To our knowledge Ongoren and Rockwell (1988b), in an experimental work, were the only researchers to investigate oblique oscillations of a circular cylinder with

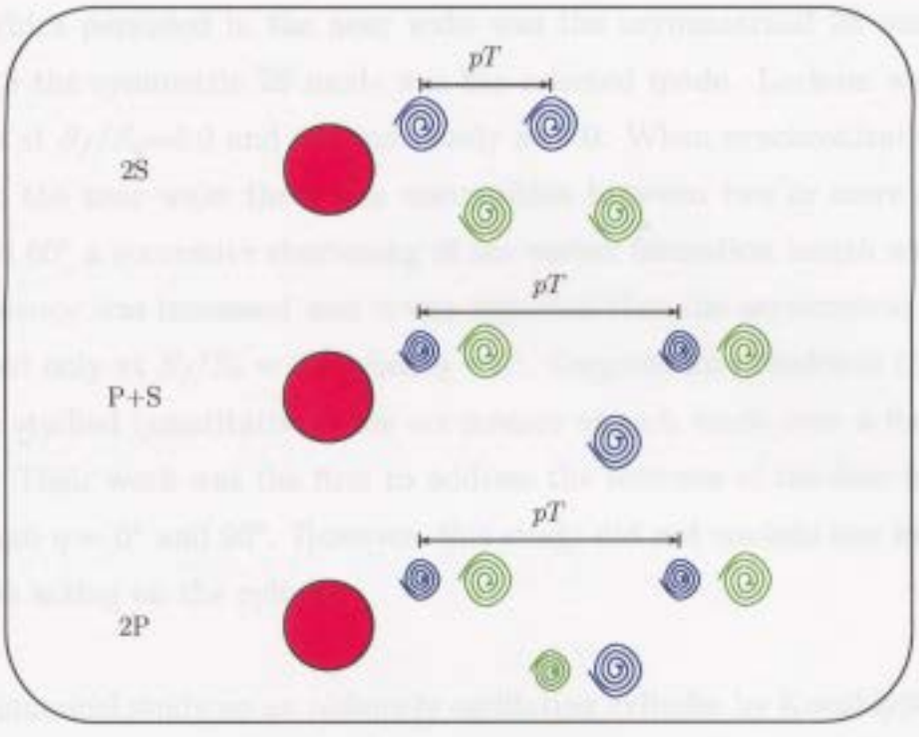

Figure 1.4: Summary of modes of vortex formation.

an oncoming uniform stream. They conducted experiments in a water channel using the hydrogen bubble technique to visualize the formations in near wake for $0.5 \leq S_f/S_0 \leq 4.0$, $A = 0.26$, and $855 \leq R \leq 1300$ with $0° \leq \eta \leq 90°$. A comprehensive study of streamwise ($\eta = 0°$) oscillations is presented in which symmetric and asymmetric modes of vortex formation were observed. For lower frequencies, the near wake structure developed from 2S at S_f/S_0=0.5 and 1.0 to the P+S mode at $S_f/S_0 = 2.0$. For increasing frequency $S_f/S_0 = 3.0$, 4.0, the shedding of the vortices in the near wake becomes symmetric due to the increased velocity of the cylinder resulting in a symmetric 2S mode in which single counter-rotating vortices are shed from the top and bottom of the cylinder at the same instant. At $S_f/S_0 = 3.0$, this arrangement of shedding persists in the downstream direction for up to three vortex pairs. Ongoren and Rockwell (1988b) then choose intermediate angles of forced oscillation as $\eta = 45°$ and 60° which introduced simultaneous symmetric and asymmetric perturbations to the flow. For $\eta = 45°$, 60° and $S_f/S_0 \leq 2.0$, the mode of vortex

shedding which persisted in the near wake was the asymmetrical 2S mode and for $S_f/S_0 \geq 2.5$ the symmetric 2S mode was the selected mode. Lock-on was observed in this case at S_f/S_0=3.0 and 4.0 and nearly at 1.0. When synchronization was not observed in the near wake there was competition between two or more modes. At $\eta = 45°$ and 60° a successive shortening of the vortex formation length was observed as the frequency was increased and it was reported that the asymmetric P+S mode was observed only at $S_f/S_0 = 2.0$ when $\eta = 0°$. Ongoren and Rockwell (1988b) continued also studied quantitatively the occurrence of each mode over a fixed number of periods. Their work was the first to address the features of the flow for an angle different than $\eta = 0°$ and 90°. However, this study did not contain any investigation of the forces acting on the cylinder.

The first numerical study on an obliquely oscillating cylinder by Kocabiyik, Mahfouz, and Al-Mdallal (2004) considers small amplitude oscillations $A = 0.2$ at an angle of $\eta = 45°$ and Reynolds number of $R = 500$ when $0.5 \leq S_f/S_0 \leq 4.0$. Other results on this problem have been discussed in two conference proceedings by Kocabiyik and Al-Mdallal (2003a,b). Full results of their work will be published elsewhere. Therefore, this thesis is the most comprehensive numerical study considering oblique oscillations of a circular cylinder to date which was motivated by the lack of literature on the problem.

Chapter 2

Numerical methodology and verification of solution

Numerical techniques for solving flow problems in fluid dynamics have been evolving since the emergence of the digital computer. Finite difference and finite element methods, in particular, have been developed to obtain the numerical solution of the Navier-Stokes equations in the past three decades. However, a fundamental numerical problem arises from the fact that the flow behaves differently in the boundary-layer surrounding, and far away from, the body. In these regions, the flow develops on different scales, and hence different resolutions are required. The aim is to obtain adequate resolution in both regions without wasting computational time and effort. Another major problem lies in implementing the boundary conditions at the surface of, and at large distances from, the cylinder. Mesh refinement, step-sizes, and convergence also, as in all computational studies, limit the numerical solutions.

Finite element schemes have been used by researchers such as Smith and Brebbia (1977), Gresho, Lee and Sani (1980), Eaton (1987), Karniadakis and Triantafyllou (1989), Anagnostopoulos (1989; 1997; 2000), and Herfjord (1995), to study flows past fixed and oscillating cylinders in the presence of a uniform stream. The advantage of this technique is that grid generation near the surface of the cylinder

and refinement are efficient. However, specifying correct boundary conditions with this method is not ideal as it requires further numerical calculations, often involving the pressure distribution, which is one of the most difficult quantities to approximate.

Finite difference schemes have been used by Jordin and Fromm (1972), Collins and Dennis (1973), Swanson and Spaulding (1978), Badr and Dennis (1985), Franke, Rodi and Schoenung (1990), Badr, Dennis and Kocabiyik (1995), Nguyen and Kocabiyik (1997), Kocabiyik and Nguyen (1999), and Dennis, Nguyen and Kocabiyik (2000). Coordinate transformations are required in these schemes to create a computational grid which is fitted to the circular boundaries. In addition, the standard central difference formula, which are commonly used, provide a solution with a best-case second-order accuracy in space. However, finite difference methods usually generate simple sparse matrices which can be solved quickly and efficiently. In addition, other numerical techniques such as evolved iterative procedures and adaptive grid refinement can be coupled with finite difference methods for increased accuracy with minimal effort.

As we mentioned earlier, the numerical method utilized in this thesis was originally used by Professor S.C.R. Dennis and has since been tested for various external flows generated by circular cylinders over the past 30 years. The method is based on a spectral finite-difference approximation of the governing equations with time stepping accomplished using an implicit scheme. Gauss-Seidel iterations are used to improve the numerical solution until a prescribed tolerance is achieved.

This method and its validation for the cases of initial and uniform flow past a circular cylinder, in addition to flow generated by forced oblique oscillations of a circular cylinder, are given in detail in the subsequent sections.

2.1 Method of solution

To exploit the periodicity of the flow domain, the solution procedure used in this study, following the work of Badr and Dennis (1985), begins with a truncated Fourier series expansion of the dependent variables ψ and ζ of the form

$$\psi(\xi,\theta,t) = \frac{1}{2}F_0(\xi,t) + \sum_{n=1}^{N} F_n(\xi,t)\cos(n\theta) + f_n(\xi,t)\sin(n\theta), \tag{2.1.1}$$

$$\zeta(\xi,\theta,t) = \frac{1}{2}G_0(\xi,t) + \sum_{n=1}^{N} G_n(\xi,t)\cos(n\theta) + g_n(\xi,t)\sin(n\theta). \tag{2.1.2}$$

Direct substitution of these expressions into equations (1.3.11) and (1.3.12) yield a set of interdependent ordinary differential equations governing each Fourier mode given by

$$\frac{\partial^2 F_0}{\partial \xi^2} = e^{2\xi}G_0, \qquad \frac{\partial^2 F_n}{\partial \xi^2} - n^2 F_n^2 = e^{2\xi}G_n, \tag{2.1.3}$$

$$\frac{\partial^2 f_n}{\partial \xi^2} - n^2 f_n = e^{2\xi}g_n. \tag{2.1.4}$$

$$e^{2\xi}\frac{\partial G_n}{\partial t} = \frac{2}{R}\left(\frac{\partial^2 G_n}{\partial \xi^2} - n^2 G_n\right) - \frac{1}{2}nf_n\frac{\partial G_0}{\partial \xi} + \frac{1}{2}S_n, \tag{2.1.5}$$

$$e^{2\xi}\frac{\partial g_n}{\partial t} = \frac{2}{R}\left(\frac{\partial^2 g_n}{\partial \xi^2} - n^2 g_n\right) + \frac{1}{2}nF_n\frac{\partial G_0}{\partial \xi} + \frac{1}{2}T_n, \tag{2.1.6}$$

for $n = 1, 2, \ldots, N$ where N is the order of truncation of the Fourier series and $S_n(\xi,t)$ and $T_n(\xi,t)$ are

$$\begin{aligned} S_n = \sum_{m=1}^{\infty} \Bigg[& ((m-n)F_p + qF_q)\frac{\partial g_m}{\partial \xi} - (pf_p + qf_q)\frac{\partial G_m}{\partial \xi} + m\left(\frac{\partial F_p}{\partial \xi} + \frac{\partial F_q}{\partial \xi}\right) g_m \\ & - m\left(\operatorname{sgn}(m-n)\frac{\partial f_p}{\partial \xi} + \frac{\partial f_q}{\partial \xi}\right) G_m \Bigg], \end{aligned}$$

$$\begin{aligned} T_n = \sum_{m=1}^{\infty} \Bigg[& (qf_q - pf_p)\frac{\partial g_m}{\partial \xi} - ((m-n)F_p - qF_q)\frac{\partial G_m}{\partial \xi} - m\left(\frac{\partial F_p}{\partial \xi} - \frac{\partial F_q}{\partial \xi}\right) G_m \\ & - m\left(\operatorname{sgn}(m-n)\frac{\partial f_p}{\partial \xi} - \frac{\partial f_q}{\partial \xi}\right) g_m \Bigg] \end{aligned}$$

with $q = m + n$ and $p = |m - n|$ for $n = 1, 2, ..., N$. Also, the boundary and integral conditions governing the Fourier modes computed from (1.3.13), (1.3.15), and (1.3.18)-(1.3.20) are now

$$F_0(0,t) = F_n(0,t) = f_n(0,t) = 0, \tag{2.1.7}$$

$$\frac{\partial F_0(0,t)}{\partial \xi} = \frac{\partial F_n(0,t)}{\partial \xi} = \frac{\partial f_n(0,t)}{\partial \xi} = 0, \tag{2.1.8}$$

$$G_n,\ g_n \to 0 \ \text{ as } \ \xi \to \infty, \tag{2.1.9}$$

$$\int_0^\infty e^{2\xi}\, G_0\, d\xi = 0, \tag{2.1.10}$$

$$\int_0^\infty e^{(2-n)\xi}\, G_n\, d\xi = -2V(t)\sin\eta\ \delta_{n,1}, \tag{2.1.11}$$

$$\int_0^\infty e^{(2-n)\xi}\, g_n\, d\xi = 2(1 + V(t)\cos\eta)\ \delta_{n,1}. \tag{2.1.12}$$

To this end, we note that the two second-order partial differential equations (1.3.11) and (1.3.12) with conditions (1.3.13), (1.3.15), (1.3.18)-(1.3.20) have been transformed into a set of (4N+2)-ordinary differential equations (2.1.3)-(2.1.6) with conditions (2.1.7)-(2.1.12).

In this thesis, the governing equations and conditions in (2.1.3)-(2.1.12) will be transformed to boundary-layer coordinates (x, θ, t) using

$$\xi = kx \quad \text{with} \quad k = \left(\frac{8t}{R}\right)^{\frac{1}{2}} \tag{2.1.13}$$

which facilitates an implicit stretching of the boundary layer. Here, R is the Reynolds number and k is a small parameter which is of the same order as the thickness of the boundary layer. The choice of 8 as a constant in the definition of k is purely for superficial compactness of the resulting boundary-layer equations. A subsequent scale order analysis of the Fourier coefficients based on this parameter then yields the result that the vorticity components ($G_0(\xi,t)$, $G_n(\xi,t)$, and $g_n(\xi,t)$) are of order $O(k^{-1})$ and the stream function components ($F_0(\xi,t)$, $F_n(\xi,t)$, and $f_n(\xi,t)$) are of

$O(k)$ leading to the introduction of the scaled dependent variables

$$f_n(\xi,t) = kf_n(x,t), \quad F_n(\xi,t) = kF_n(x,t), \quad g_n(\xi,t) = \frac{g_n(x,t)}{k}, \quad G_n(\xi,t) = \frac{G_n(x,t)}{k}, \tag{2.1.14}$$

for $n = 1, 2, 3, ..., N$. Using the above transformations in equations (2.1.3)-(2.1.6) gives

$$\frac{\partial^2 F_0}{\partial x^2} = e^{2kx} G_0, \qquad \frac{\partial^2 F_n}{\partial x^2} - n^2 k^2 F_n = e^{2kx} G_n \tag{2.1.15}$$

$$\frac{\partial^2 f_n}{\partial x^2} - n^2 k^2 f_n = e^{2kx} g_n \tag{2.1.16}$$

and

$$\begin{aligned} 4t\frac{\partial G_n}{\partial t} &= e^{-2kx}\frac{\partial^2 G_n}{\partial x^2} + 2x\frac{\partial G_n}{\partial x} + (2 - n^2k^2e^{-2kx})G_n \\ &\quad -2te^{-2kx}\left(nf_n\frac{\partial G_0}{\partial x} - S_n(x,t)\right), \end{aligned} \tag{2.1.17}$$

$$\begin{aligned} 4t\frac{\partial g_n}{\partial t} &= e^{-2kx}\frac{\partial^2 g_n}{\partial x^2} + 2x\frac{\partial g_n}{\partial x} + (2 - n^2k^2e^{-2kx})g_n \\ &\quad +2te^{-2kx}\left(nF_n\frac{\partial G_0}{\partial x} + T_n(x,t)\right) \end{aligned} \tag{2.1.18}$$

where $S_n(x,t)$ and $T_n(x,t)$ have the same form as before but with the physical spatial ξ-coordinate replaced by the boundary layer spatial x-coordinate. The boundary and integral conditions in the boundary-layer coordinate system remain relatively unchanged and are given by

$$F_0(0,t) = F_n(0,t) = f_n(0,t) = 0, \tag{2.1.19}$$

$$\frac{\partial F_0(0,t)}{\partial x} = \frac{\partial F_n(0,t)}{\partial x} = \frac{\partial f_n(0,t)}{\partial x} = 0, \tag{2.1.20}$$

$$G_0(x,t),\ G_n(x,t),\ g_n(x,t) \to 0, \quad \text{as } x \to \infty \tag{2.1.21}$$

$$\int_0^\infty e^{2kx}\ G_0(x,t)\ dx = 0, \tag{2.1.22}$$

$$\int_0^\infty e^{(2-n)kx}\ G_n(x,t)\ dx = -2V(t)\sin(\eta)\ \delta_{n,1}; \tag{2.1.23}$$

$$\int_0^\infty e^{(2-n)kx}\, g_n(x,t)\, dx = 2(1+V(t)\cos(\eta))\, \delta_{n,1}. \tag{2.1.24}$$

The initial solution at $t = 0$ is obtained, following the work by Collins and Dennis (1973a) and Badr and Dennis (1985), using an exact analysis. This initial condition is given by

$$G_0(x,0) = 0, \tag{2.1.25}$$

$$G_n(x,0) = -4\dot{V}(0)\sin(\eta)\pi^{-\frac{1}{2}}e^{-x^2}\delta_{n,1}, \tag{2.1.26}$$

$$g_n(x,0) = 4\pi^{-\frac{1}{2}}(1+\dot{V}(0)\cos(\eta))e^{-x^2}\delta_{n,1}, \tag{2.1.27}$$

$$F_0(z,0) = 0, \tag{2.1.28}$$

$$F_n(x,0) = -2\dot{V}(0)\sin(\eta)[x\mathrm{erf}(x)+\pi^{-\frac{1}{2}}(e^{-x^2}-1)]\delta_{n,1}, \tag{2.1.29}$$

$$f_n(x,0) = 2(1+\dot{V}(0)\cos(\eta))[x\mathrm{erf}(x)+\pi^{-\frac{1}{2}}(e^{-x^2}-1)]\delta_{n,1}. \tag{2.1.30}$$

2.2 Description of the drag and lift coefficients

The discussion in this thesis will focus greatly on the in-line and transverse forces resulting, fundamentally, from the pressure gradient at the surface of the cylinder, the shear stress acting on it, and the imposed oscillations. In ideal flow, since the pressure distribution over the surface of the cylinder is symmetric about the vertical and horizontal axis, the net force on the body due to the pressure gradient would be zero. We may determine the dimensionless pressure gradient using the angular component of the momentum equation (1.3.4) applied to the surface of the cylinder where the no-slip and impermeability conditions hold to be

$$\frac{\partial p_0}{\partial \theta} = -\frac{4}{R}\left(\frac{\partial \zeta}{\partial \xi}\right)_{\xi=0} + 2a_\theta \tag{2.2.1}$$

where p_0 is the pressure coefficient defined as

$$p_0 = \frac{p^*_{\xi=0} - p^*_{\theta_0}}{\frac{1}{2}\rho U^2}. \tag{2.2.2}$$

Here, $p^*_{\xi=0}$ and $p^*_{\theta_0}$ are the dimensional pressure on the surface of the cylinder with the latter being defined at some reference value θ_0 usually take to be $\theta_0 = 0$ or $\theta_0 = \pi$, and a_θ is the angular component of the resultant acceleration vector in the non-inertial frame of reference given in (1.3.6). Using (2.1.1)-(2.1.2) and integrating (2.2.1) over θ we find the pressure distribution over the surface of the cylinder is

$$\begin{aligned} p_0 \;=\; & \frac{4}{R}\sum_{n=1}^{N}\left[\left.\frac{\partial G_n}{\partial \xi}\right|_{\xi=0}\left(\frac{\sin(n\theta)-\sin(n\theta_0)}{n}\right)+\left.\frac{\partial g_n}{\partial \xi}\right|_{\xi=0}\left(\frac{\cos(n\theta_0)-\cos(n\theta)}{n}\right)\right] \\ & +2\left[\dot{V}(t)\cos(\eta)(\cos(\theta)-\cos(\theta_0))+\dot{V}(t)\sin(\eta)(\sin(\theta)-\sin(\theta_0))\right] \\ & +\frac{2}{R}(\theta-\theta_0)\left.\frac{\partial G_0}{\partial \xi}\right|_{\xi=0}. \end{aligned} \tag{2.2.3}$$

The drag D and lift L per unit length forces are extremely important in the analysis of the vortex formations in the near wake. These forces provide insight into the lock-on phenomenon and mode competition. The lift and drag forces are quantified in terms of the dimensionless drag and lift coefficients expressed as

$$C_D = \frac{D}{\frac{1}{2}\rho U^2} \tag{2.2.4}$$

and

$$C_L = \frac{L}{\frac{1}{2}\rho U^2}, \tag{2.2.5}$$

respectively. In our formulation, these terms may be calculated from

$$C_D = \frac{2}{R}\int_0^{2\pi}\left.\left(\frac{\partial \zeta}{\partial \xi}-\zeta\right)\right|_{\xi=0}\sin(\theta)d\theta - \pi\dot{V}(t)\cos(\eta), \tag{2.2.6}$$

$$C_L = -\frac{2}{R}\int_0^{2\pi}\left.\left(\frac{\partial \zeta}{\partial \xi}-\zeta\right)\right|_{\xi=0}\cos(\theta)d\theta - \pi\dot{V}(t)\sin(\eta) \tag{2.2.7}$$

where the first term in each represents the contribution due to the pressure gradient, the second terms represent the contribution due to the surface stress, the third terms are a direct result of the use of the non-inertial frame of reference. Substituting the Fourier expansions, (2.1.1)-(2.1.2), into these expressions we obtain the total drag and lift coefficients as

$$C_D = \frac{2\pi}{R}\left[g_1(0,t)-\left(\frac{\partial g_1}{\partial \xi}\right)_{\xi=0}\right] - \pi\dot{V}(t)\cos(\eta) \tag{2.2.8}$$

and

$$C_L = \frac{2\pi}{R}\left[\left(\frac{\partial G_1}{\partial \xi}\right)_{\xi=0} - G_1(0,t)\right] - \pi \dot{V}(t)\sin(\eta), \tag{2.2.9}$$

respectively, where we note that the resultant forces are completely determined from a single Fourier mode.

2.3 The numerical solution procedure

The solution procedure used in this thesis, which is essentially a modification of that used by Badr and Dennis (1985), is divided into two stages. The first stage of the numerical solution begins in boundary-layer coordinates (x, θ, t) and uses equations (2.1.15)-(2.1.18) with the associated boundary and initial conditions given by (2.1.19)-(2.1.24) and (2.1.25)-(2.1.30). Solving these equations, we are able to accurately resolve the time development of the boundary-layer in the early stages of motion. However, for finite values of the Reynolds number, as time increases, the boundary-layer parameter k grows at a rate proportional to $t^{1/2}$ which is unrealistic because the corresponding grid size in the physical space grows in proportion to k. Thus, the second stage begins following the first one when the boundary-layer becomes thick enough to use the physical coordinates (ξ, θ, t). At this critical time t_c we switch back to the physical coordinate ξ and continue integration until the final time is reached. The value of t_c, varies with Reynolds number since it determines the location of the outer boundary of the computational domain through the relationship $\xi_{M+1} = kx_{M+1}$.

In the present method, the conformal transformation (1.3.17) is used to generate grid points around a circular cylinder. In particular, (1.3.17) facilitates an exponential stretching in the radial direction, ξ, which clusters nodes near to the surface of the cylinder. The resultant computational domains used in the two stages of the numerical integration scheme consist of $M + 2$ grid points in the radial direction and

are given by

$$x_i = i\,h_x \quad \text{for } i = 0,\ 1,\ ...,\ M+1,$$

in the boundary-layer coordinate system to solve (2.1.15)-(2.1.18) and

$$\xi_i = i\,h_\xi \quad \text{for } i = 0,\ 1,\ ...,\ M+1,$$

in the physical coordinate system to solve (2.1.3)-(2.1.6). During the first integration stage the two coordinate systems are related to one another through $\xi = k(t)x$. The physical-coordinate domain in the second stage is thus determined by specifying the value of the critical time $t = t_c$.

From (2.1.13), it is evident that choosing a uniform spacing h_x in the x-direction corresponds to a uniform spacing which grows in time for ξ since $h_\xi = k(t)\,h_x$. Then, this uniform spacing corresponds to a non-uniform spacing in the radial direction since $r = e^\xi$. The series of graphs in Figure 2.1 displays the time development of the grid mapping from a uniform grid in $0 \leq x \leq x_{M+1}$ (vertical axis) to the non-uniform grid in the dimensionless radial coordinate r (horizontal axis). At the smaller time $t_1 < t_c$, the grid points are clustered near the surface of the cylinder at $r = 1$. In the interval $t \leq t_c$, the computational domain in the non-uniform grid, $1 \leq r \leq r_{\max}$, grows with time while maintaining a fixed number of grid points in exponential spacing. The critical time at which the grid ceases to grow is $t = t_c$. Then, for $t > t_c$, the non-uniform radial grid is fixed about the cylinder for the remainder of the calculations. Figure 2.2 gives the location of the maximum radial grid point as a function of the time. Note, the location of the maximum contour grows until $t = t_c$, at which time the location of the grid point remains fixed. In the calculations, t_c is determined individually for each set of flow parameters but it must satisfy the condition that $k \leq 1$.

The Fourier series expansions of ψ and ζ create a set of interdependent Fourier modes given by $F_0(x,t)$, $F_n(x,t)$, $f_n(x,t)$, $G_0(x,t)$, $G_n(x,t)$, and $g_n(x,t)$. The dependency of each mode suggests that the use of an iterative technique in this problem would

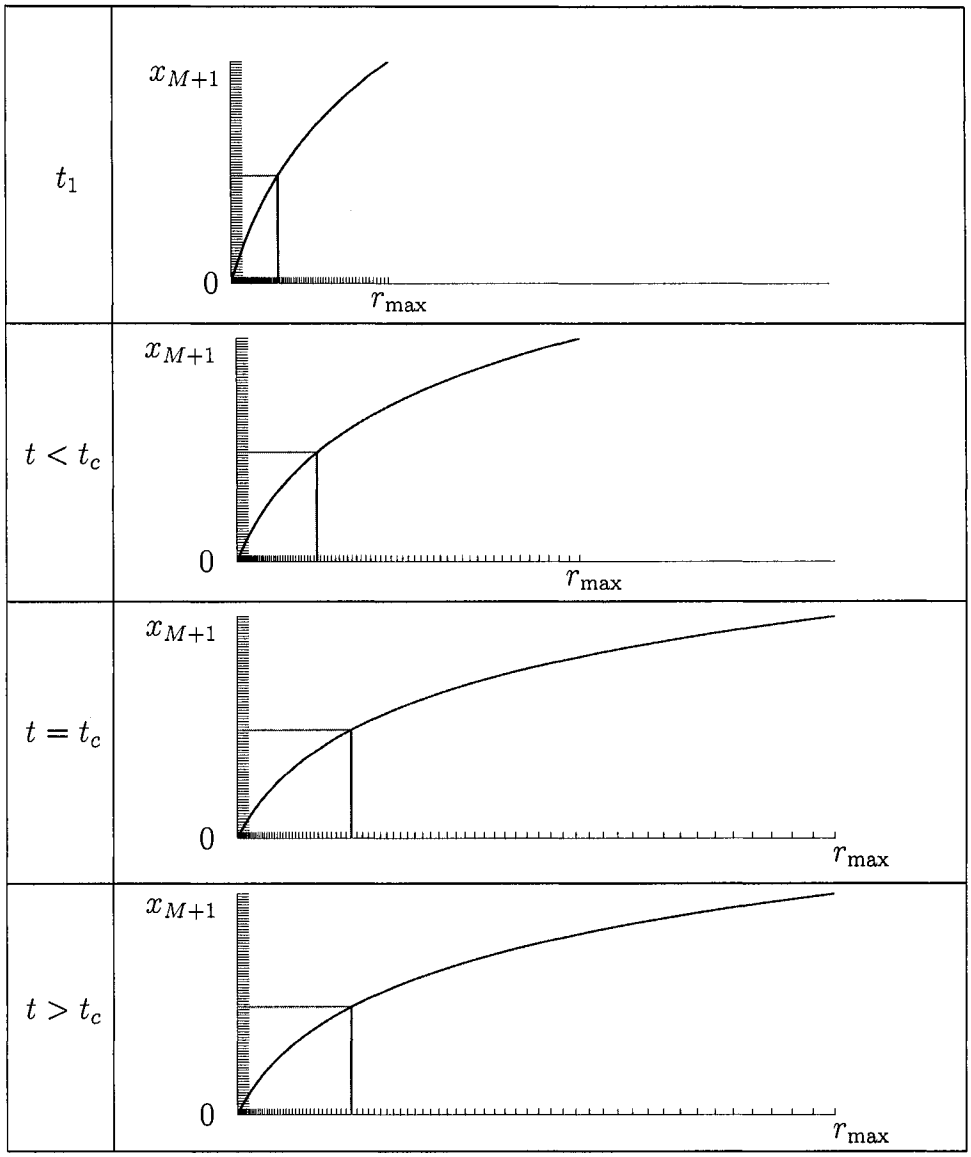

Figure 2.1: Time-development of the grid mapping from the uniform boundary-layer x-discretization to the dimensionless radial r-coordinate

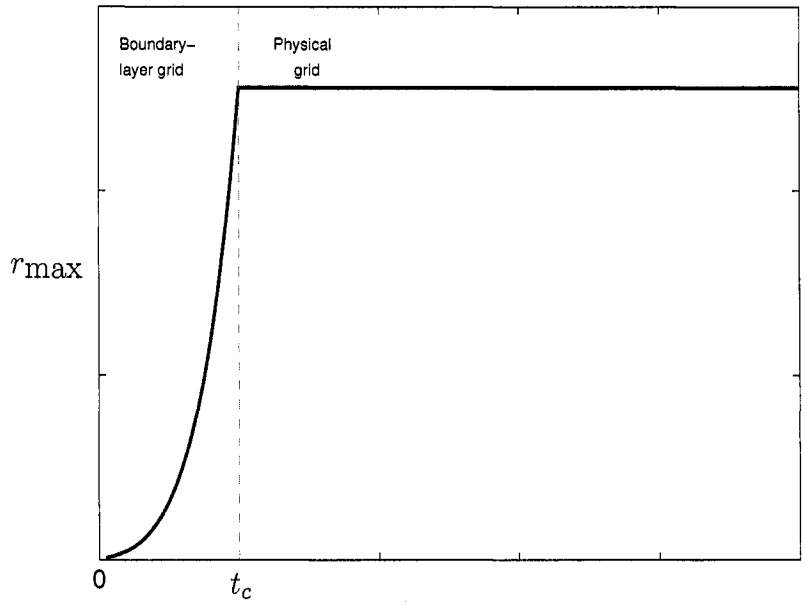

Figure 2.2: Location of outer radial boundary of the computational domain as time progress based on the given coordinate mapping.

be useful to obtain accurate solutions. The iterative method employed in this thesis is based on solving (2.1.15)-(2.1.18) in an implicit manner to achieve convergence criterion of the form

$$\begin{aligned} |G_n^m(x,t) - G_n^{m-1}(x,t)| &\leq 10^{-\epsilon}, \quad n = 0,1,2,...,N, \\ |F_n^m(x,t) - F_n^{m-1}(x,t)| &\leq 10^{-\epsilon}, \quad n = 0,1,2,...,N, \\ |g_n^m(x,t) - g_n^{m-1}(x,t)| &\leq 10^{-\epsilon}, \quad n = 1,2,...,N, \\ |f_n^m(x,t) - f_n^{m-1}(x,t)| &\leq 10^{-\epsilon}, \quad n = 1,2,...,N, \end{aligned} \tag{2.3.1}$$

where m denotes the iteration step and ϵ determines the desired tolerance.

At a particular time t, we assume that each of the Fourier coefficients $F_0(\chi,t)$, $F_n(\chi,t)$, $f_n(\chi,t)$, $G_0(\chi,t)$, $G_n(\chi,t)$, and $g_n(\chi,t)$ are known, where χ is a variable used to distinguish between the two integration stages in boundary-layer and physical coordinates. To advance to the next time step $t+\Delta t$, a computational procedure of the following form is used (assuming that we begin in boundary-layer coordinates, or $\chi = x$):

- Take $\chi = x$, the boundary-layer coordinate. Given the coefficients $F_0(\chi,t)$, $F_n(\chi,t)$, $f_n(\chi,t)$, $G_0(\chi,t)$, $G_n(\chi,t)$, and $g_n(\chi,t)$ at time level t and at the $M+2$ grid points $\chi_i = i\,h_\chi$ for $i = 0,\ 1,\ 2,\ ...,\ M+1$:

1. An initial approximation of the coefficients ($m = 0$) is

$$\begin{aligned} G_0^{m-1}(\chi,t+\Delta t) &= G_0(\chi,t) \quad F_0^{m-1}(\chi,t+\Delta t) &= F_0(\chi,t) \\ G_n^{m-1}(\chi,t+\Delta t) &= G_n(\chi,t) \quad F_n^{m-1}(\chi,t+\Delta t) &= F_n(\chi,t) \\ g_n^{m-1}(\chi,t+\Delta t) &= g_n(\chi,t) \quad f_n^{m-1}(\chi,t+\Delta t) &= f_n(\chi,t) \end{aligned}$$

2. Calculate $G_0^m(\chi,t+\Delta t)$ and $F_0^m(\chi,t+\Delta t)$

3. For $n = 1$ up to N, depending on χ,

   (i) Calculate $G_n^m(\chi,t+\Delta t)$ from $(2.1.17)_{\chi=x}$ or $(2.1.5)_{\chi=\xi}$

   (ii) Calculate $F_n^m(\chi,t+\Delta t)$ from $(2.1.15)_{\chi=x}$ or $(2.1.3)_{\chi=\xi}$

   (iii) Calculate $g_n^m(\chi,t+\Delta t)$ from $(2.1.18)_{\chi=x}$ or $(2.1.6)_{\chi=\xi}$

   (iv) Calculate $f_n^m(\chi,t+\Delta t)$ from $(2.1.16)_{\chi=x}$ or $(2.1.4)_{\chi=\xi}$

5. If convergence criterion (2.3.1) is satisfied go to Step 6, otherwise increment m and repeat Steps 2-5.

6. Increment t to $t = t + \Delta t$. If we have reached the final time, stop. Otherwise, go to Step 7.

7. If $t = t_c$, we switch back to the physical coordinate, $\chi = \xi$, with the grid points determined by $\xi_i = k(t_c)x_i$ for $i = 0$ to $M+1$. Go to Step 1.

This numerical scheme is also shown graphically in Figure 2.3. Despite the two different integration stages, there is an inherent symmetry in the two sets of governing differential equations. Thus, in this section, we will give an outline of the numerical scheme for only one set of vorticity-stream function components in boundary-layer coordinates as to avoid repetition.

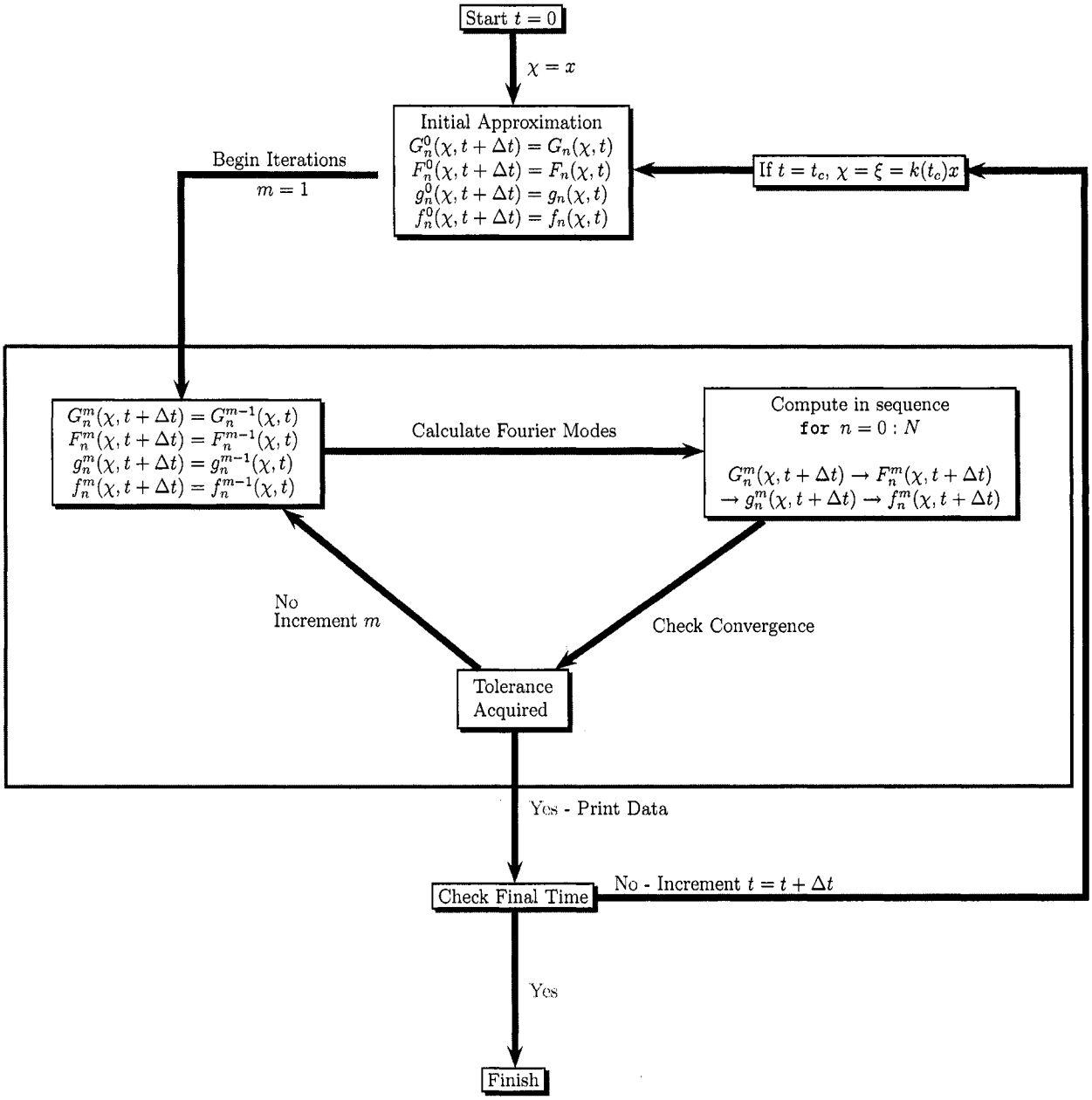

Figure 2.3: Computational flowchart. The variable χ is used to distinguish between the solution in the boundary layer x-coordinate and the physical ξ-coordinate.

The Fourier coefficients in the expansion of the vorticity are governed by equations of the form (2.1.18), for $g_n(x,t)$, which may be rewritten as

$$4t\frac{\partial g_n}{\partial t} = q_n(x,t), \quad n = 1,2,3,... \tag{2.3.2}$$

where

$$q_n(x,t) = e^{-2kx}\frac{\partial^2 g_n}{\partial x^2} + 2x\frac{\partial g_n}{\partial x} + (2 - n^2k^2e^{-2kx})g_n + 2te^{-2kx}nF_n\frac{\partial G_0}{\partial x} + 2te^{-2kx}T_n. \tag{2.3.3}$$

At time $t + \Delta t$, we assume that the solution at the previous time step t is known, with the initial solutions given by (2.1.25)-(2.1.27). The Crank-Nicholson procedure is used to advance the solution by a single time-step via integration of the governing equation from $t = t_j$ to $t_{j+1} = t + \Delta t$ to obtain

$$(4(t+\Delta t) - \frac{\Delta t}{2})(g_n^{j+1} - g_n^j) = \frac{1}{2}\Delta t(q_n^j + q_n^{j+1}) \tag{2.3.4}$$

where the superscripts j and $j+1$ indicate evaluation of the functions at the previous and current time step respectively. Using (2.3.3) defined at $t + \Delta t$, after collecting like terms, (2.3.4) becomes

$$a(x,t+\Delta t)\frac{d^2g_n^{j+1}}{dx^2} + b(x,t+\Delta t)\frac{dg_n^{j+1}}{dx} + c(x,t+\Delta t)g_n^{j+1} = d(x,t+\Delta t) + e(x,t) \tag{2.3.5}$$

where

$$a(x,t+\Delta t) = [e^{-2kx}]^{j+1}, \tag{2.3.6}$$

$$b(x,t+\Delta t) = 2x, \tag{2.3.7}$$

$$c(x,t+\Delta t) = 2 - [n^2k^2e^{-2kx}]^{j+1} - \frac{8}{\Delta t}(t + \frac{1}{2}\Delta t), \tag{2.3.8}$$

$$d(x,t+\Delta t) = -2(t+\Delta t)[e^{-2kx}(nF_n\frac{dG_0}{dx} + T_n)]^{j+1}, \tag{2.3.9}$$

$$e(x,t) = -q_n^j + \frac{8}{\Delta t}(t + \frac{1}{2}\Delta t)g_n^j. \tag{2.3.10}$$

Then, approximating the derivative terms using the standard central finite difference formulae the final discretized equation becomes

$$A^i g_n^{i-1,j+1} + B^i g_n^{i,j+1} + C^i g_n^{i+1,j+1} = D^i + E^i \tag{2.3.11}$$

where the coefficients are

$$A^i = (2a(x_i, t+\Delta t) - b(x_i, t+\Delta t)h_x), \tag{2.3.12}$$

$$B^i = 2h_x^2 c(x_i, t+\Delta t) - 4a(x_i, t+\Delta t)), \tag{2.3.13}$$

$$C^i = (2a(x_i, t+\Delta t) + b(x_i, t+\Delta t)h), \tag{2.3.14}$$

$$D^i = 2h_x^2 d(x_i, t+\Delta t) \tag{2.3.15}$$

$$E^i = 2h^2 e(x_i, t) \tag{2.3.16}$$

for $i = 1, 2, ..., M$. The corresponding form for the Fourier coefficient of $\cos(n\theta)$, namely G_n, is similar and may be derived by mirroring the foregoing analysis. Thus, to determine the solution at time $t + \Delta t$, we must solve $2N + 1$ tri-diagonal non-homogeneous systems of equations in order to completely determine the vorticity during a single iteration. For this we use a tri-diagonal matrix algorithm (TDMA) given in Appendix B. Essentially, this algorithm uses Given's Rotations to eliminate the lower diagonal and then solves the upper bi-diagonal system using back substitution. It is noted that this matrix is non-singular for all the parameter values which have been used in this thesis, a result that we cannot comment on for the general case. Non-singularity, in this case, can is confirmed by verifying diagonally dominance of the tri-diagonal matrix. Therefore, for all simulations conducted by the author the non-singularity of the matrix indicates that the TDMA will not encounter a zero pivot along the diagonal. Hence, the solution of these $2N + 1$ matrix equations is stable.

To calculate F_0 at time $t + \Delta t$ we use the direct scheme in Appendix C to integrate equation (2.1.15) using (2.1.19)-(2.1.20) at the cylinder surface. The other Fourier modes in the expansion of the stream function, f_n and F_n, at time $t + \Delta t$ are solved using the fact that the solutions for G_n and g_n at the current time step have just been calculated. The method of solution follows the procedure of Dennis and Chang (1969) in which the governing equation for $f_n(x, t + \Delta t)$ may be rewritten as

$$\frac{d^2 f_n}{dx^2} - \beta^2 f_n = r_n \tag{2.3.17}$$

where partial derivative is replaced by an ordinary derivative since the time is fixed, $\beta = nk$, and $r_n = e^{2kx} g_n(x, t + \Delta t)$. Introducing

$$p_n(x) = \frac{df_n}{dx} + \beta f_n, \tag{2.3.18}$$

$$q_n(x) = \frac{df_n}{dx} - \beta f_n \tag{2.3.19}$$

we may then decompose equation (2.3.17) into the system

$$\frac{dp_n}{dx} - \beta p_n = r_n, \tag{2.3.20}$$

$$\frac{dq_n}{dx} + \beta q_n = r_n \tag{2.3.21}$$

which must be solved subject to the conditions on the surface of the cylinder given by

$$p_n(0) = 0, \qquad q_n(0) = 0. \tag{2.3.22}$$

The solution of (2.3.21) is obtained via a stable method of integration in the direction of increasing x using the one-step integration formula

$$\begin{aligned} q_n^1 = {} & \gamma q_n^0 + \frac{1}{\beta}(r_n^1 - \gamma r_n^0) - \frac{1}{2h_x\beta^2}[r_n^2 - r_n^0 - \gamma(4r_n^1 \\ & - 3r_n^0 - r_n^2)] + \frac{1}{h_x^2\beta^3}[(r_n^0 - 2r_n^1 + r_n^2)(1 - \gamma)]. \end{aligned} \tag{2.3.23}$$

for $i = 1$ and the two-step formula

$$\begin{aligned} q_n^i = {} & \gamma^2 q_n^{i-2} + \frac{1}{\beta}(r_n^i - \gamma^2 r_n^{i-2}) - \frac{1}{2h_x\beta^2}\left[(3r_n^i \right. \\ & \left. -4r_n^{i-1} + r_n^{i-2}) - \gamma^2(4r_n^{i-1} - 3r_n^{i-2} - r_n^i)\right] \\ & + \frac{1}{h_x^2\beta^3}\left[(r_n^{i+1} - 2r_n^i + r_n^{i-1})(1 - \gamma^2)\right]. \end{aligned} \tag{2.3.24}$$

for $i = 2, 3, ..., M$ where $\gamma = e^{-\beta h_x}$. The same method of forward integration applied to (2.3.20) is unstable due to the appearance of the growing exponential in the homogeneous solution. However, integration backwards from $x = x_{M+1}$ was shown to be stable by Collins (1973). We make a change of variables in equation (2.3.20) from x to z where the relationship between the two is given by

$$x = x_{M+1} - z, \tag{2.3.25}$$

with x_{M+1} a large fixed value. Equation (2.3.20) is then

$$\frac{dp_n}{dz} + \beta p_n = -r_n(x_{M+1} - z) \tag{2.3.26}$$

which must be accompanied by an initial condition at $z = 0$, or $x = x_{M+1}$. However, $p_n(x_{M+1})$ is not known and thus the major difficulty here is to specify the value at the boundary correctly. To do this we integrate the product of $e^{-\beta x}$ and equation (2.3.20) from x_{M+1} to ∞ so that

$$\begin{aligned} &-e^{-\beta x_{M+1}} p_n(x_{M+1}) + \lim_{\xi \to \infty} \left[e^{-n\xi} (D_\xi f_n(\xi) + n f_n(\xi)) \right] \\ &= \int_{x_{M+1}}^{\infty} e^{(2-n)\xi} g_n(\xi) d\xi. \end{aligned} \tag{2.3.27}$$

Now, assuming that x_{M+1} is large enough so that (2.1.21)) is satisfied, and using the far field conditions, we obtain

$$p_n(x_{M+1}) = 2(1 + \dot{V}(t)\cos(\eta)) e^{\beta x_{M+1}} \delta_{n,1}. \tag{2.3.28}$$

The step-by-step integration formula in (2.3.23)-(2.3.24) may then be applied to (2.3.26) to integrate p_n backwards, starting from (2.3.28). As a result, $f_n(x, t + \Delta t)$ may be calculated from

$$f_n(x, t + \Delta t) = \frac{p_n(x) - q_n(x)}{2\beta} \tag{2.3.29}$$

which completes the solution procedure for the corresponding stream function component. Thus, after calculating each of the $2N+1$ vorticity terms we then apply these integration techniques to determine each of the associated stream function terms.

For the full numerical solution, a C++ code which makes use of the freeware GNU Scientific Library (GSL) was written to implement the numerical schemes discussed. The bulk of the numerical simulations were carried out in serial on a 64-processor Beowulf cluster located in the Department of Mathematics and Statistics and on a Silicon Graphics Onyx computer consisting of 28 MIPS R12000 processors located in the Computational Visualization Centre, both at Memorial University.

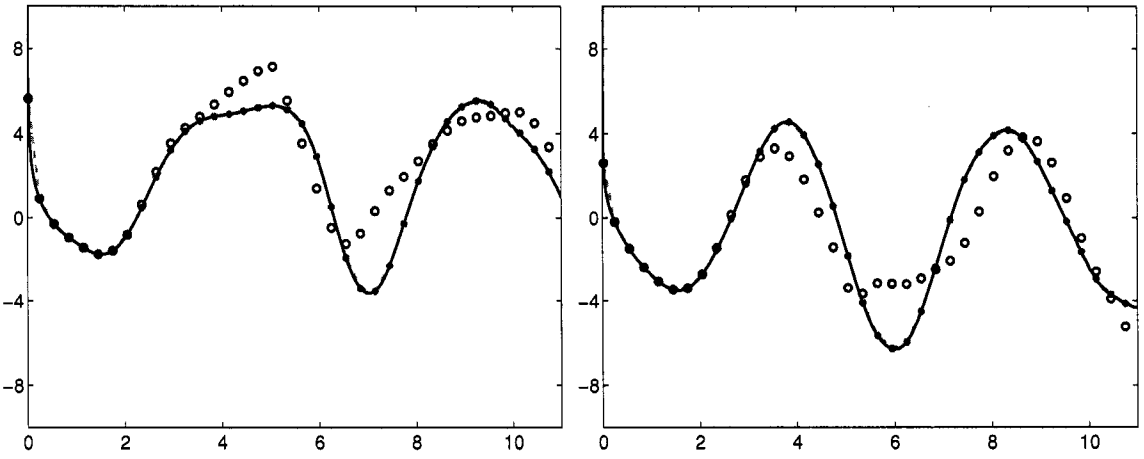

Figure 2.4: The effect of varying x_{M+1} on the drag (left) and lift (right) coefficients for $R = 500$, $A = 0.3$, $\eta = 45°$, $S_f = 2.0S_0$, $S_0 = 0.2$: $x_{M+1} = 4.0$ (○); 6.0 (- - -); 8.0 (—); 10.0 (∗).

2.4 Validation of computational mesh

Before beginning our numerical simulations, there are several coding parameters which must be specified such as the grid size h_x, the time step Δt, the order truncation of the Fourier series N, and the maximum x-coordinate at which we assume that the amount of vorticity in the flow field is negligible. The correct specification of each of these parameters is important to numerical accuracy of the solution procedure and hence, before each simulation, we must conduct a series of experiments to determine the "optimal value" of these parameters. We define this optimal value for each parameter as the value which has the property that the accuracy of the calculation would not change if we refined the value further. In this manner, the computational time and effort required to calculate the solution is also minimized. The procedure for determining these optimal values will be discussed for a sample simulation, but in general we must conduct similar experiments for each choice of the flow parameters.

First, to choose x_{M+1} we vary it from about 4 to 10, as seen in Figure 2.4. We observe that there is minimal effect on the accuracy of these curves when we change

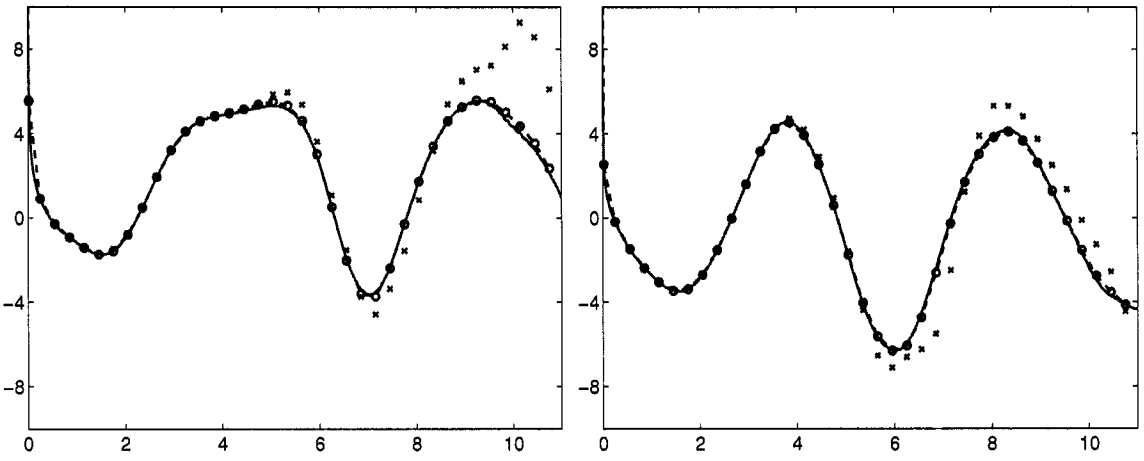

Figure 2.5: The effect of varying h_x on the drag (left) and lift (right) coefficients for $R = 500$, $A = 0.3$, $\eta = 45°$, $S_f = 2.0S_0$, $S_0 = 0.2$: $h_x = 0.025$ (-o-); 0.05 ( ); 0.1 (x).

x_{M+1} from 8 to 10 whereas there was a large effect for all previous transitions. Thus, in this case, we would choose $x_{M+1} = 8.0$ as our optimal value.

Further, we perform numerical experiments to choose the grid size. As seen in Figure 2.5, there is minimal change in accuracy when varying h_x from 0.05 to 0.025 which suggests that it is sufficient to choose h_x as 0.05 for our trials. However, in most of the simulations that we performed, we chose h_x as 0.025 to ensure a high accuracy is maintained in the solution.

Similar trials are conducted to determine Δt and N in this manner. For the majority of our calculations we found that 10 initial time steps of 10^{-4}, followed by 29 time steps of 10^{-3} was able to accurately calculate the flow at small times. Then, for the remainder of the simulation, the time step was fixed at $\Delta t = 10^{-2}$. In addition, a maximum value of $N = 60$ was observed to be more than adequate for the order of truncation of the Fourier series.

2.5 Verification of initial flow simulation

To verify the accuracy of the present algorithm, numerical results are obtained at small times and compared to the results from an alternative numerical method which is essentially a generalization of that used by Collins and Dennis (1973). In this method, each of the scaled Fourier modes in (2.1.14) are expanded in terms of both k and t

$$G_n(x,t) = \sum_{i=0}^{\infty}\sum_{j=0}^{\infty} G_n^{(i,j)}\, t^j\, k^i, \qquad g_n(x,t) = \sum_{i=0}^{\infty}\sum_{j=0}^{\infty} g_n^{(i,j)}\, t^j\, k^i \tag{2.5.1}$$

$$F_n(x,t) = \sum_{i=0}^{\infty}\sum_{j=0}^{\infty} F_n^{(i,j)}\, t^j\, k^i, \qquad f_n(x,t) = \sum_{i=0}^{\infty}\sum_{j=0}^{\infty} f_n^{(i,j)}\, t^j\, k^i. \tag{2.5.2}$$

The process of derivation of the differential equations for these coefficients and the boundary conditions satisfied by these coefficients follows very closely the procedures described Collins and Dennis (1973). It is not necessary to give the analysis in detail and we shall only give the resulting differential equations and boundary conditions of for the order $O(k^i t^j)$ terms:

$$\frac{d^2 f_n^{(i,j)}}{dx^2} = g_n^{(i,j)} + \sum_{p=0}^{i-1} \frac{(2x)^{i-p}}{(i-p)!}\, g_n^{(p,j)}, \tag{2.5.3}$$

$$\frac{d^2 F_n^{(i,j)}}{dx^2} = G_n^{(i,j)} + \sum_{p=0}^{i-1} \frac{(2x)^{i-p}}{(i-p)!}\, G_n^{(p,j)}, \tag{2.5.4}$$

$$\frac{d^2 g_n^{(i,j)}}{dx^2} + 2x\frac{dg_n^{(i,j)}}{dx} - 2[2j+i-1]g_n^{(i,j)} = n^2 g_n^{(i-2,j)} + X_n^{(i,j)}, \tag{2.5.5}$$

$$\frac{d^2 G_n^{(i,j)}}{dx^2} + 2x\frac{dG_n^{(i,j)}}{dx} - 2[2j+i-1]G_n^{(i,j)} = n^2 G_n^{(i-2,j)} + Y_n^{(i,j)}, \tag{2.5.6}$$

$$F_n^{(i,j)}(0) = f_n^{(i,j)}(0) = 0, \tag{2.5.7}$$

$$\frac{\partial F_n^{(i,j)}(0)}{\partial x} = \frac{\partial f_n^{(i,j)}(0)}{\partial x} = 0, \tag{2.5.8}$$

$$\int_0^{\infty} \sum_{p=0}^{i} \frac{[(2-n)x]^{i-p}}{(i-p)!}\, G_n^{(p,j)}(x)\, dx = -2\,\mathrm{coeff}[V(t)\sin(\eta), t^j]\, \delta_{n,1}\, \delta_{i,0}; \tag{2.5.9}$$

$$\int_0^\infty \sum_{p=0}^{i} \frac{[(2-n)x]^{i-p}}{(i-p)!}\, g_n^{(p,j)}(x)\, dx = 2\ \text{coeff}[1 + V(t)\cos(\eta), t^j]\ \delta_{n,1}\delta_{i,0}. \qquad (2.5.10)$$

where $X_n^{(i,j)}$ and $Y_n^{(i,j)}$ resulting from the substitution of the given expansion into the latter terms of (2.1.17)-(2.1.18) are given in Appendix D and coeff$[F(t), t^j]$ is the coefficient of the t^j term in the Taylor series expansion of the function $F(t)$, assuming that such an expansion exists. This method of solution was also used by Collins and Dennis (1974) to solve for flow past an accelerated cylinder where the governing equations, which only consisted of equation (2.5.5) with a slightly smaller summation term $X_n^{(i,j)}$, described the symmetric development of the flow.

Using the solutions obtained from these equations we will form a double power series to approximate each of the Fourier modes which may then be summed to determine the scaled vorticity and stream function. We follow the solution procedure of Collins and Dennis (1973) where when solving for an instance of i and j in equations (2.5.5)-(2.5.6) we solve an equation of the form

$$y'' + 2xy' - 2(2j + i - 1)y = Q. \qquad (2.5.11)$$

The solution of (2.5.11) can be found more accurately if we introduce the transformation $y(x) = e^{-\frac{1}{2}x^2}\phi(x)$ which yields

$$\phi'' - \gamma(x)\phi' = \beta(x) \qquad (2.5.12)$$

where

$$\gamma(x) = x^2 - 1 + 2i + 4j \qquad \text{and} \qquad \beta(x) = e^{\frac{1}{2}x^2}Q(x). \qquad (2.5.13)$$

Ascher, Mattheij, and Russell (1995) discussed the numerical solution of this equation in great detail and showed that the error in the standard finite difference approximation can be drastically reduced from $O(h_x^2)$ to $O(h_x^6)$. This is accomplished by multiplying the central finite difference discretization of (2.5.12) with an appropriate difference operator. For this form of differential equation using a grid size of h_x, the

approximation of equation (2.5.12) is given by

$$\left(1-\frac{1}{12}h^2\gamma_{l-1}\right)\phi_{l-1}+\left(1-\frac{1}{12}h^2\gamma_{l-1}\right)\phi_{l+1}-\left(2+\frac{5}{6}h^2\gamma_l\right)\phi_l=$$

$$\frac{1}{12}h^2\left(\beta_{l-1}+10\beta_l+\beta_{l+1}\right). \qquad (2.5.14)$$

When the $O(k^i t^j)$ vorticity component of each Fourier mode has been calculated, the corresponding $O(k^i t^j)$ stream function component is determined using equations (2.5.3)-(2.5.4) and a direct integration procedure of order h_x^7 given in Appendix C. Using this procedure we numerically compute as many terms in the k and t expansion as we desire. For the purpose of this thesis, we will calculate the first 12 terms in the expansions. The final series solution, which is valid for small values of the time t and small values of the parameter k, will be used to verify the accuracy of the full numerical scheme in the initial stages of motion.

We compare the results of several flow properties calculated from the full numerical integration scheme with the small-time results of the time series expansion calculated numerically. The time development of the surface vorticity for $R = 200$, $A = 0.6$, $\eta = 45°$ and $S_f/S_0 = 1.0$ is given in Figure 2.6. For $t \leq 0.5$ the agreement between the two sets of results is excellent with small discrepancies observed as we increase the time.

The time-development of the drag and lift coefficients in Figure 2.7 shows the effect of increasing the Reynolds number when $A = 0.6$, $\eta = 45°$, and $S_f/S_0 = 1.0$. For all Reynolds number, in the initial stages of motion, it is evident that the large numerical and small-time solutions agree quite well. As R becomes smaller, however, the small-time solution is less accurate as $t \to 1$. A plot of the infinity norm between the series of curves is given at the bottom of each column where we observe increasing accuracy for increasing Reynolds number. Hence, the results obtained by the full numerical integration procedure are in good agreement with the approximate solution which is obtained based on small time series expansions and is valid for large R.

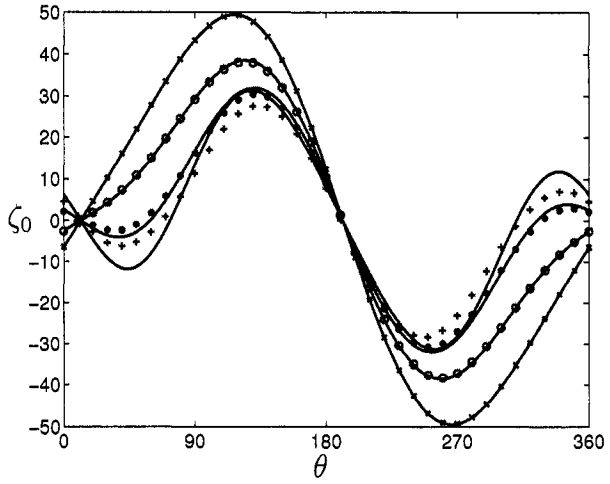

Figure 2.6: Full numerical (—) time development of surface vorticity for $R = 200$, $A = 0.6$, $S_f = 1.0S_0$, $S_0 = 0.1954$ compared with the series expansion solution at time $t = 0.1$ (x); $t = 0.2$ ($\circ$); $t = 0.5$ ($*$); $t = 0.8$ ($+$).

2.6 Validation of uniform flow simulations

The numerical findings of Qian and Vezza (2001) are first used for comparison in this case. Qian and Vezza (2001) implement a finite volume technique to solve the problem of impulsively started flow past a circular cylinder for a Reynolds number of $R = 1000$. In doing so, they display both long and short term development of the flow, the latter of which we will focus on.

The development of the vorticity at small values of the time is compared with the results of Qian and Vezza (2001) in Figure 2.8. At five instances, we show the equi-vorticity contours and conclude that our numerical solution accurately calculates the size, location, and shape of the developing vortices. In addition, corresponding to an impulsive start, we observe the initial formation of vortices at the rear of the cylinder which is followed by, as we increase the time, the creation of a second vortex (at $t = 2.0$) which interacts with the original vortex. This interaction is further depicted in the streamlines at $t = 5.0$ in Figure 2.9. We display the resulting drag coefficient calculation in Figure 2.10. The result which is compared with that obtained by Qian

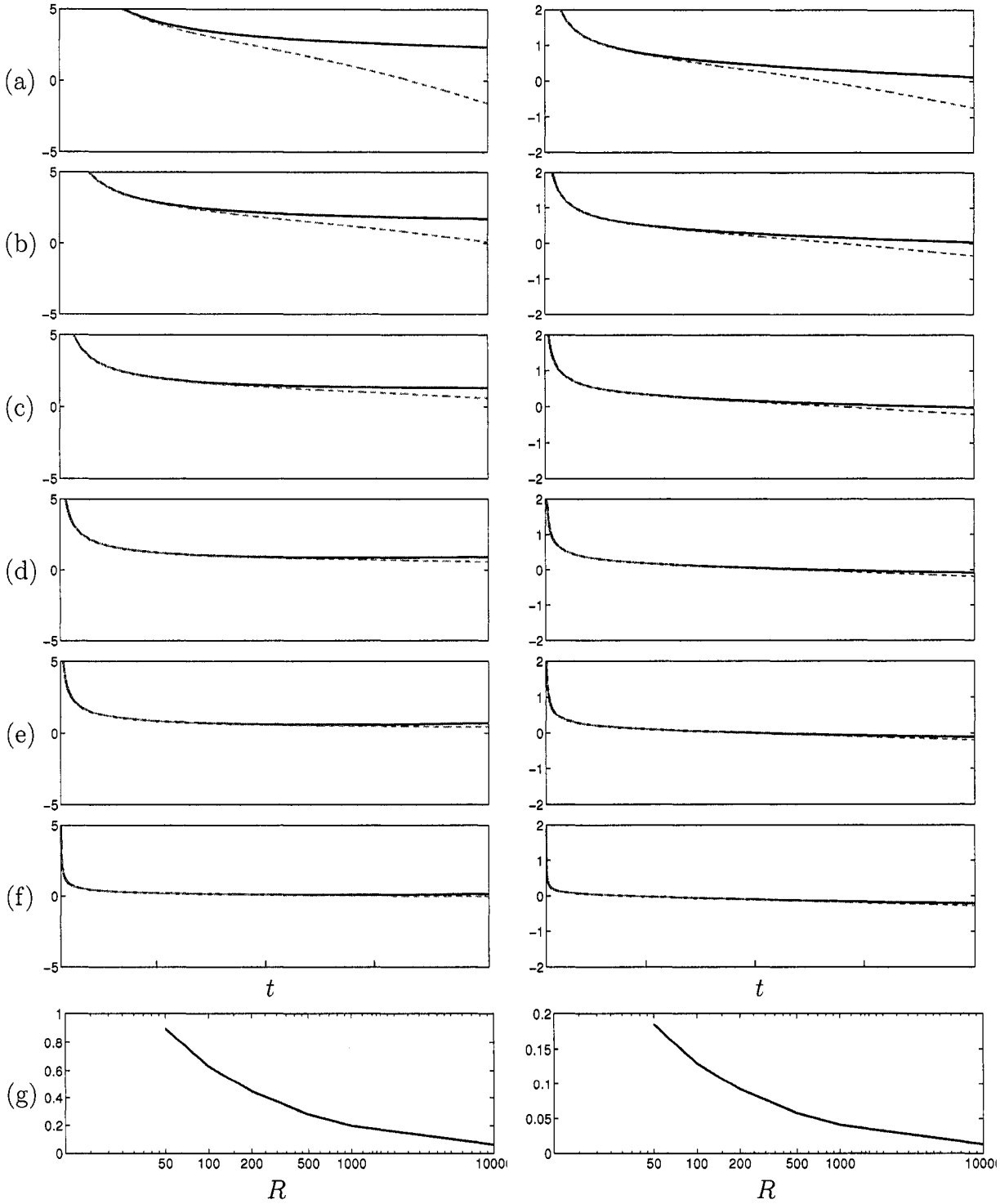

Figure 2.7: Drag (left) and lift (right) comparisons of small-time series solution (- - -) with full numerical integration solution (—) for $t \leq 1$, $A = 0.6$, $S_f = 0.1954$, $\eta = 45°$: (a) $R = 50$; (b) $R = 100$; (c) $R = 200$; (d) $R = 500$; (e) $R = 10^3$; (f) $R = 10^4$; (g) Error (infinity norm) between solutions for each Reynolds number.

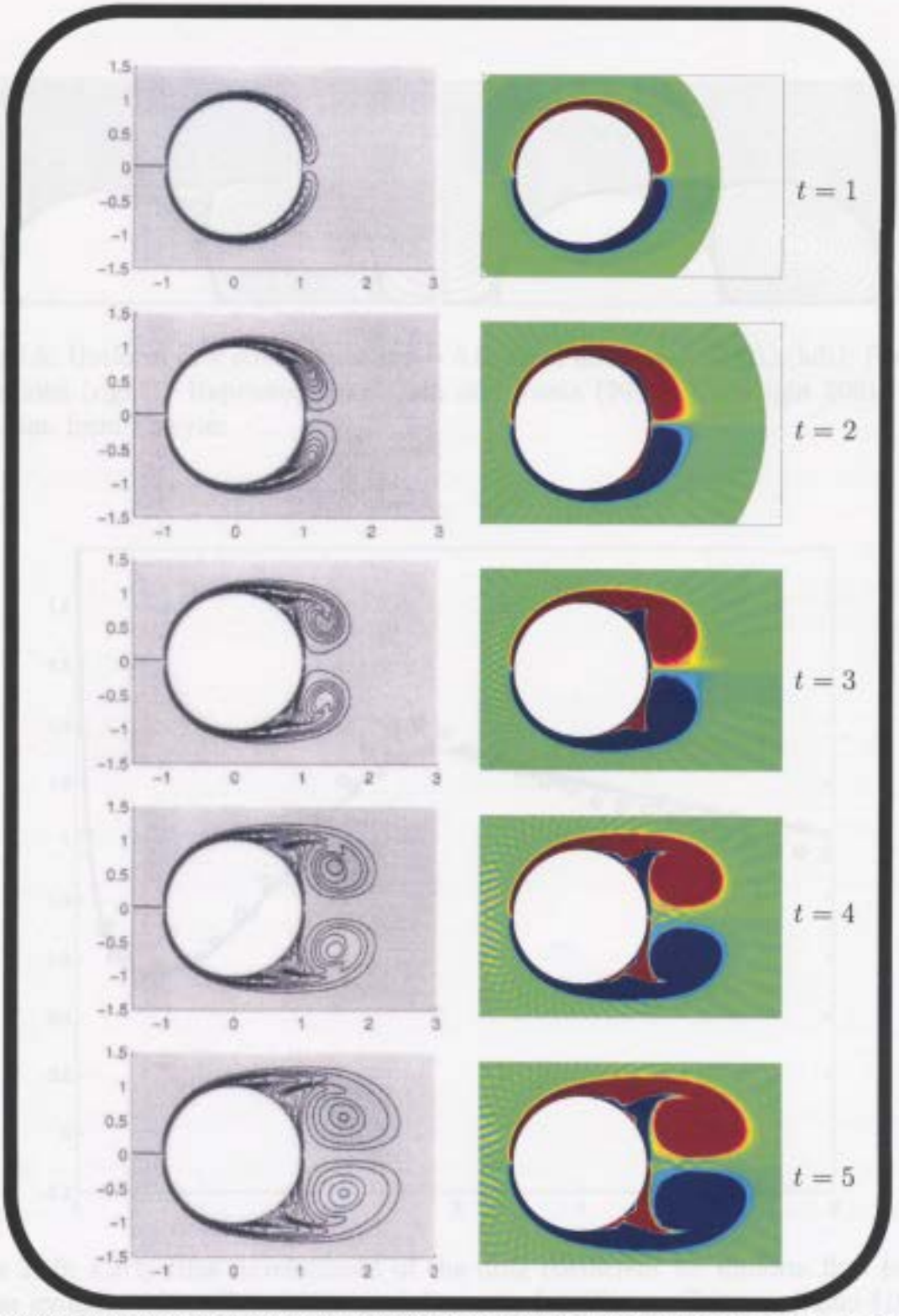

Figure 2.8: Present calculation of vorticity contours (right) compared with the results of Qian and Vezza (2001) (left) for the uniform flow case with $R = 1000$. Reprinted from Qian and Vezza (2001), Copyright 2001, with permission from Elsevier.

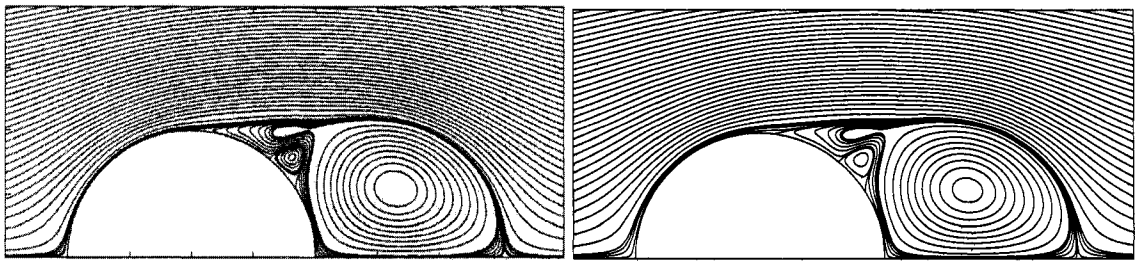

Figure 2.9: Uniform flow streamlines at $t = 5.0$: Qian and Vezza (2001) (left); Present calculations (right). Reprinted from Qian and Vezza (2001), Copyright 2001, with permission from Elsevier.

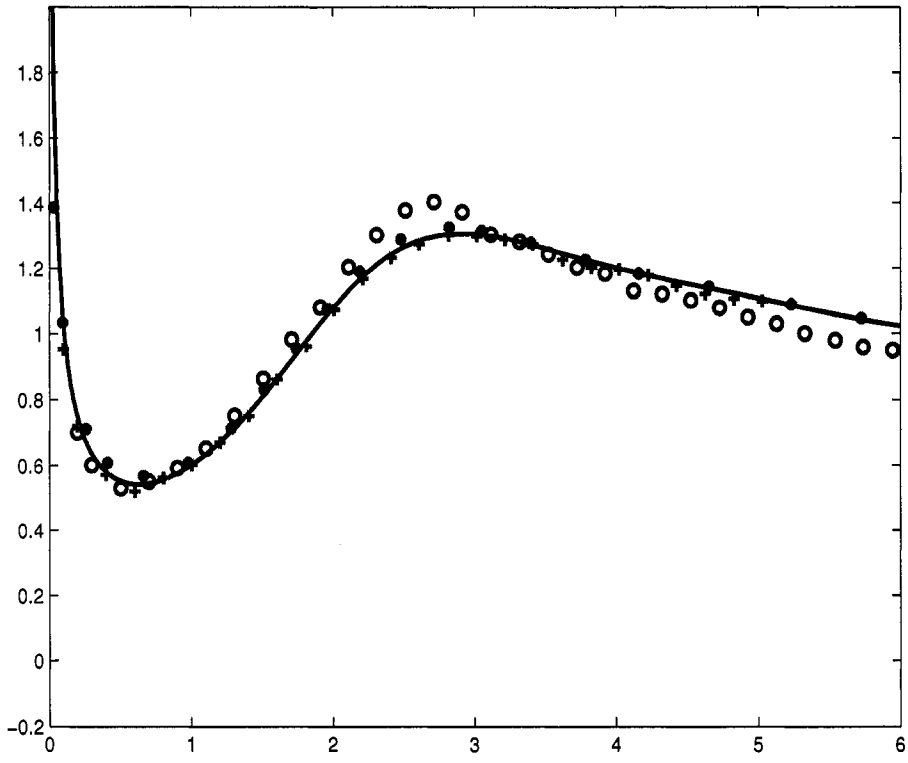

Figure 2.10: Early time development of the drag coefficient for uniform flow past a circular cylinder when $R = 1000$: (—) Present; (○) Cheng, Chew and Luo (1997); (+) Koumoutsakos and Leonard (1995); (•) Qian and Vezza (2001). Reprinted from Qian and Vezza (2001), Copyright 2001, with permission from Elsevier.

and Vezza (2001), Koumoutsakos and Leonard (1995) and Cheng, Chew and Luo (1997) who all use hybrid vortex methods, shows good agreement.

Next, we use the Computational Fluid Dynamics (CFD) commercial package FLUENT to solve for uniform flow past a circular cylinder when $R = 500$ and compare it to the numerical result we obtain. This package is loosely based on a finite element technique for solving flows over complex geometries and implements a wide range of numerical strategies to optimize convergence and accuracy. Figure 2.11 shows a comparison of the results obtained by FLUENT with the vorticity contours produced from our numerical solution. The results are in good agreement with one another.

2.7 Validation of forced cross-flow oscillation simulations

The next verification which we will perform is for the case of transverse ($\eta = 90°$) oscillations. We make comparisons with the recent results which have been presented by Guilmineau and Queutey (2002) in which $R = 185$, $A = 0.4$, and $0.8 \leq S_f/S_0 \leq 1.2$. Figure 2.12 shows a comparison of the vorticity contours as we increase the forcing frequency ratio through the fundamental lock-on regime. In the figure, we see that for $S_f/S_0 \leq 1.1$, the area of major concentration of vorticity is the upper half of the cylinder. However, as we increase the forcing frequency ratio above this value we see a switching of the concentration of vorticity from the top to the bottom half of the cylinder. The phase shift and amplitude jump in the lift force which occurs in this lock-on regime is attributed to this switching phenomenon as explained by Guilmineau and Queutey (2002); Lu and Dalton (1996); Cetiner and Rockwell (2001).

For large amplitude transverse oscillations, we compare our results to Li, Sherwin and Bearman (2002) who used a fixed mesh spectral element solver. Shown in Figure 2.13 are the equi-vorticity contours at $R = 200$, $S_f/S_0 = 0.8$, $0 \leq A \leq 1.3$.

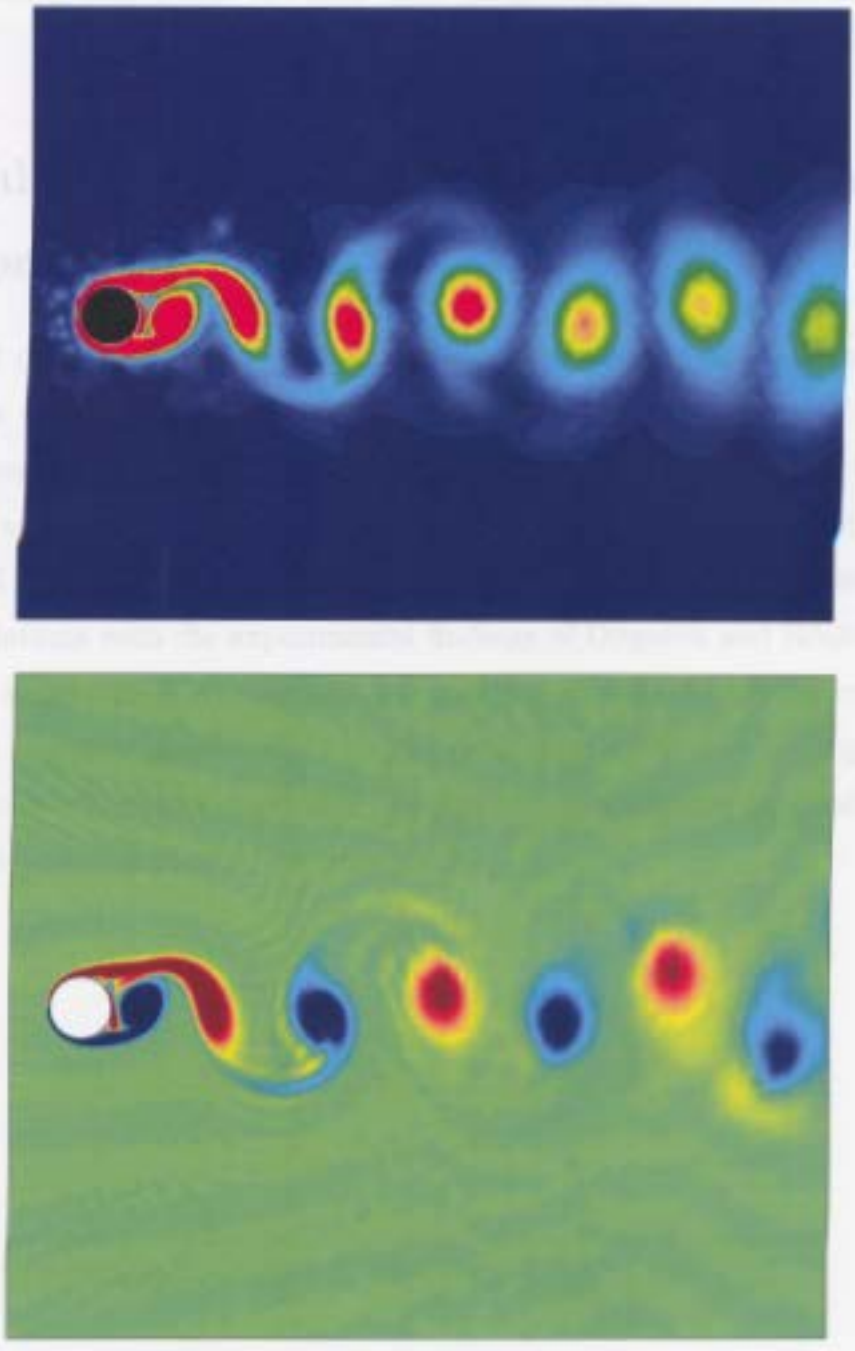

Figure 2.11: Equi-vorticity contours at instant when lift force on cylinder is zero, changing from positive to negative for uniform flow past a circular cylinder when $R = 500$: FLUENT (top); Present calculation (bottom).

Satisfactory qualitative agreement is observed between the two sets of figures where, for an increasing amplitude, the near-wake mode transition from 2S to P+S is captured.

2.8 Validation of forced oblique oscillation simulations

The final set of verifications we will consider are for oblique oscillations of a circular cylinder at $\eta = 45°$ in a uniform flow. Our simulations are compared with the experimental results of Ongoren and Rockwell (1988b) for the case when the Reynolds number is $R = 855$, the amplitude of oscillation is $A = 0.26$, and the forcing frequency ranges from 1.0 to 4.0. A comparison of the vorticity contours calculated in our numerical simulations with the experimental findings of Ongoren and Rockwell (1988b) are given in Figure 2.14. Snapshots are take the instant when the cylinder is at its maximum negative displacement in the oscillation cycle over a range of forcing frequency ratios. The numerical and experimental results are in good qualitative agreement with one another in the near wake.

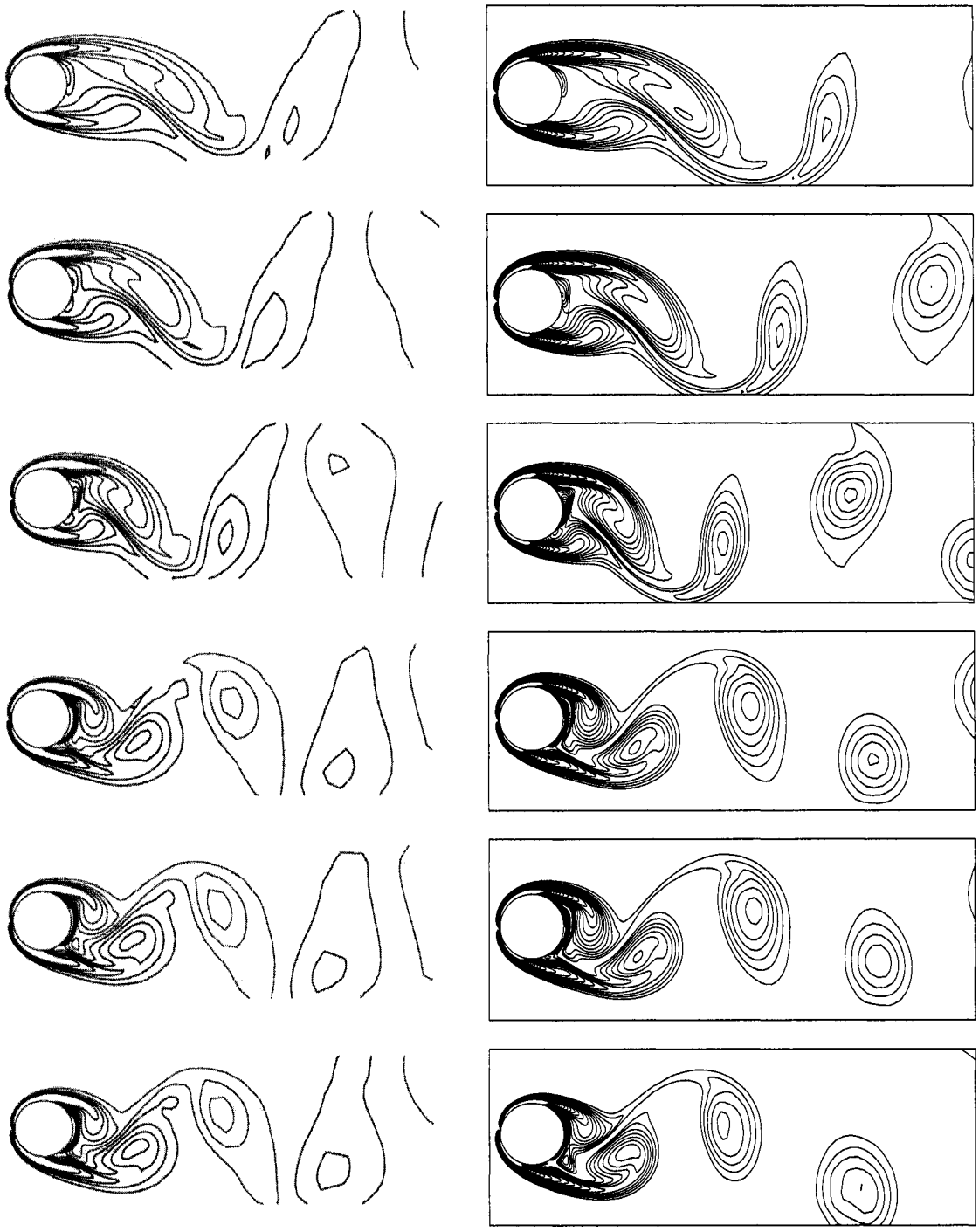

Figure 2.12: Comparison of vorticity contours over a range of forcing frequencies in the fundamental lock-on regime when $R = 185$ and $A = 0.4$.: Guilmineau and Queutey (2002) (left); Present calculations (right). From top to bottom $S_f/S_0 = 0.8$, 0.9, 1.0, 1.1, 1.112, and 1.2. Reprinted from Guilmineau and Queutey (2002), Copyright 2002, with permission from Elsevier.

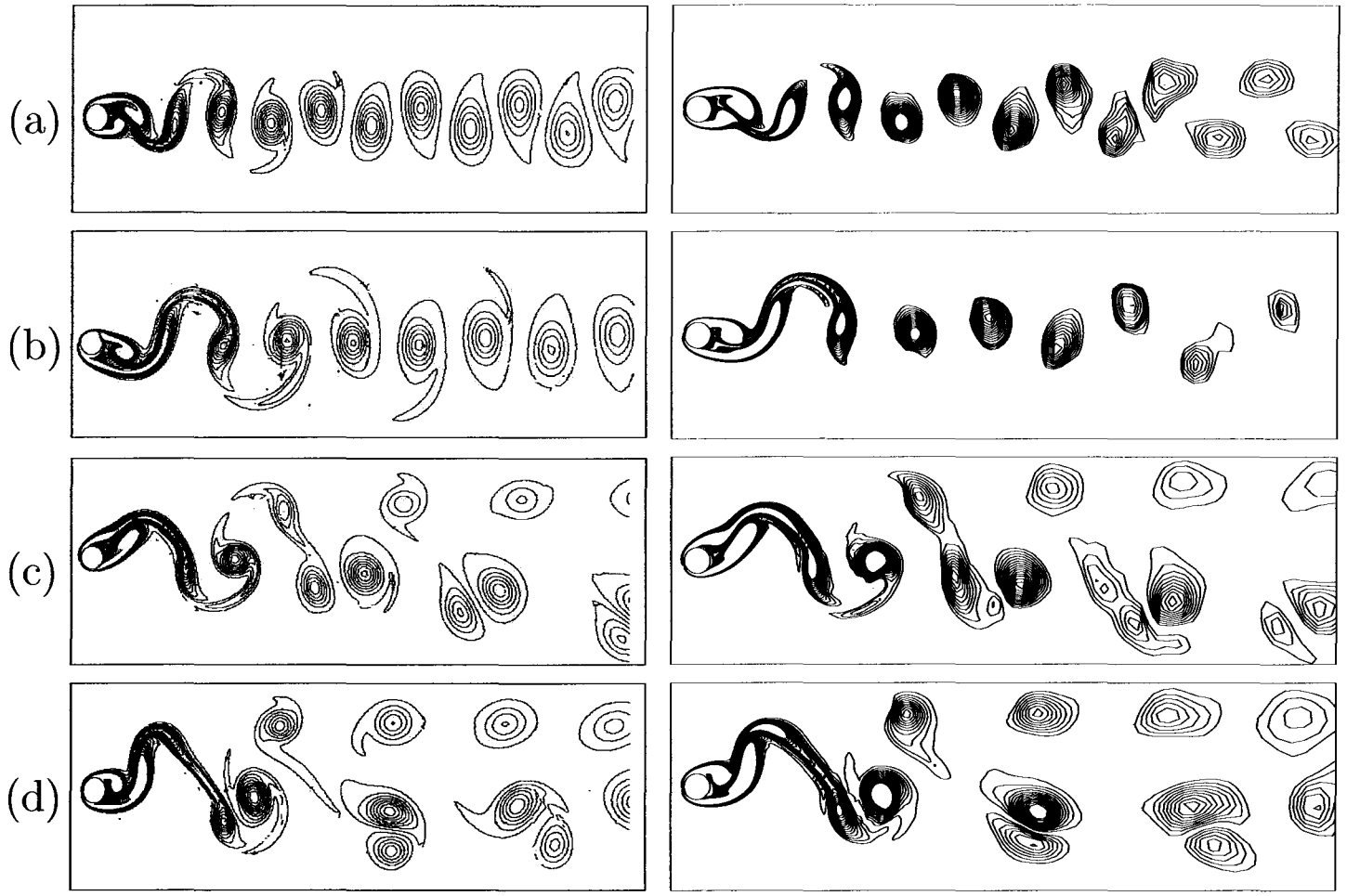

Figure 2.13: Comparison of present (right) numerical findings with those of Li, Sherwin and Bearman (2002) for $R = 200$, $S_f/S_0 = 0.8$, $\eta = 90°$: (a) $A = 0$; (b) 1.0; (c) 1.2; (d) 1.3. Reprinted from Li, Sherwin and Bearman (2002), Copyright 2002, with permission from John Wiley and Sons Limited.

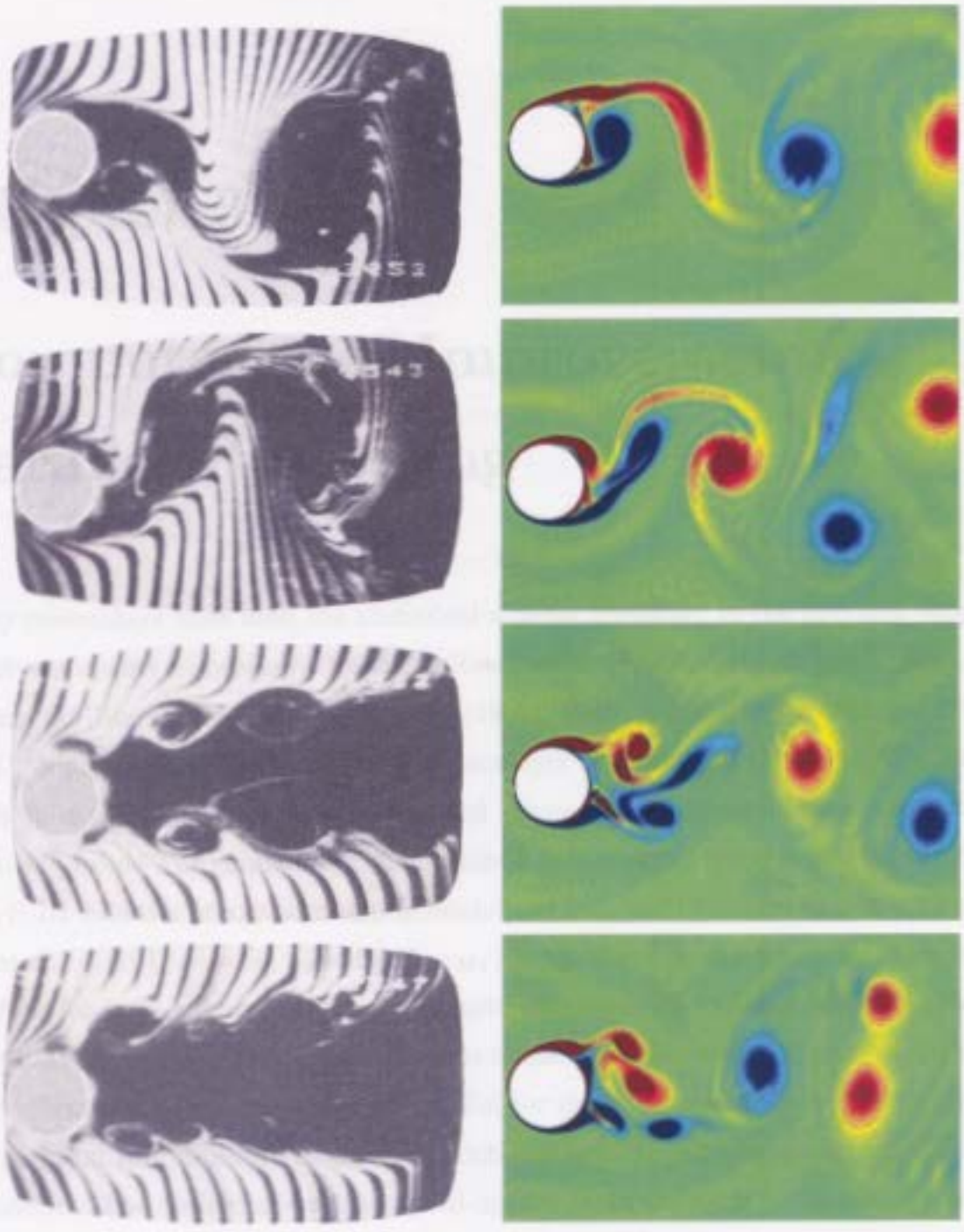

Figure 2.14: Comparison of present (right) numerical findings with those of Ongoren and Rockwell (1988b) for $R = 855$, $A = 0.26$, $\eta = 45°$ and $S_f/S_0 = 1.0$, 2.0, 3.0, 4.0 (from top to bottom). Reprinted from Ongoren and Rockwell (1988b), Copyright 1988, with the permission of Cambridge University Press.

Chapter 3

Computational Improvements - Parallel Processing

Many researchers have used the numerical scheme presented in the previous chapter to solve a variety of problems involving flow past a circular cylinder [see Collins and Dennis (1973b; 1974), Badr and Dennis (1985), Badr, Dennis and Kocabiyik (1995; 1996), Nguyen and Kocabiyik (1997), Kocabiyik and Nguyen (1996; 1999)]. In all of these cases, since a common numerical scheme is used, execution times remain relatively fixed. The simulation time obtained in this thesis when executing the code on a P-III 400MHz processor is approximately 3 hours per 10 dimensionless time units (when $\Delta t = 0.01$, $N = 60$, $h_x = 0.025$, $x_{M+1} = 8$). Thus, to calculate the behavior of the flow for large values of the time up until about $t = 300$ requires about 4 days of computational effort. This thesis attempts to decrease the execution time of the code by performing the computations in parallel for the first time. To do this we divide the program into multiple fragments which can execute simultaneously on different processors. The desired effect is to speed-up the execution time which ideally should be P times as fast if we use P processors.

3.1 Parallel implementation

To execute the numerical simulations in parallel we use the shared memory architecture Silicon Graphics Onyx computer which consists of 28 processors. To do the actual implementation of the parallel code we use standard OpenMP directives for C/C++. However, before implementing the parallelization must first analyze the numerical formulation of the problem.

As mentioned earlier, the governing equations (2.1.15)-(2.1.18) resulting from a Fourier series expansion are all interdependent and thus iterations are used to improve the solution. The Gauss-Seidel iterative scheme which is incorporated into the numerical scheme requires that we use the most recent updated values for G_n, g_n, F_n, and f_n during the calculation of the current iteration. Other researchers add an additional element to this scheme using over and under-relaxation parameters. The benefit of these schemes is that the number of iterations required for the calculation to converge to a solution is decreased, as compared to the Gauss-Jacobi method, in which *only* information from the previous iteration is used in the calculation. In addition to using the improved iterative procedures, it is also possible to decrease the time required by performing parallel computations. However, using the Gauss-Seidel method (with or without the relaxation parameters) seriously limits the possible speedup because it uses the most recent information during each iteration, and thus a worthwhile parallel algorithm is difficult to derive. To allow for a significant speedup during parallel computations, we must use the Gauss-Jacobi scheme, or some other iterative scheme where the calculations at the current iteration depend solely on those from the previous iteration. Hence, the question which remains unanswered is whether or not using improved iterative schemes (Successive Over-Relaxation, Conjugate Gradient, Chebyshev Iteration, Minimum Residual) has a larger impact on the computational time than does parallelization.

Using the Gauss-Jacobi iterative method the most significant computation that we

may perform in parallel is the computation of each of the Fourier coefficients. Firstly, this iterative scheme allows us to compute G_n and g_n in parallel since their values at the current iteration are independent. Second, during the calculation of the Fourier coefficients, the modes corresponding to n are not dependent on the modes corresponding to $n-1$ at the current iteration. Hence, we may divide the work required to calculate G_n, F_n, g_n, and f_n (for $n = 1, ..., N$), during one iteration (as depicted in Figure 3.1), into P processors as seen in Figure 3.2. In this figure we observe

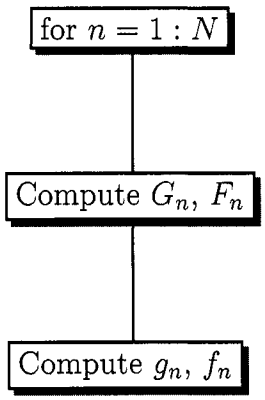

Figure 3.1: Execution of n-loop during iteration in serial.

that $P/2$ of the total P processors are devoted to the calculation of G_n, F_n, and $P/2$ processors are devoted to g_n, f_n. For instance, given 8 processors, we use 4 processors to calculate G_n, F_n and 4 to calculate g_n, f_n. Then, we distribute certain values of n to each processor for calculation so that the time each processor remains idle is minimized. For instance, if $N = 60$, and $P = 8$, then the tasks would be completed as shown in Table 3.1. Notice that the calculation of the Fourier modes is divided equally into the P processors with the exception that processor 0 will compute G_0 and F_0. Also note that we calculate the vorticity component and corresponding stream function component on the same processor since separation of the two components will not minimize the time required. In fact, our experiments have shown that about 90% of the execution time is used in computing the vorticity components G_n, g_n and only about 5% is used to compute the corresponding stream function F_n, f_n.

Figure 3.2: Execution of n-loop during iteration in parallel.

Functions	Processor	n computed
G_n, F_n	0	$0 \rightarrow 15$
	1	$16 \rightarrow 30$
	2	$31 \rightarrow 45$
	3	$46 \rightarrow 60$
g_n, f_n	4	$0 \rightarrow 15$
	5	$16 \rightarrow 30$
	6	$31 \rightarrow 45$
	7	$46 \rightarrow 60$

Table 3.1: Allotment of tasks on 8 processors when $N = 60$.

3.2 Results

To analyze the execution of the code, we use the Speed Shop utility to record important parameters such as the CPU time on each processor. In addition, we concentrate on one particular instance of flow (given by $A = 0.2$, $\eta = 45°$, $S_f/S_0 = 2.0$) and numerical parameters (given by $x_{M+1} = 8.0$, $h_x = 0.025$, $N = 60$). In the analysis, the code must perform 1036 time steps to reach a final dimensionless time of $t = 10$.

The CPU time required and speed-up S_P on P processors, defined as

$$S_P = \frac{\text{CPU time in serial}}{\text{CPU time on } P \text{ processors}}, \tag{3.2.1}$$

as we increase the number of processors is given in Table 3.2 and represented graphically in Figure 3.3. Using two processors we observe a optimal value for the speedup

P	Real Execution Time (minutes)	Ideal Execution Time	Real S_P	Ideal S_P
1	183.5	-	1.00	1.00
2	91.6	91.8	2.00	2.00
4	49.4	45.9	3.71	4.00
8	28.4	22.9	6.47	8.0

Table 3.2: Time and speed-up results.

since our code executes twice as fast. However, as we increase the number of processors, the difference between the theoretical and actual values for the speed-up

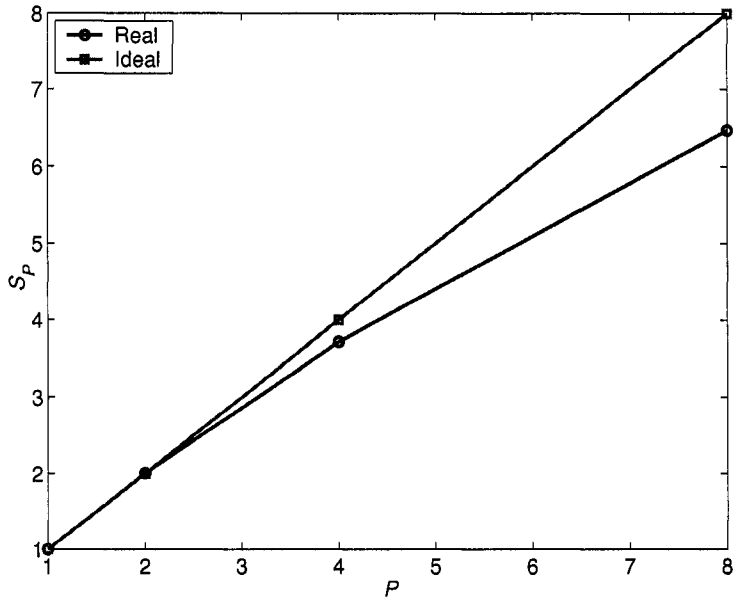

Figure 3.3: Theoretical and computed speed-up.

increases. This is a common observation in parallel processing since as the number of processors increases, the time required for each slave to communicate with the master increases.

The accuracy of the Gauss-Seidel method as compared to the Gauss-Jacobi method when the program executes in serial is depicted in Figure 3.4 where the infinity norm between the drag and lift coefficients is calculated. For these trials a tolerance of 10^{-5} was used in each of the convergence schemes. Therefore, the Gauss-Seidel and Gauss-Jacobi iterative schemes should be accurate to at least 5 decimal places if they converge to a unique solution. As shown in Figure 3.4, the error in the curves is always less than 10^{-5} as expected. The only error observed in this curves is outside of the range of the prescribed tolerance. Theoretically, a tolerance of 10^{-10} could be prescribed to display the decimal place at which both iterative schemes differ, but from a computational point of view obtaining such an accuracy is impossible due to deviations resulting from the use of floating point arithmetic. Hence, there is no difference in the accuracy of the calculations when we switch iterative schemes, as

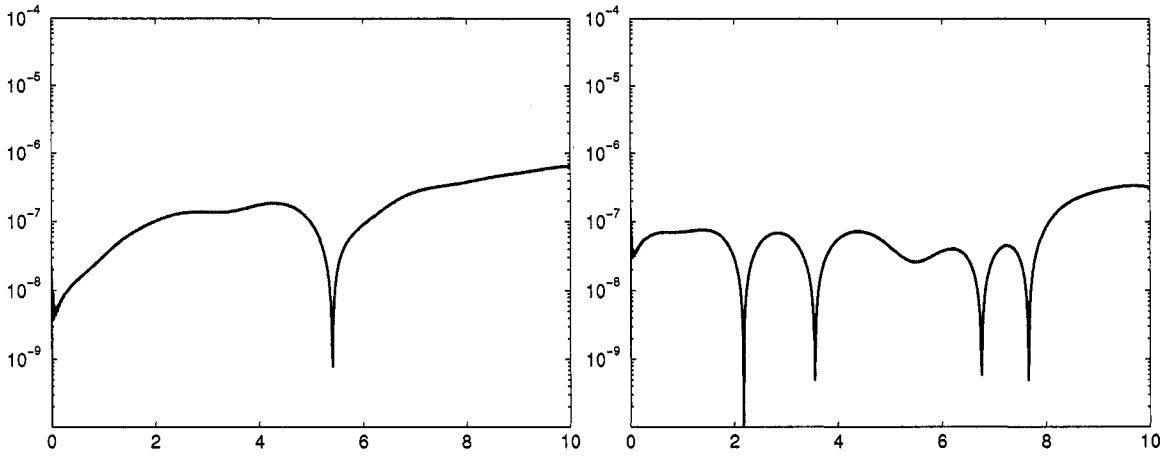

Figure 3.4: Error calculated by means of infinity norm between the lift (left) and drag (right) coefficients when using the Gauss-Seidel and Gauss-Jacobi iterative methods.

expected from theory.

In fact, the purpose of using Gauss-Seidel scheme is to decrease the number of iterations. However, it is noted that the total number of iterations required for convergence to the desired solution does not increase drastically when we use the Gauss-Jacobi. For Gauss-Seidel iterations, a maximum of 4 iterations was observed when working in the parameter range of this thesis, whereas, for the Gauss-Jacobi scheme a maximum of 5 iterations was observed. Hence, for the range of parameters used in this thesis, the improved iterative scheme does drastically reduce the number of iterations. Thus, parallelization is crucial in the speed-up of the execution time.

Chapter 4

Oblique Oscillations of a Circular Cylinder: Lock-on regimes via spectral analysis

In this chapter we will discuss the results for flow past an obliquely oscillating circular cylinder at a Reynolds number of $R = 200$. Frequency variations in the range $0.3 \leq S_f/S_0 \leq 3.2$ for a fixed angle, $\eta = 45°$, and amplitude, $A = 0.5$, are considered so that we may classify the ranges in which lock-on occurs.

The results are analyzed using numerical flow visualization by means of equi-vorticity contours and streamlines. To do this we present snapshots of the flow field at precise instants during the cylinder oscillation. Figure 4.1(a) shows the displacement of the cylinder with distinct points A to Q along its trajectory. The first position A, is taken when the cylinder is at the origin moving downward as seen in Figure 4.1(b) where the actual cylinder position corresponding to nodes A to Q have been plotted. Note that positions I and Q correspond to the completion of one, T, and two, $2T$, periods of oscillation, respectively. All other positions are spaced equally in time using intervals of $T/8$. We will use this lettering to present snapshots of the flow field.

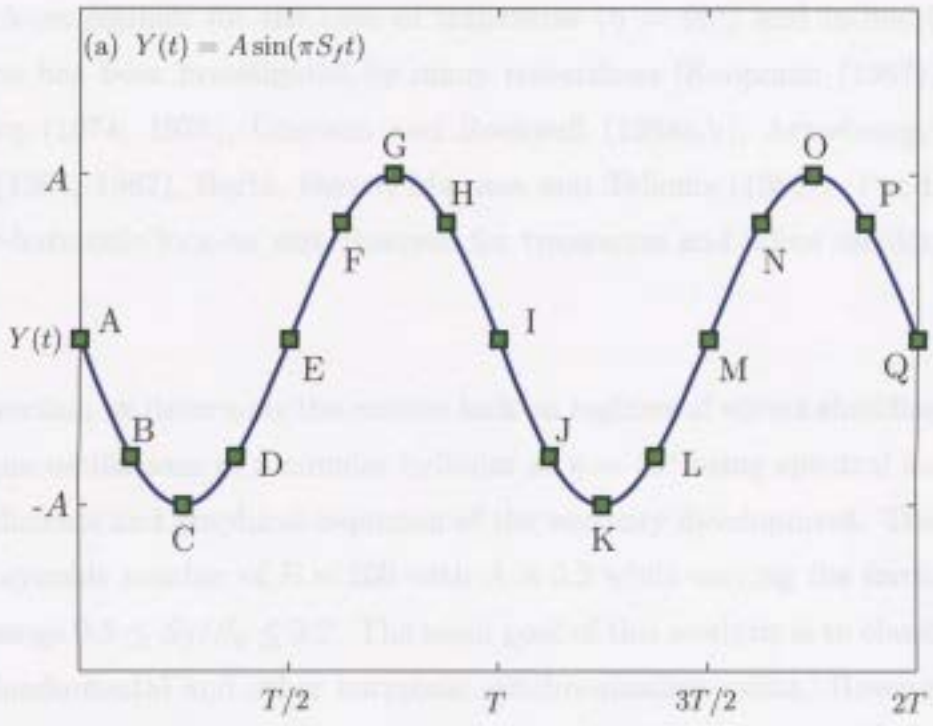

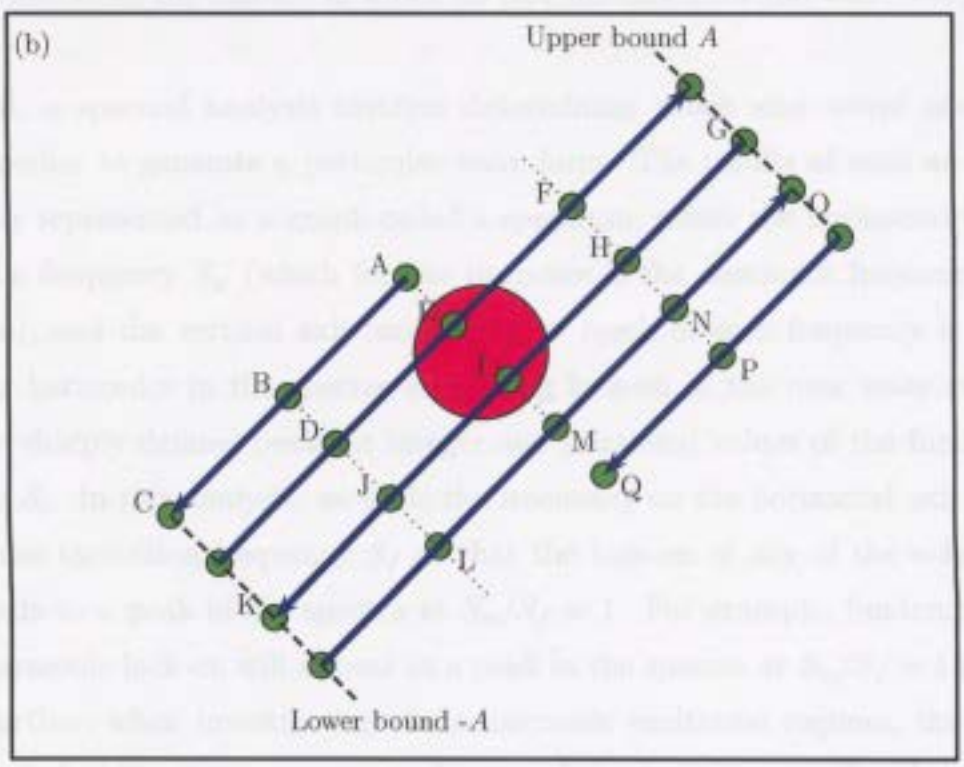

Figure 4.1: (a) Displacement trajectory of the cylinder over two periods, $2T$, of cylinder oscillation with an interval spacing of $T/8$ representing times at which flow field snapshots will be taken and (b) cylinder positions at each snapshot

The lock-on regimes for the case of transverse ($\eta = 90°$) and in-line ($\eta = 0°$) oscillations has been investigated by many researchers [Koopman (1967), Griffin and Ramberg (1974; 1976), Ongoren and Rockwell (1988a,b), Armstrong, Barnes and Grant (1986; 1987), Barbi, Favier, Maresca and Telionis (1986)]. Fundamental and 2-super-harmonic lock-on was observed for transverse and inline oscillations, respectively.

In this section we determine the various lock-on regimes of vortex shedding for the case of oblique oscillations of a circular cylinder at $\eta = 45°$ using spectral analysis of the lift coefficients and graphical depiction of the vorticity development. The simulations use a Reynolds number of $R = 200$ with $A = 0.5$ while varying the forcing frequency in the range $0.3 \leq S_f/S_0 \leq 3.2$. The main goal of this analysis is to classify regions in which fundamental and other harmonic synchronization exists. However, before we begin, we introduce the manner in which we plot the spectrum and what it represents.

In general, a spectral analysis involves determining which sine waves need to be added together to generate a particular wave form. The results of such an analysis are usually represented on a graph called a spectrum, where the horizontal axis represents the frequency S_w (which for our purposes is the dominant frequency in the near wake), and the vertical axis measures how much of each frequency is present. Particular harmonics in the spectra suggesting lock-on in the near wake are represented by sharply defined peaks at integer and fractional values of the fundamental frequency S_0. In this analysis, we scale the frequency on the horizontal axis S_w with the cylinder excitation frequency S_f so that the lock-on of any of the n-harmonics corresponds to a peak in the spectra at $S_w/S_f = 1$. For example, fundamental and 2-superharmonic lock-on will appear as a peak in the spectra at $S_w/S_f = 1.0$ in both cases. Further, when investigating the n-harmonic excitation regimes, the effect of the natural shedding frequency is seen by a peak in the spectra at $S_w/S_f = 1/n$.

Using this scaling, we summarize some of the more commonly occurring waveforms in Figure 4.2. The graphs in the left-hand column represent the particular waveform and the graph on the right is the corresponding spectrum. Note that for these waveforms, the frequency noted below the wave name in Figure 4.2 is the one used in the normalization of the wake frequency. Waves A, B, and C are created using a single sine function with forcing frequencies $S_f/S_0 = 1.0, 2.0$, and 3.0, respectively. For all three frequencies, we see peaks in the associated spectra at $S_w/S_f = 1.0$ since the wake frequency S_w is normalized by the forcing frequency. For each of these waveforms, however, we see that the amplitude of the curve from period to period remains constant which is not always the case for the lift coefficient of an oscillating cylinder. If we add two of these fundamental waves together the effect is to create shapes such as waves $A+B$, $A+C$, $B+C$, and $A+B+C$ where different amplitudes are present, but still the period in each is $T = 2/S_f$. Modifications to the period are introduced via the addition of the $\frac{1}{2}$ and $\frac{1}{3}$-subharmonic frequencies which would appear as peaks at $S_w/S_f = S_0/2S_f$ and $S_0/3S_f$, respectively. This figure suggests how particular waveforms are created. Some of these waveforms will be evident in our lift coefficient, especially near forcing frequencies in the 2-superharmonic excitation regime where two local maxima occur similar to wave A+B.

It is also important to note that the spectrum is a purely mathematical concept. As such, it will give the frequencies which are dominant in the Fourier approximation of the curve, which in this case is the lift coefficient. Thus, to completely determine the state of the vortex shedding we must also take into account the amplitude of lift over each oscillation cycle and the near wake isolines. An approximate repeated amplitude or series of repeated amplitudes indicates a locked-on state of vortex shedding since the size of each vortex shed is linked to the local maxima and minima of the lift coefficient. Once lock-on is established in a particular range of forcing frequencies, S_f, interesting vortex shedding modes are then depicted.

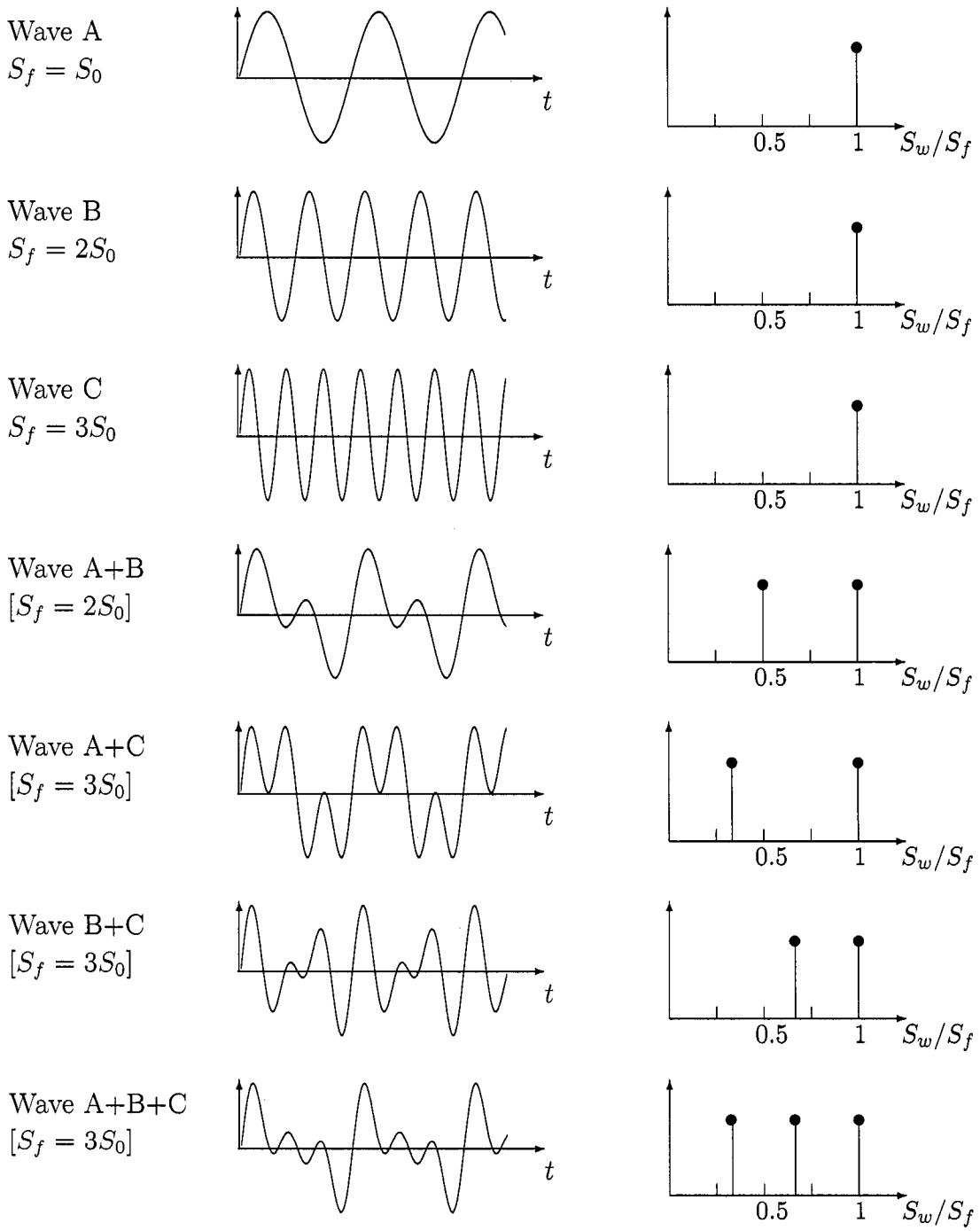

Figure 4.2: Waveforms and spectra created by varying frequencies in trigonometric functions.

4.1 $\frac{1}{2}$-subharmonic excitation for $R = 200$, $A = 0.5$, and $\eta = 45°$: $0.3 \leq S_f/S_0 \leq 0.7$

The lift coefficients with corresponding spectrum for $A = 0.5$, are plotted in Figure 4.3 for values of the forcing frequency near $S_f = 0.5S_0$. In this case the peak in the spectrum shifts according to the inverse of the forcing frequency ratio. For example, at $S_f/S_0 = 0.3$, we see the peak is approximately at $S_w/S_f = 3.33$ and it moves to the left as we increase the forcing frequency. This peak in the spectrum suggests that the natural shedding frequency observed for uniform flow past a circular cylinder is still dominant since

$$\frac{S_w}{S_f} = 3.33 \Rightarrow S_w = 3.33S_f \Rightarrow S_w = 3.33(0.3S_0) \approx S_0.$$

The same observations can be made as the forcing frequency increases to $S_f/S_0 = 0.7$. That is, the peaks in the spectra are resultant from the natural shedding frequency, not the cylinder oscillation frequency. We note that if S_f was not used to normalize the near wake frequency S_w, then for all of these frequencies, $0.3 \leq S_f/S_0 \leq 0.7$, we would obtain a peak at $S_w \approx S_0$ whereas $\frac{1}{2}$-subharmonic lock-on is characterized by a peak at the forcing frequency, $S_w \approx S_f$. Therefore, the vortex shedding frequency has not yet locked-on to the cylinder oscillation frequency as suggested by the non-existence or non-dominance of peaks at $S_w/S_f = 1.0$. The vorticity contours over a complete cycle of cylinder oscillation are shown in Figure 4.4 for $S_f/S_0 = 0.5$. Over one half of a period of oscillation, $T/2$, one vortex is shed from the top and one is shed from the bottom in an alternating sequence. This pattern is classified as the 2S vortex shedding mode.

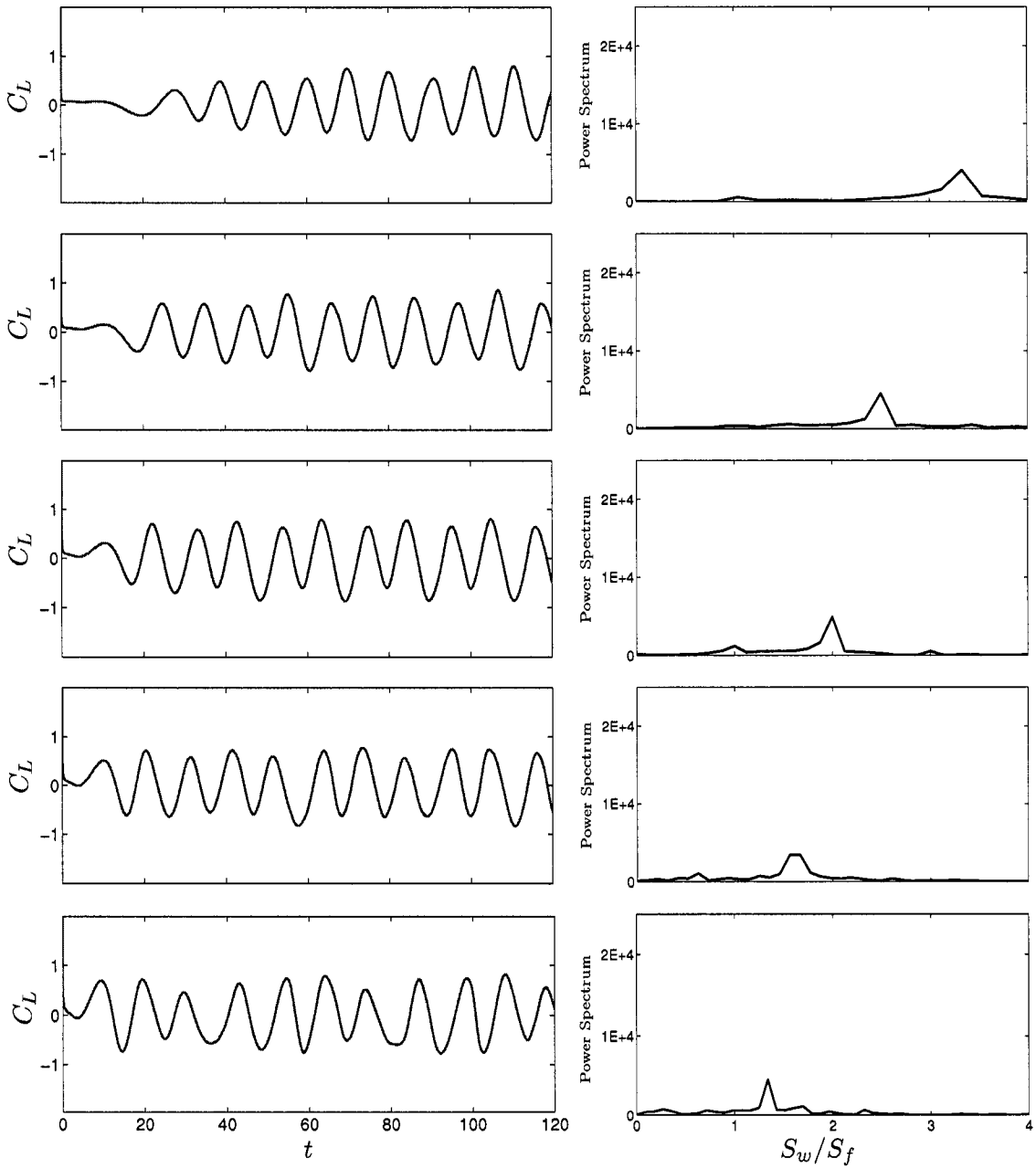

Figure 4.3: Lift coefficients and corresponding spectra for $R = 200$, $\eta = 45°$, $A = 0.5$ at S_f/S_0=0.3, 0.4, 0.5, 0.6, 0.7 (from top to bottom).

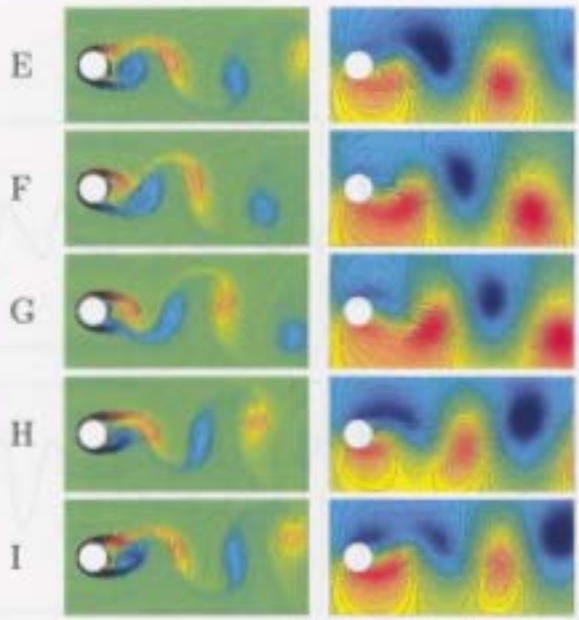

Figure 4.4: Vorticity contours at $R = 200$, $\eta = 45°$, $A = 0.5$, $S_f/S_0 = 0.5$ where the 2S vortex shedding mode persists in the near wake over half a period, $T/2$, of cylinder oscillation from E to I [$T = 20.47$, $92.12 \leq t \leq 102.35$].

4.2 Fundamental excitation for $R = 200$, $A = 0.5$, and $\eta = 45°$: $0.8 \leq S_f/S_0 \leq 1.2$

The next area of major interest is located in the range about $S_f/S_0 = 1.0$, corresponding to a fundamental excitation. At a forcing frequency of $S_f/S_0 = 0.8$, we note that there is no dominant peak in the spectra as shown in Figure 4.5. Then, as we increase the forcing frequency, a peak starts to develop at $S_w/S_f = 1$. In fact, with this increase we observe an amalgamation of the natural shedding and forcing frequencies when $S_f/S_0 = 0.9$. Finally, at $S_f/S_0 = 1.0$ we see a single dominant peak at $S_w/S_f = 1.0$ indicating that the near wake is locked-on to the cylinder oscillation frequency. A closer examination of the equi-vorticity contours and streamlines given in Figure 4.6 over one period, T, of cylinder oscillation confirms that there is lock-on at this forcing frequency.

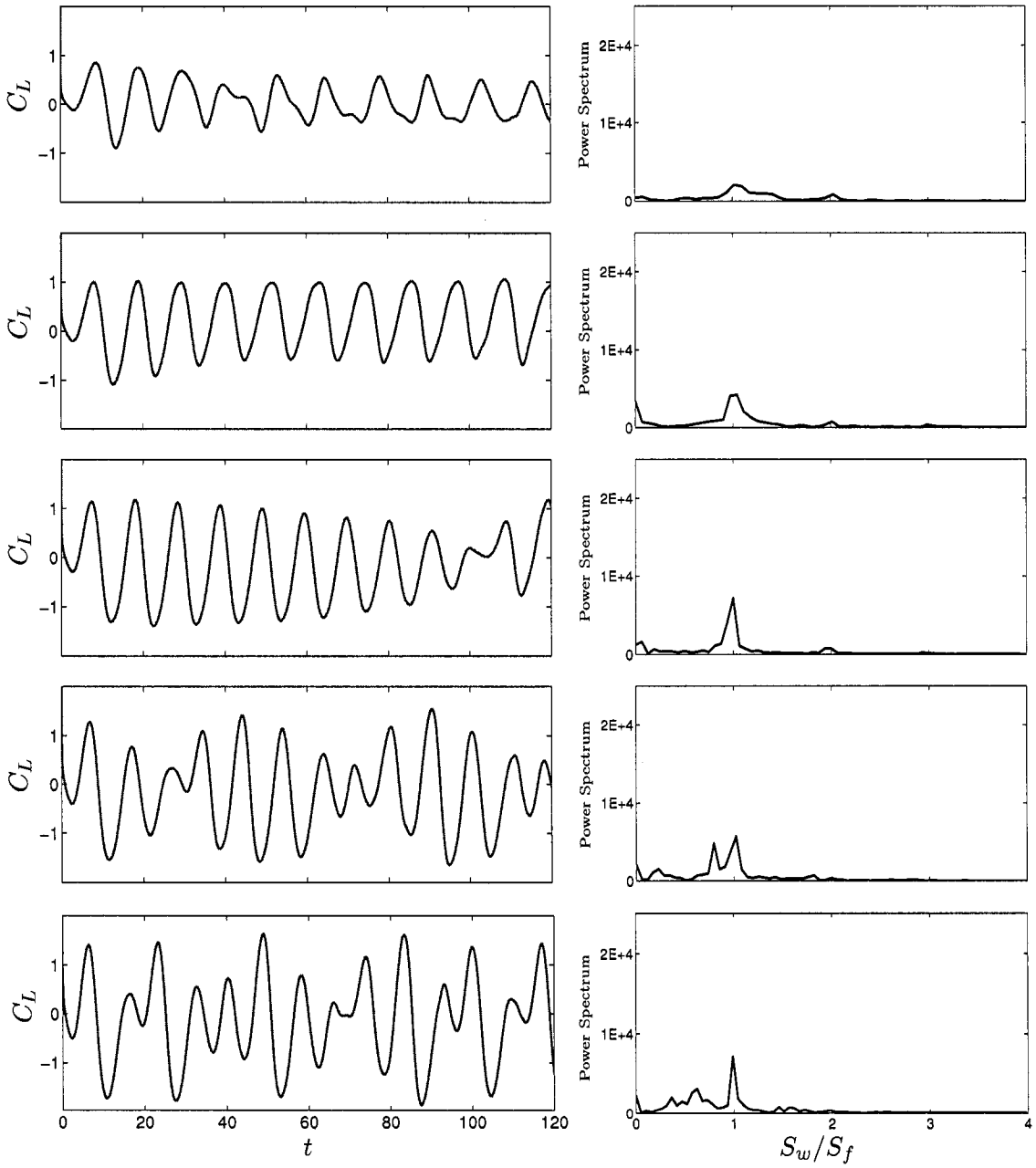

Figure 4.5: Lift coefficients and corresponding spectra for $R = 200$, $\eta = 45°$, $A = 0.5$ at S_f/S_0=0.8, 0.9, 1.0, 1.1, 1.2 (from top to bottom).

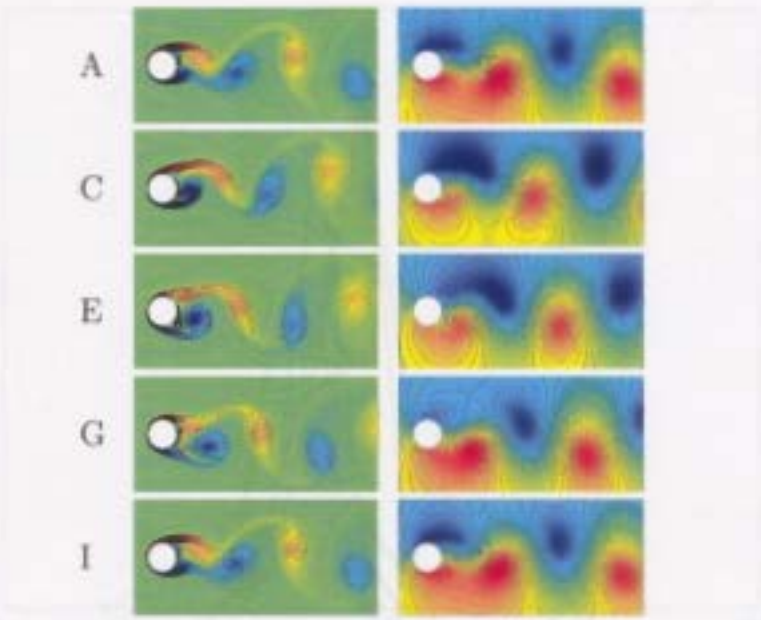

Figure 4.6: Vorticity contours at $R = 200$, $\eta = 45°$, $A = 0.5$, $S_f/S_0 = 1.0$ where we have a fundamental lock-on of the 2S vortex shedding mode over one period, T, of cylinder oscillation from A to I [$T = 10.24$, $82.92 \leq t \leq 92.16$].

Increasing the forcing frequency slightly to $S_f/S_0 = 1.1$ we observe that a strong beating pattern has formed in the lift coefficient. The reason for this beating is explained in the power spectrum (see Figure 4.5) where it is evident that the forcing frequency is dominant at $S_w/S_f = 1.0$, but the natural shedding frequency S_0 is still very strong. In fact, for fundamental lock-on to occur, the natural shedding frequency must be suppressed.

To determine the precise interval of fundamental lock-on it is necessary to conduct more simulations in the region $0.9 < S_f/S_0 < 1.1$. At this point, we may exclude the endpoints $S_f/S_0 = 0.9$ and 1.1 since lock-on has not been observed at these frequencies. After conducting these simulations we conclude from the lift coefficients and corresponding spectra seen in Figure 4.7 that the fundamental lock-on range is $0.92 \leq S_f/S_0 \leq 1.02$, which is accurate to two decimal places. The power spectra of the lift coefficients are plotted in this figure for $S_f/S_0 = 0.91, 0.92, 1.0, 1.02$, and 1.03 without the scaling factor S_f. For $S_f/S_0 = 0.91 < 0.92$, the peak in the spectra

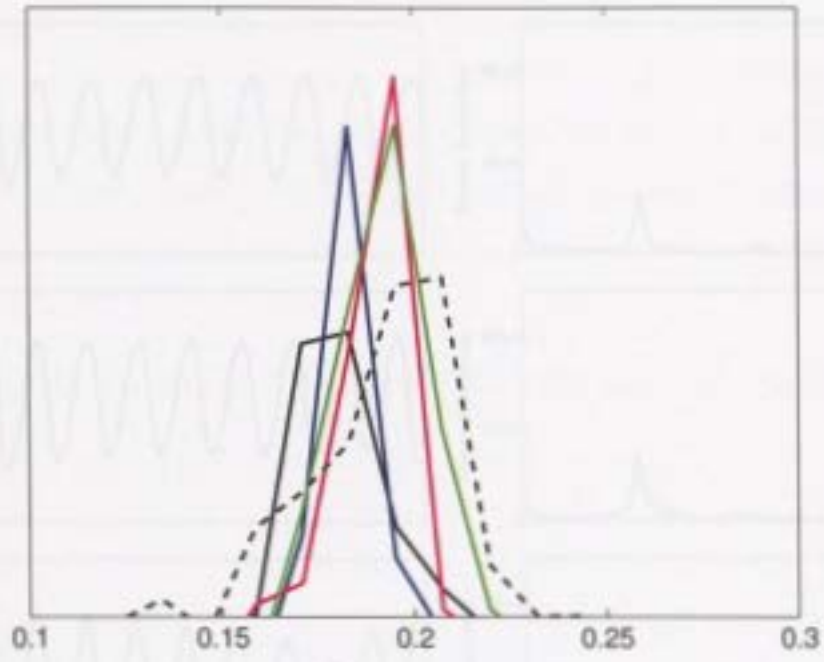

Figure 4.7: Power spectra of lift coefficients for $R = 200$, $A = 0.5$, $\eta = 45°$, and $S_f/S_0 = 0.91$ (—); 0.92 —; 1.0 (—); 1.02 (—); 1.03 (---).

near S_0 is actually a combination of the two dominant frequencies, namely the natural and forcing frequencies. Once the forcing frequency enters the lock-in zone at $S_f/S_0 = 0.92$ we observe a single peak in the spectra which moves from left to right as the forcing frequency is increased. Numerical experimentation shows that when $S_f/S_0 = 1.03$, the single peak breaks apart again into the two individual frequencies, thus determining the end of the lock-in zone. Therefore, the fundamental lock-on regime is $0.92 \leq S_f/S_0 \leq 1.02$ for $R = 200$, $A = 0.5$, and $\eta = 45°$.

One of the most interesting features which was observed for the case of transverse oscillations is the transition of the lift within the fundamental lock-on regime [see Guilmineau and Queutey (2002)]. In the beginning of the region, the lift is a nice sinusoidal curve. However, over the small lock-on interval a beating pattern develops. This phenomenon is also observed in our simulations at $\eta = 45°$. The lift coefficient from $S_f/S_0 = 0.92$ to $S_f/S_0 = 1.1$ shows clearly the development of the beating as seen in Figure 4.8. For a forcing frequency of $S_f/S_0 = 0.92$-0.95, the periodic nature

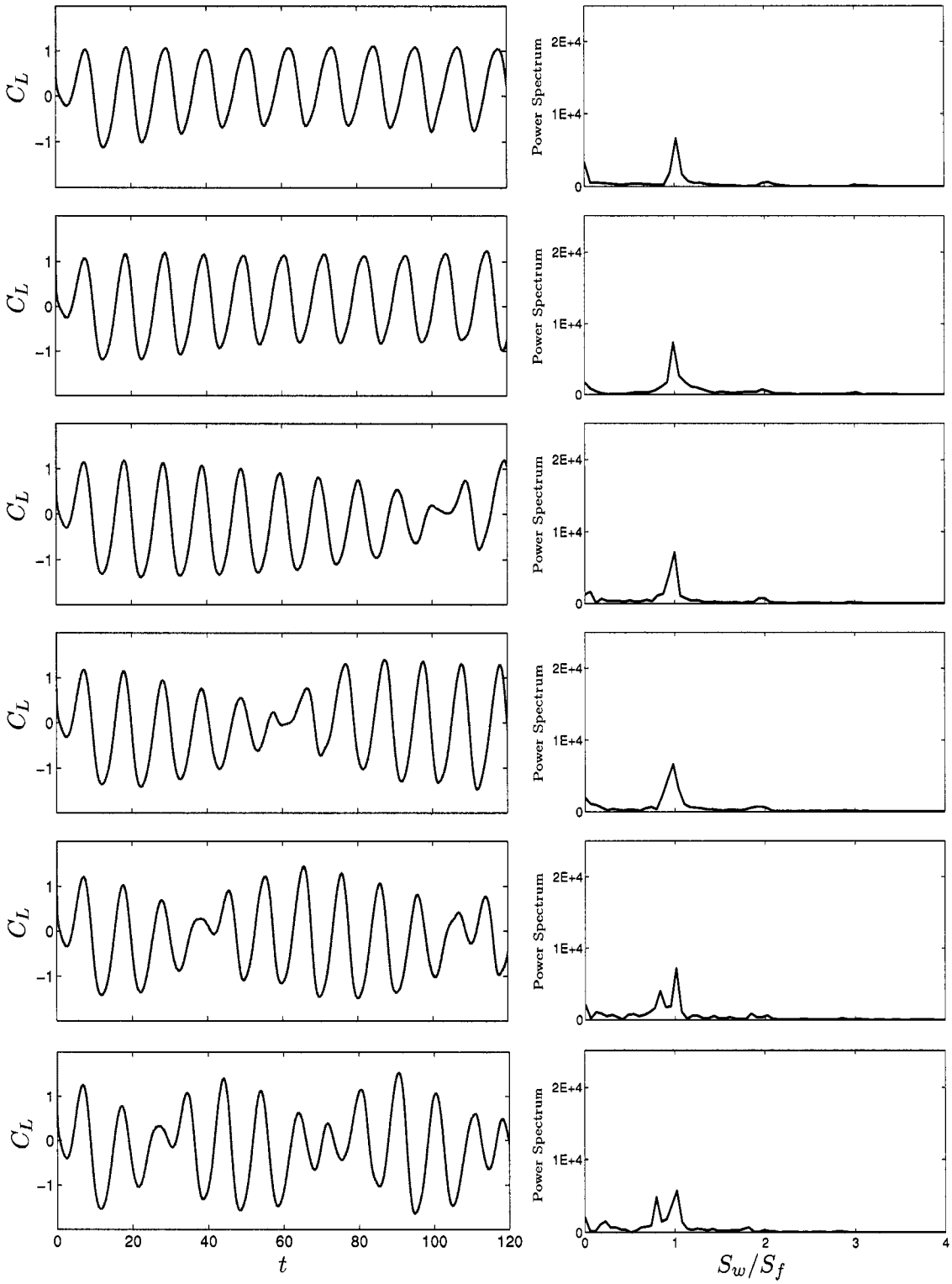

Figure 4.8: Development of the lift coefficient for $R = 200$, $\eta = 45°$, $A = 0.5$, at $S_f/S_0 = 0.92$, 0.95, 1.0, 1.02, 1.05, 1.1 (from top to bottom).

of the lift is preserved. Then, at $S_f/S_0 = 1.0$ a single beat develops in the lift which is followed again by a periodic curve. A slight increase of the forcing frequency to $S_f/S_0 = 1.02$ shifts the beat in the lift curve to the left and for $S_f/S_0 = 1.0$ we observe aa clearly defined beating period. Each increase thereafter leads to a successive decrease of the beating period up until $S_f/S_0 = 1.1$.

4.3 2-superharmonic excitation for $R = 200$, $A = 0.5$, and $\eta = 45°$: $1.2 \leq S_f/S_0 \leq 2.2$

The next range of frequency values that we will consider is in the superharmonic excitation regime near $S_f/S_0 = 2$. The lift coefficients and corresponding spectra for this case are given in Figure 4.9 for forcing frequency values from $S_f/S_0 = 1.8$ to $S_f/S_0 = 2.2$. For $S_f/S_0 \leq 2.0$, it is immediately evident from the spectrum that there are several frequencies dominant in the lift curve. As a result, based on the classical definition, there could not be any lock-on since a single peak is not evident in the spectra, as is the case in the fundamental regime.

However, the determination of lock-on is not confined to the analysis of the lift coefficient. For example, Ongoren and Rockwell (1988a,b), do not analyze the behavior of fluid forces and therefore it is impossible for them to observe the dominant frequencies in the near wake. Their classification of lock-on regimes is based on observations made throughout the vortex shedding cycle. If the near wake region is repeated in time, then lock-on is confirmed. For instance, consider the results for $S_f/S_0 = 1.8$ shown in Figure 4.9. This figure indicates that the lift coefficient is periodic over two periods, $2T$, of cylinder oscillation and has a spectrum with two major peaks. Although these two peaks exist in the spectra, the vorticity contours, as shown in Figure 4.10, clearly confirm that the vortex shedding is locked-on over two periods, $2T$, of oscillation in the near wake. Thus, in this thesis, we will take the near wake vorticity contours and streamlines into account before excluding a frequency value from the lock-on range.

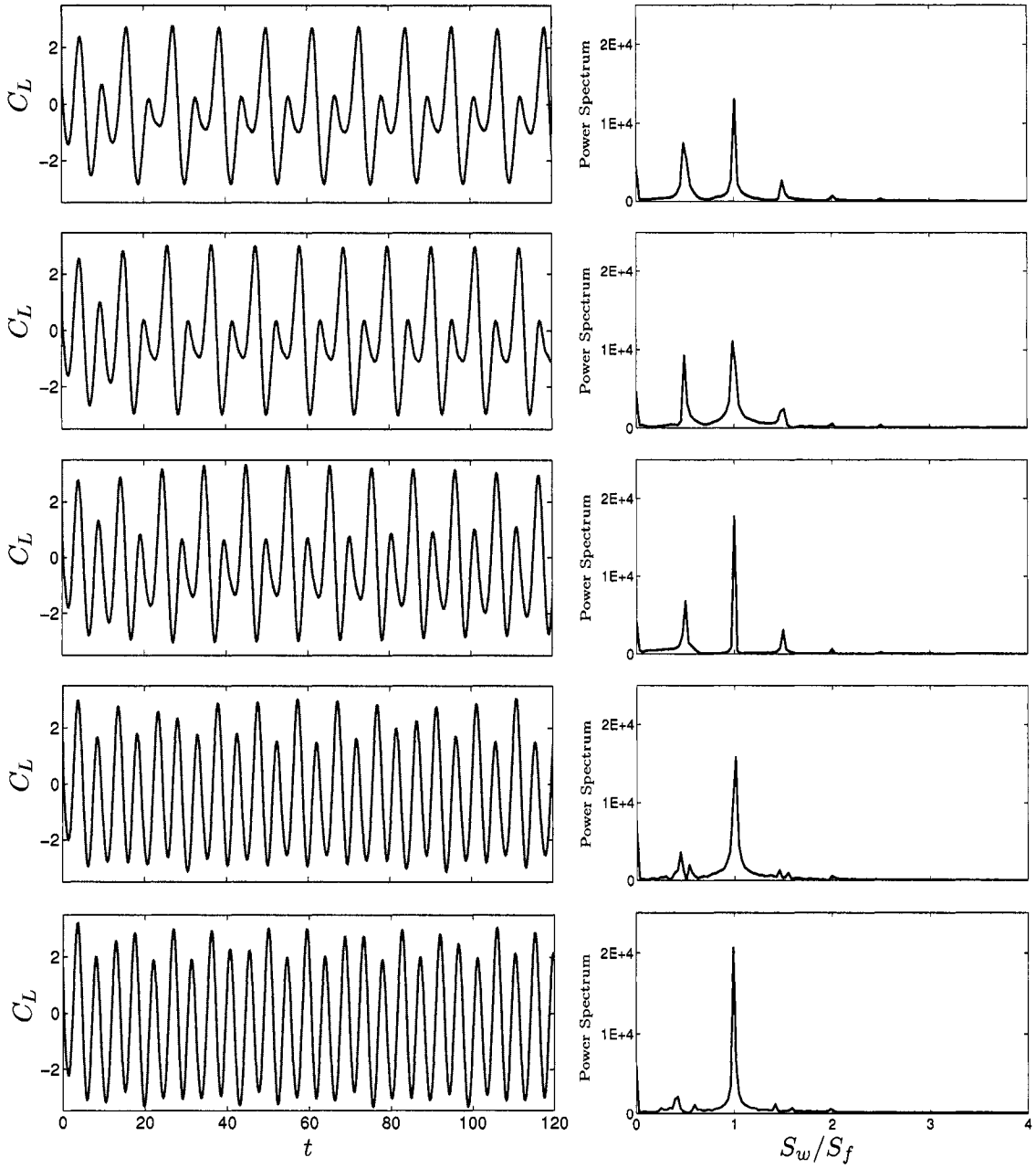

Figure 4.9: Lift coefficients and corresponding spectra for $R = 200$, $\eta = 45°$, $A = 0.5$ at $S_f/S_0 = 1.8$, 1.9, 2.0, 2.1, 2.2 (from top to bottom).

In addition, we note that we are not defining lock-on as the range in which a single frequency dominates the wake. Instead, two or three dominant frequencies may be present in the spectra. The most important property of lock-on is that the vortex shedding is synchronized with the cylinder oscillation period or some integer multiple of it. In this way, we are allowing different waveforms and vortex shedding modes to be classified as lock-on. Without this addition to the definition of lock-on, the P+S lock-on modes described by Williamson and Roshko (1988) would not exist. As a side, note that when classifying modes of vortex shedding we are only considering the near wake region, as did Ongoren and Rockwell (1988a,b), while using the notation of Williamson and Roshko (1988).

Using this analysis we can immediately classify the results for $S_f/S_0 = 1.8, 1.9$, and 2.0 as lock-on based on the vorticity contours shown in Figures 4.10-4.12. These figures show that the vortex shedding cycle is repeated over two periods, $2T$, of cylinder oscillation - referred to as the period doubling phenomenon. At $S_f/S_0 = 1.8$ and 1.9, this period doubling is well defined in the lift curve as shown in Figure 4.9. However, as we increase the forcing frequency this figure clearly indicates that the amplitude difference between the two local maxima gets smaller and smaller. At $S_f/S_0 = 2.0$, the two maxima are still distinguishable, but as we increase the frequency further the series of amplitude repetitions is no longer periodic. In the associated spectra for $S_f/S_0 = 1.8$-2.0, the two largest peaks represent the dominant forcing frequency at $S_w/S_f = 1.0$ and the natural shedding frequency at $S_w/S_f = 0.5$. Moreover, the period doubling in the lift coefficient is a result of the competition between the two frequencies. As the forcing frequency is increased beyond $S_f/S_0 = 2.0$ to $S_f/S_0 = 2.1$, we observe that the peak corresponding to the natural shedding frequency is suppressed, leaving only the peak at $S_w/S_f = 1.0$ corresponding to the superharmonic excitation frequency $S_f/S_0 = 2.1$. Hence, the properties of the flow above and below $S_f/S_0 = 2.1$ are obviously different. More precise bounds on the lock-on range are now investigated.

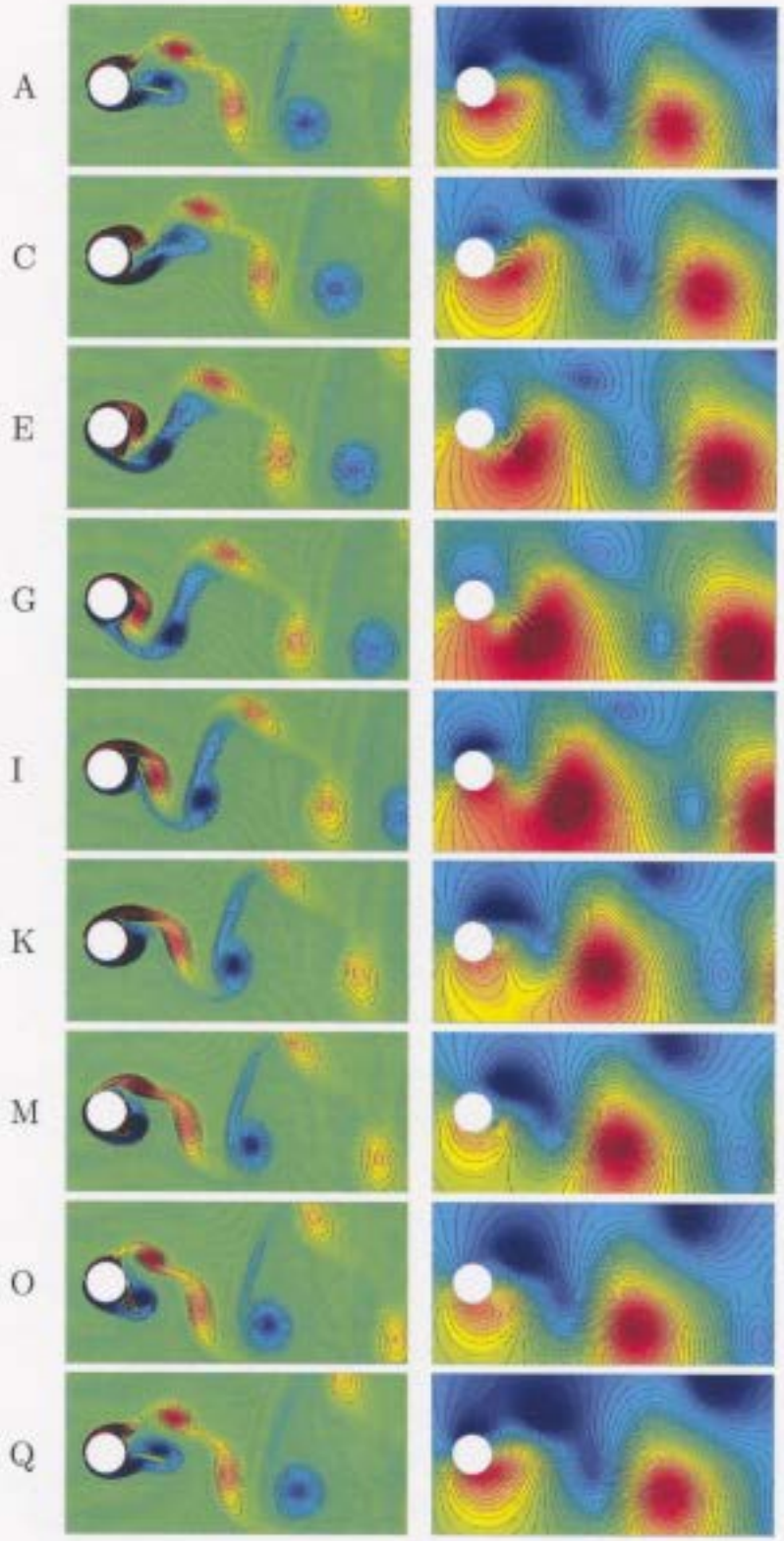

Figure 4.10: Vorticity contours at $R = 200$, $\eta = 45°$, $A = 0.5$, $S_f/S_0 = 1.8$ where we have a lock-on of the P+S vortex shedding mode over two periods, $2T$, of cylinder oscillation from A to Q [$T = 5.69$, $90.98 \leq t \leq 102.35$].

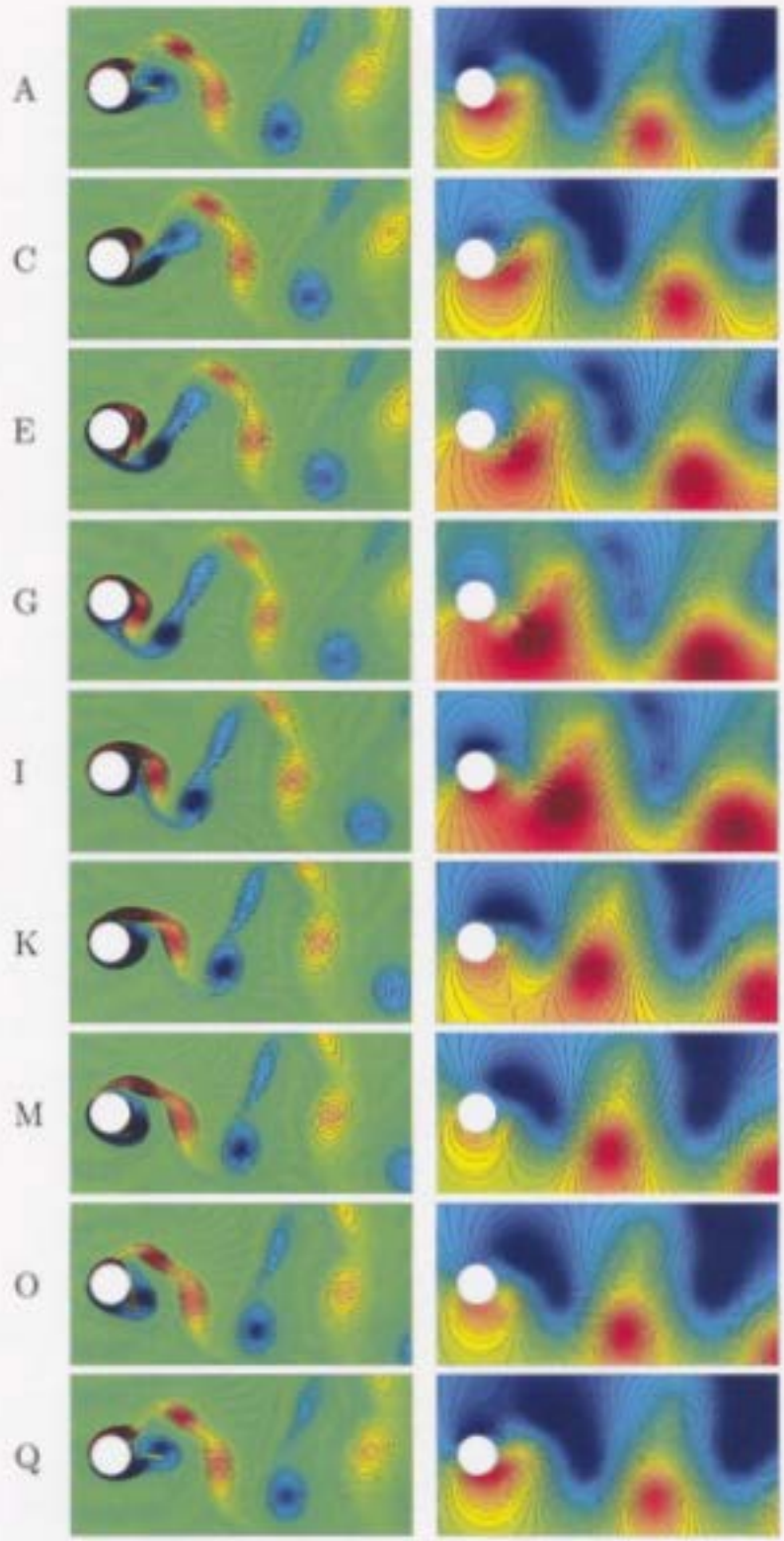

Figure 4.11: Vorticity contours at $R = 200$, $\eta = 45°$, $A = 0.5$, $S_f/S_0 = 1.9$ where we have a lock-on of the 2P vortex shedding mode over two periods, $2T$, of cylinder oscillation from A to Q [$T = 5.39$, $86.19 \leq t \leq 96.97$].

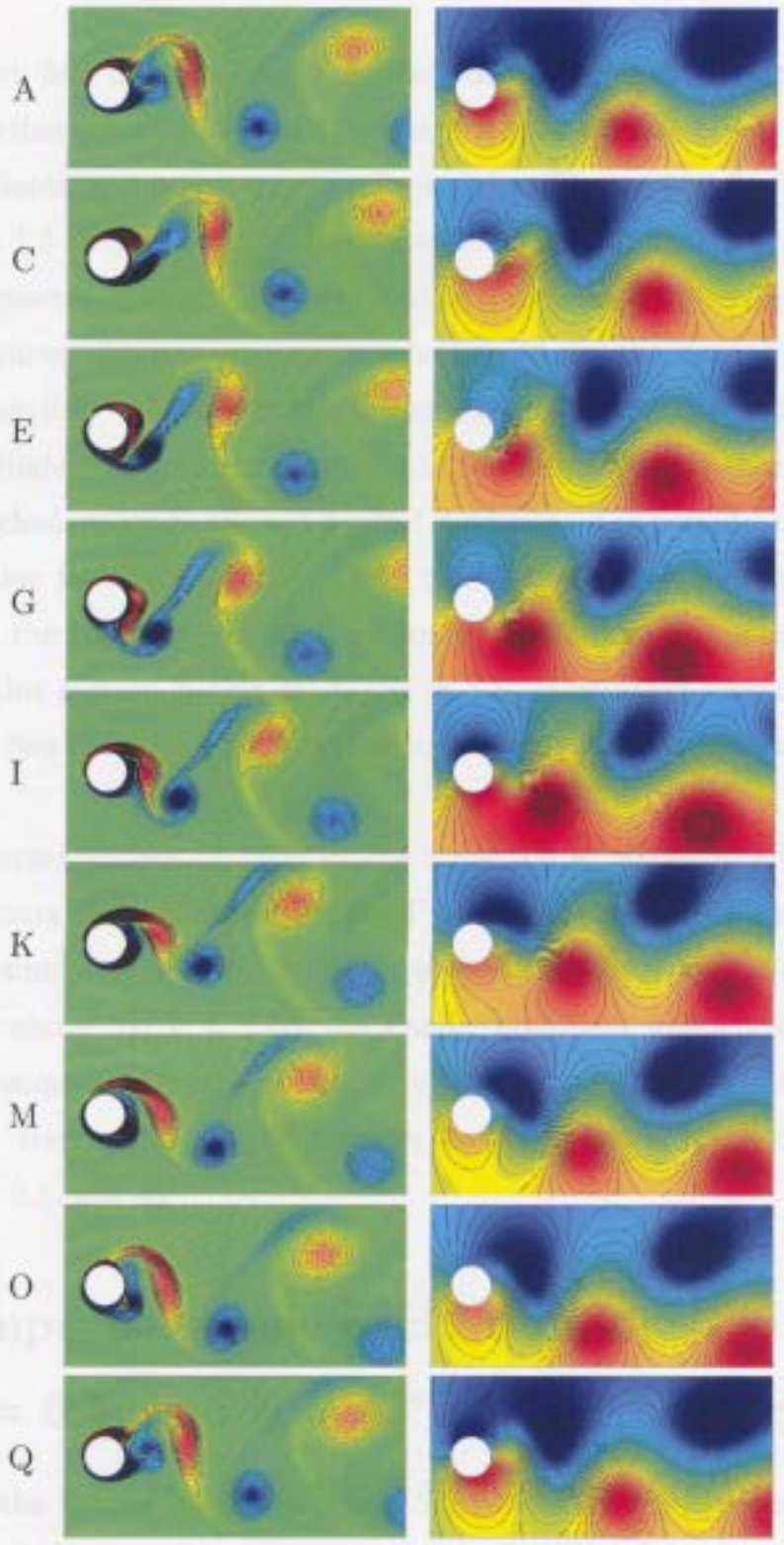

Figure 4.12: Vorticity contours at $R = 200$, $\eta = 45°$, $A = 0.5$, $S_f/S_0 = 2.0$ where we have a lock-on of the P+S vortex shedding mode over two periods, $2T$, of cylinder oscillation from A to Q [$T = 5.12$, $81.88 \leq t \leq 92.12$].

First, we must find a lower bound for lock-on in the 2-superharmonic excitation regime. A further investigation of this range is now performed by first considering the lift coefficients and power spectra displayed in Figure 4.13 for frequency values from $S_f/S_0 = 1.3$ to $S_f/S_0 = 1.7$. In this series of graphs, we observe two dominant peaks in the spectra in nearly all cases, but it is difficult to determine lock-on solely from these figures. To confirm/negate whether or not the near wake is locked-on, we plot the vorticity contours at the beginning and end of one and two periods, T and $2T$, of cylinder oscillation in Figure 4.14. Evident in this figure is that the near wake is not locked-on for $S_f/S_0 = 1.3$ and 1.4 whereas it is periodic over two periods, $2T$, of oscillation for $S_f/S_0 = 1.5$, 1.6 and 1.7. Therefore, after considering both the lift curve and the vorticity contours, we conclude that the 2-superharmonic lock-on discussed in this section begins at $S_f/S_0 = 1.5$. The synchronization of vorticity contours over two periods, $2T$, of oscillation confirms this lower bound.

The 2-superharmonic lock-on ends in the range $2.0 < S_f/S_0 \leq 2.1$ since the equi-vorticity contours are not repeated over T or $2T$ as shown in Figure 4.15 By conducting more simulations in this range we were able to determine that as we increase the frequency above $S_f/S_0 = 2.06$, the smaller dominant frequencies in the spectra begins to decompose into several smaller contributions, resulting in the end of the lock-in range. Hence, the 2-superharmonic lock-on range is $1.5 \leq S_f/S_0 \leq 2.06$ for $R = 200$, $A = 0.5$, $\eta = 45°$.

4.4 3-superharmonic excitation for $R = 200$, $A = 0.5$, and $\eta = 45°$: $2.8 \leq S_f/S_0 \leq 3.2$

For values of the forcing frequency above $S_f/S_0 = 2.5$ the structures forming in the near wake are difficult to characterize due to the fact that the velocity ratio is becoming large. In fact, the velocity amplitude of the forced oscillations is $\alpha = \pi S_f A \approx 1$

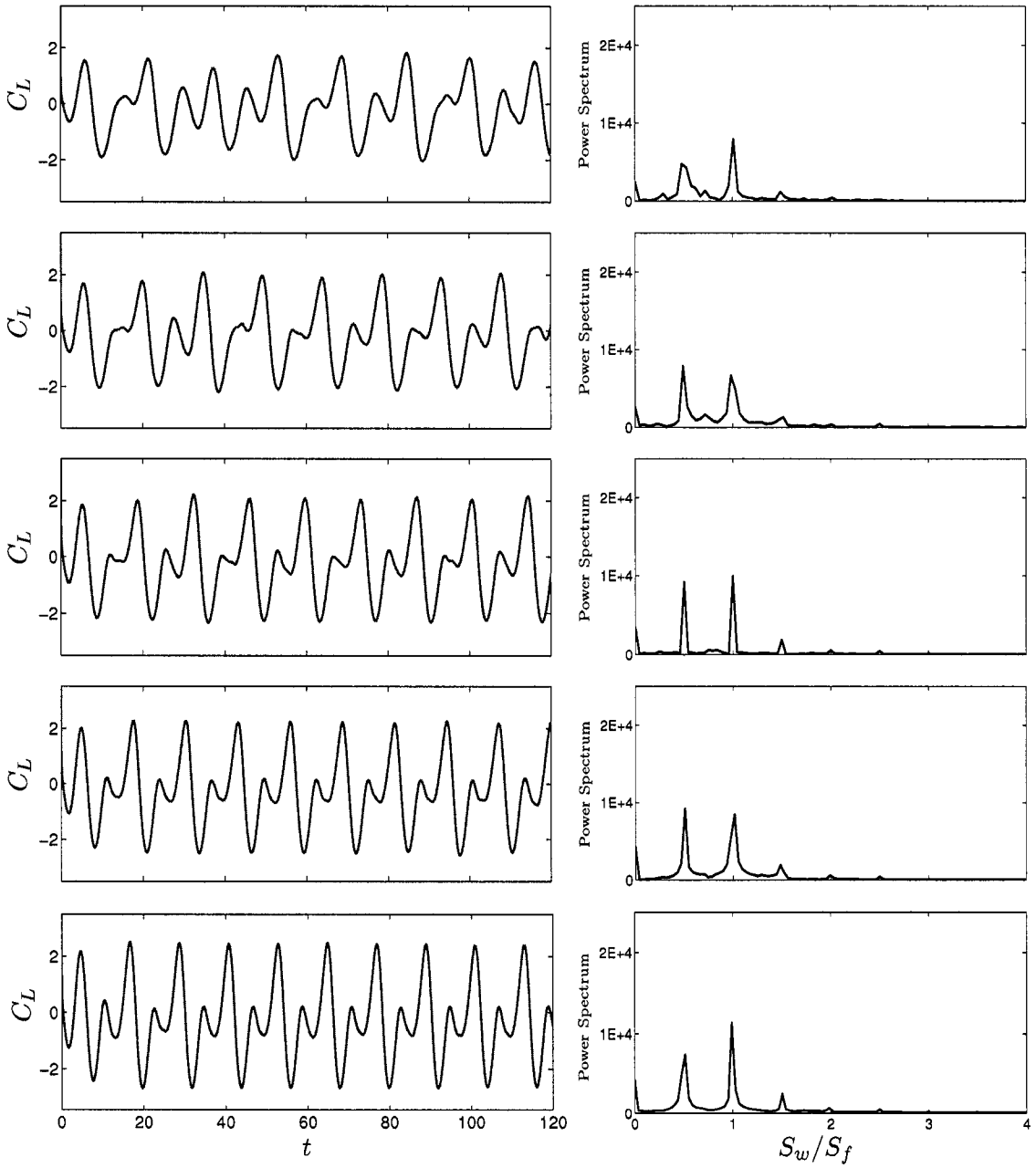

Figure 4.13: Lift coefficients and corresponding spectra for $R = 200$, $\eta = 45°$, $A = 0.5$ at $S_f/S_0 = 1.3$, 1.4, 1.5, 1.6, 1.7 (from top to bottom).

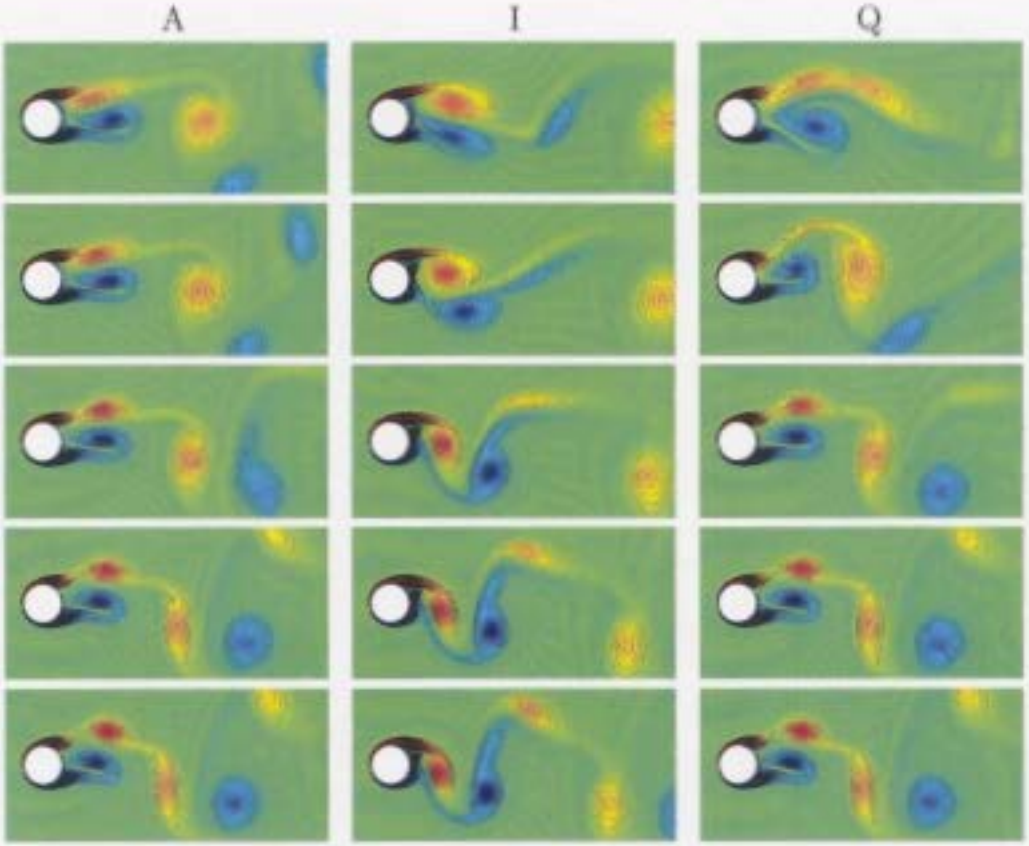

Figure 4.14: Vorticity contours at $R = 200$, $\eta = 45°$, $A = 0.5$, $S_f/S_0 = 1.3$, 1.4, 1.5, 1.6, and 1.7 (from top to bottom) at the beginning (position A, $t = 16T$) and end on one (position I, $t = 17T$) and two periods (position Q, $t = 18T$) of cylinder oscillation [$T = 2/S_f$, $S_0 = 0.1954$].

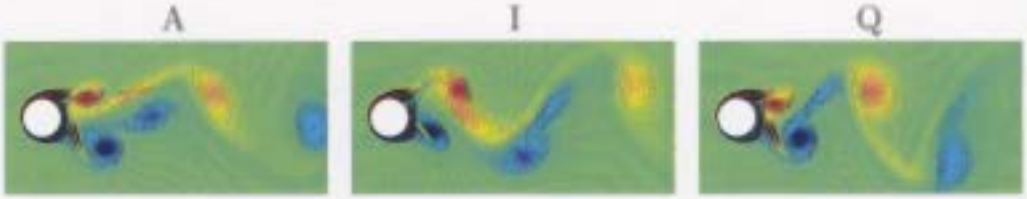

Figure 4.15: Instantaneous vorticity contours at $R = 200$, $\eta = 45°$, $A = 0.5$, $S/S_0 = 2.1$ over two periods, $2T$, of cylinder oscillation at positions A ($t = 77.98$), I (one period later, $t = 82.86$), and Q (two periods later, $t = 87.73$). [$T = 4.87$].

for values of the excitation frequency near the 3-superharmonic regime. The lift coefficient and corresponding spectra for this case are given in Figure 4.16 for frequency values in the range $2.8 \leq S_f/S_0 \leq 3.2$. We observe in each of these cases that there is one large peak in the spectra at $S_w/S_f = 1.0$ corresponding to the forcing frequency, and a smaller peak at $S_w/S_f = 0.33$, corresponding to the natural shedding frequency. Thus, the flow is dominated by the large oscillation to translation velocity ratio, α, of the cylinder. Comparing the lift coefficients we observe that all forcing frequency values have approximately the same behavior. The period between two consecutive instances where the lift passes through zero from negative to positive is approximately the same as the oscillation period. However, the amplitude of the lift coefficient changes slightly from period to period.

To better understand why the aperiodic changing of the amplitude occurs, we plot the equi-vorticity contours and streamlines in Figure 4.17 for $S_f/S_0 = 3.0$. The contours indicate that very close to the cylinder surface the vorticity patterns are approximately the same at the beginning and end of one period of cylinder oscillation. To clarify, in Figure 4.18 we present a larger view of these contours near the cylinder surface at the beginning and end of once period of oscillation. The collection of the previously shed vortices in the near wake, however, are different from period to period. The result is an unequal contribution from previously shed vortices to the lift coefficient during each period, and consequently varying amplitudes in the curve.

Hence, we conclude that lock-on does occur near $S_f/S_0 = 3.0$ for an amplitude of $A = 0.5$ in the near wake region. In this case, the cylinder oscillation is moderately large and thus, as the set of vortices shed in the one period attempts to move downstream, the cylinder has already changed direction and returned to its maximum oscillatory displacement at position G. As a result, the cylinder in this case acts as a mechanism which pushes and pulls on the fluid where major concentrations of vorticity already exists. A precise range of lock-on cannot be determined in this thesis

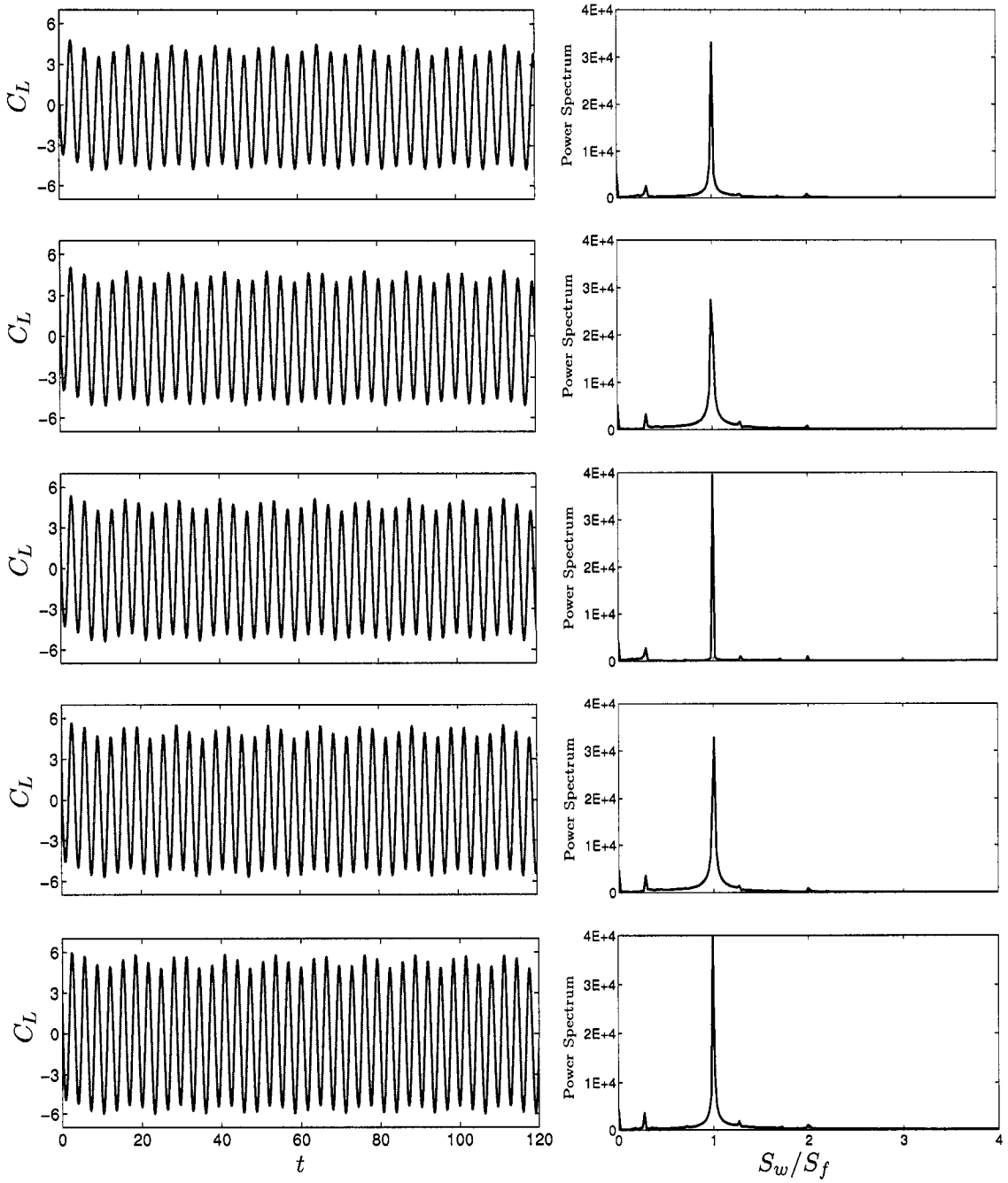

Figure 4.16: Lift coefficients and corresponding spectra for $R = 200$, $\eta = 45°$, $A = 0.5$ at $S_f/S_0 = 2.8$, 2.9, 3.0, 3.1, 3.2 (from top to bottom).

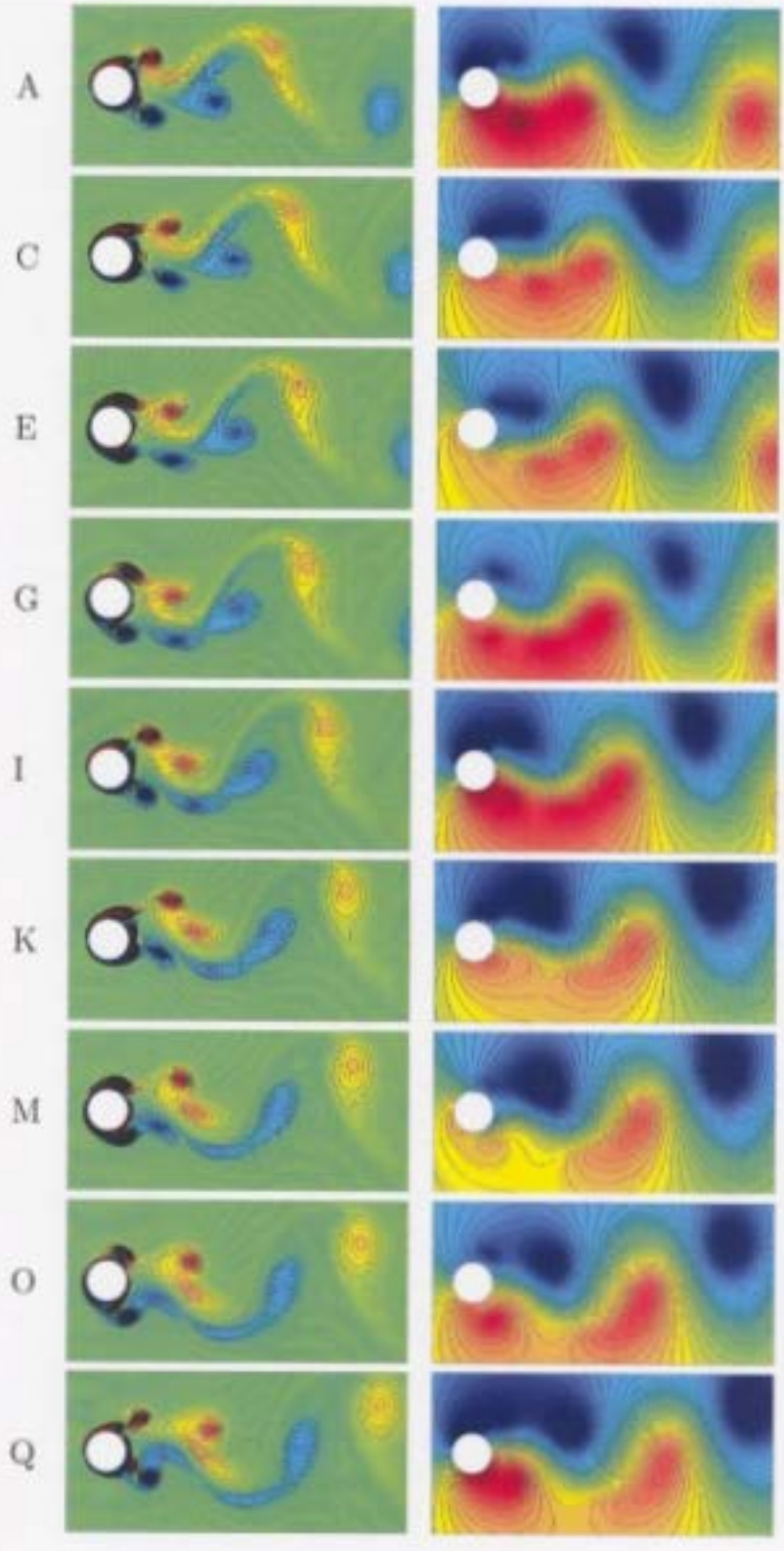

Figure 4.17: Vorticity contours at $R = 200$, $\eta = 45°$, $A = 0.5$, $S_f/S_0 = 3.0$ over two periods, $2T$, of cylinder oscillation [$T = 3.41$, $54.59 \leq t \leq 61.41$].

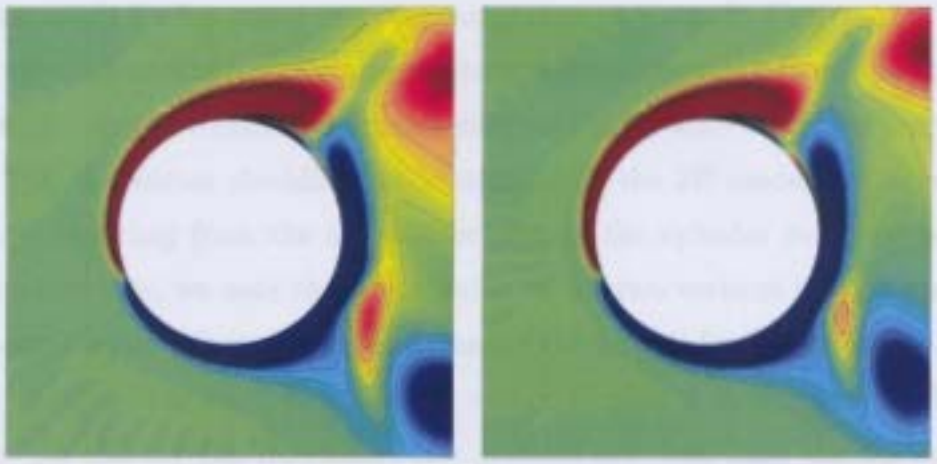

Figure 4.18: Vorticity contours at $R = 200$, $\eta = 45°$, $A = 0.5$, $S_f/S_0 = 3.0$ when cylinder displacement is zero at the beginning (position A, $t = 54.59$) and end (position I, $t = 58.00$) of one period [$T = 3.41$].

due to the complications in the near wake arising from the increased amplitude.

4.5 Preferred shedding modes during lock-on for $R = 200$, $A = 0.5$, $\eta = 45°$

The preferred mode of vortex shedding during lock-on are classified based on the analysis of Williamson and Roshko (1988). For S_f/S_0, in the fundamental lock-on range ($0.92 \leq S_f/S_0 \leq 1.02$), the mode of vortex shedding is the asymmetric 2S mode.

For frequency values in the range 2-superharmonic lock-on range, an interesting feature is captured in the vorticity contours given in Figures 4.10-4.12 for $S_f/S_0 = 1.8$, 1.9, and 2.0, respectively. Recall that the effect of the increasing frequency on the lift curve is to increase the smaller local maxima. However, in the vorticity contours we see a change in the preferred mode of vortex formation. At $S_f/S_0 = 1.8$, the

asymmetric mode P+S persists over the entire time domain. In Figure 4.10, over two cycles of cylinder oscillation, we observe two vortices shedding from the top of the cylinder and a single vortex of opposite rotation being shed from the bottom. At $S_f/S_0 = 1.9$, the vortex shedding mode changes to the 2P mode, characterized by two vortices shedding from the top and bottom of the cylinder over two periods of oscillation. However, we note that the smaller of the two vortices is weak and decays rapidly downstream. After a further increase of the forcing frequency to $S_f/S_0 = 2.0$, the wake then reverts back to the P+S vortex shedding mode, but in the opposite sense. At this forcing frequency, two vortices are shed from the bottom and a single vortex is shed from the top of the cylinder over two cylinder oscillation periods.

In the 3-superharmonic range ($S_f/S_0 = 3.0$), one vortex is shed from the top and bottom over one period of cylinder oscillation resulting in the 2S* mode. This is different than the 2S mode observed in the fundamental lock-on regime since the vortices in 2S* mode are shed at nearly the same time, forming a symmetric-like arrangement of the vortices immediately to the rear of the cylinder.

Chapter 5

Oblique Oscillations of a Circular Cylinder: Effect of the angle and amplitude of oscillation

In this chapter we continue our discussion of the flow past an obliquely oscillating cylinder at $R = 200$ with an emphasis on describing the effect of the amplitude and angle of oscillation. By varying one flow parameter (η, A, and S_f/S_0) individually, and keeping the other two fixed, the effect of each parameter on the near wake flow characteristics and force coefficients is determined. Intermediate angles of oscillations are chosen as $\eta = 15°, 30°$, 45°, 60°, and 75° and the amplitude varies from $A = 0.2$ to $A = 1.0$ when $S_f/S_0 = 0.5$, 1.0, and 2.0.

5.1 Effect of the angle and amplitude of oscillation on vortex modes and force coefficients at $R = 200$ and $S_f/S_0 = 0.5$

In this section we present the results for $R = 200$, $S_f/S_0 = 0.5$, when $15° \leq \eta \leq 75°$, and $A = 0.2$, 0.6, 1.0. At a frequency of $S_f/S_0 = 0.5$, the near wake is still dominated

by the natural shedding frequency at all amplitudes and angles considered in this thesis. This was also observed in Chapter 4 for $A = 0.5$ when $\eta = 45°$. The vorticity contours for $A = 0.2$, 0.6 and 1.0 when $15° \leq \eta \leq 75°$ are shown in Figures 5.1-5.3. In these figures the contours plotted over half a period, $T/2$, of cylinder oscillation depict the 2S mode of vortex shedding at all angles and amplitudes as a result of the dominant natural shedding frequency. Therefore, for this smaller frequency the effect of the angle and amplitude is minimal on the modes of vortex formation.

The lift and drag coefficients for this case are given in Figures 5.4-5.9, where we observe a beating period of $T/2$ in the lift and T in the drag. At the larger amplitude it is more evident that the amplitude of the drag decreases as the angle increases whereas very little change is observed in the lift. The unequal peaks that develop in the lift as we increase the amplitude of oscillation and decrease the angle is a direct result of the unequal concentrations of vorticity at the beginning and end of the half period, $T/2$, of oscillation. For streamwise and transverse oscillations of a circular cylinder, the displacement of the cylinder during each half period is symmetric about the horizontal or vertical axis. However, for oblique oscillations the movement of the cylinder during the first and second half periods is quite different in terms of the amount of horizontal/vertical movement in relation to the uniform flow. In one half of the period the cylinder is moving downward into the uniform stream, and in the second half it is moving upward away from the stream. Therefore, during each half period the 2S mode persists in the near wake, but the size of each vortex shedding on top and bottom from 0-$T/2$ and $T/2$-T varies as a result of the different movements. For this reason, we could refer to the period of vortex shedding as T instead of $T/2$ even though no major change in the nature of the shedding is evident. In this thesis, we continue to classify the shedding mode as 2S and simply point out this effect of the angle of oscillation.

Moreover, as suggested by the power spectra of the lift coefficient plotted along with

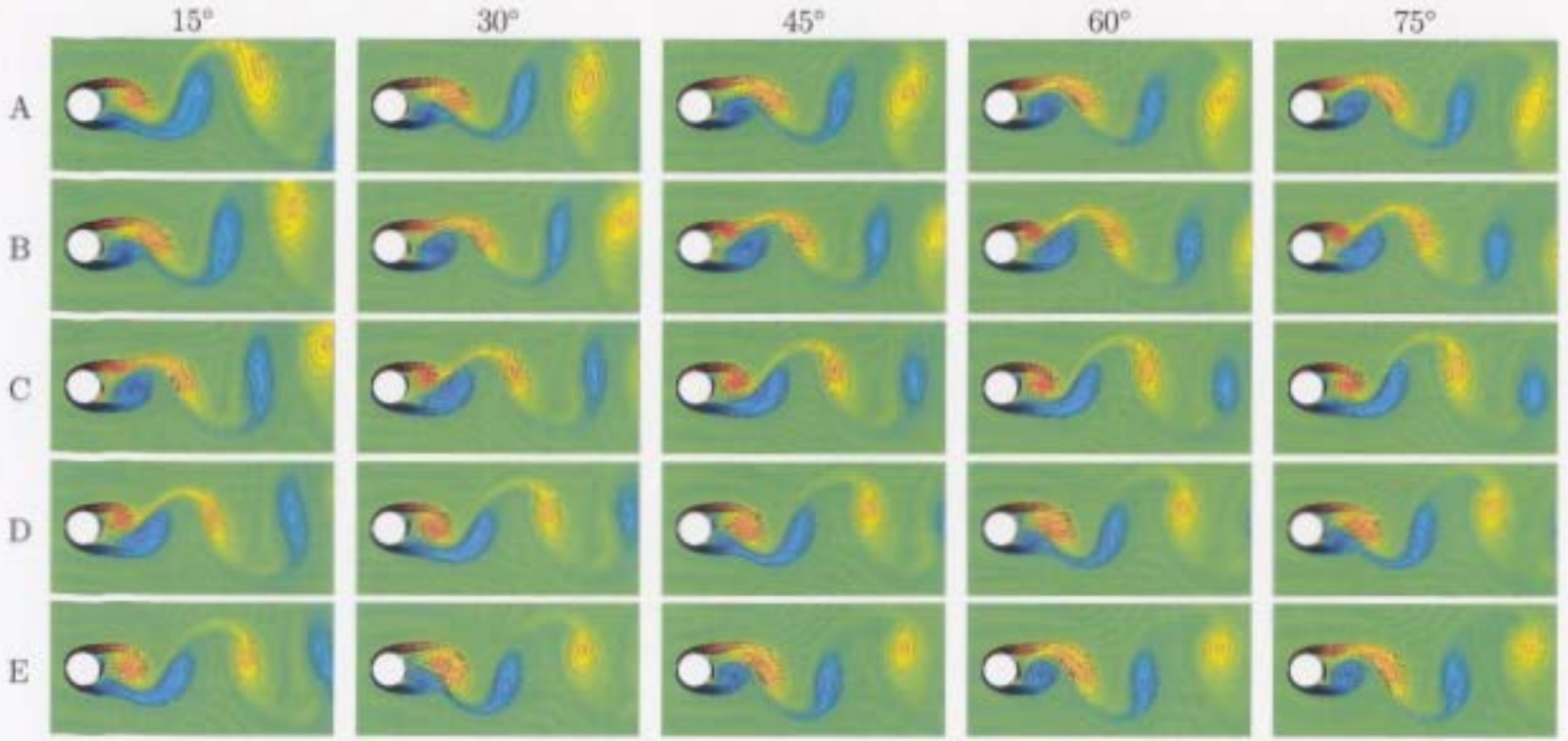

Figure 5.1: Vorticity contours for $R = 200$, $S_f/S_0 = 0.5$, $A = 0.2$ with $\eta = 15°$, $30°$, $45°$, $60°$, and $75°$ over half a period $(T/2)$ of cylinder oscillation $[T = 20.47,\ 81.88 \leq t \leq 92.12]$.

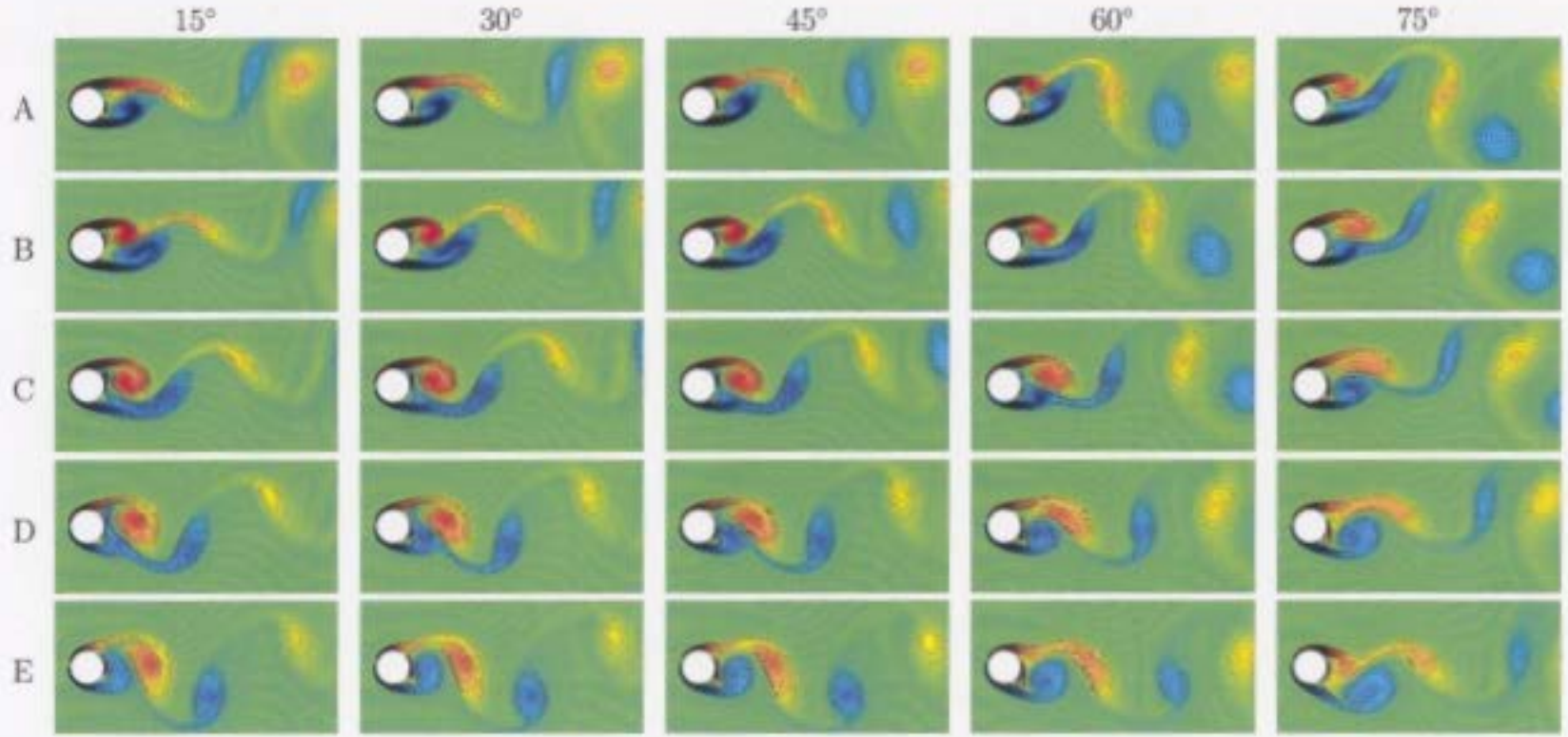

Figure 5.3: Vorticity contours for $R = 200$, $S_f/S_0 = 0.5$, $A = 1.0$ with $\eta = 15°$, $30°$, $45°$, $60°$, and $75°$ over half a period $(T/2)$ of cylinder oscillation $[T = 20.47,\ 81.88 \leq t \leq 92.12]$.

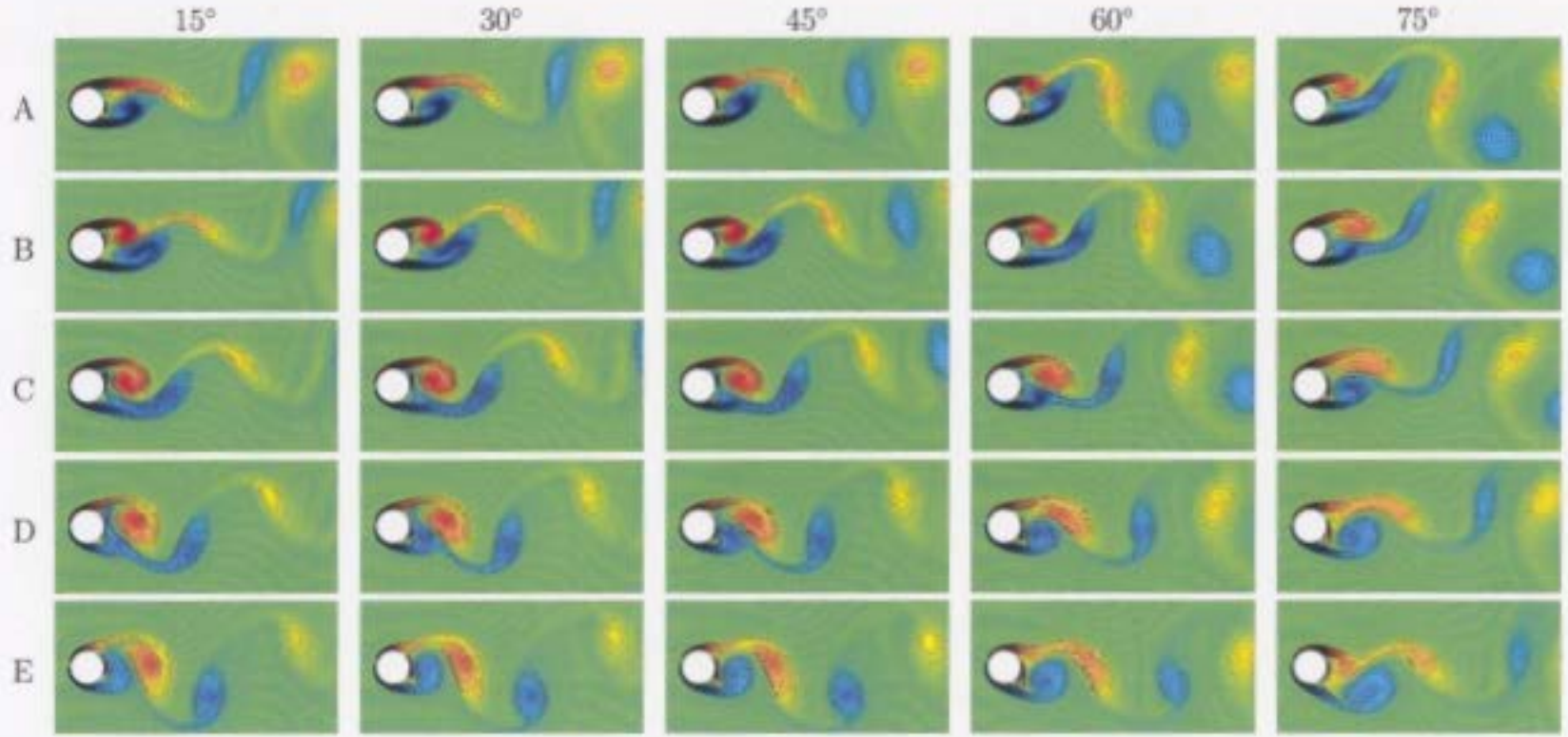

Figure 5.3: Vorticity contours for $R = 200$, $S_f/S_0 = 0.5$, $A = 1.0$ with $\eta = 15°$, $30°$, $45°$, $60°$, and $75°$ over half a period $(T/2)$ of cylinder oscillation $[T = 20.47,\ 81.88 \leq t \leq 92.12]$.

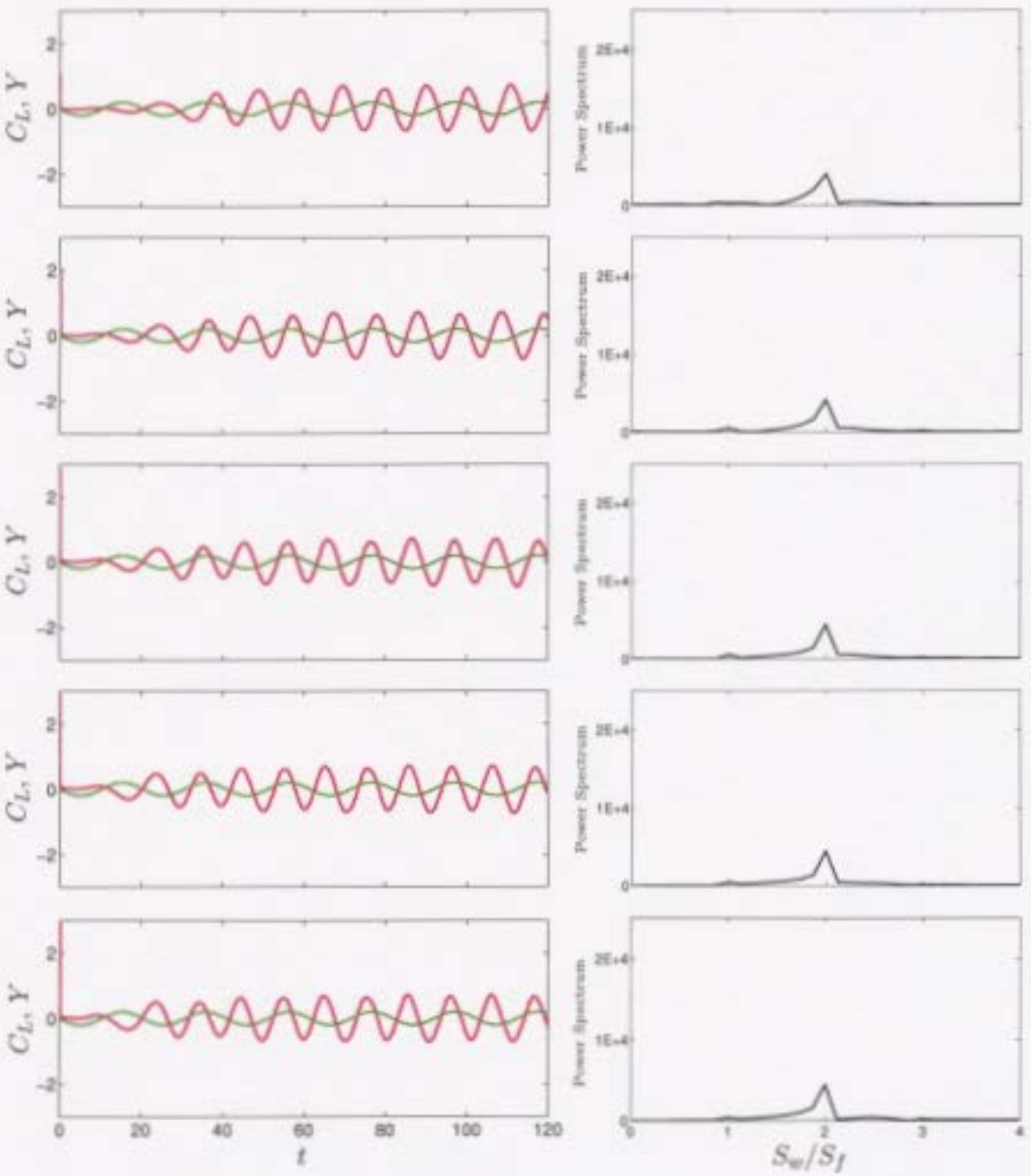

Figure 5.4: Lift coefficient (—) and cylinder displacement (—) with power spectrum of lift coefficient (right) for $R = 200$, $A = 0.2$, $S_f/S_0 = 0.5$ for angles of oscillation $\eta = 15°$, $30°$, $45°$, $60°$ and $75°$ (from top to bottom).

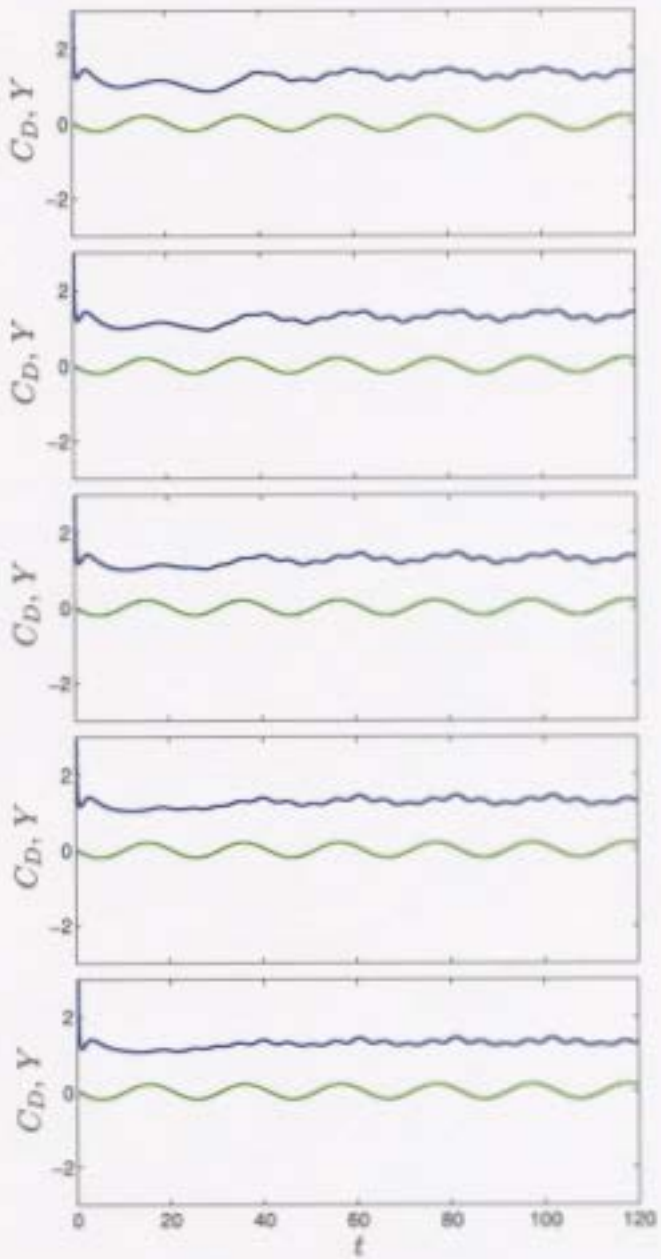

Figure 5.5: Drag coefficient (—) and cylinder displacement (—) for $R = 200$, $A = 0.2$, $S_f/S_0 = 0.5$ for angles of oscillation $\eta = 15°$, $30°$, $45°$, $60°$ and $75°$ (from top to bottom).

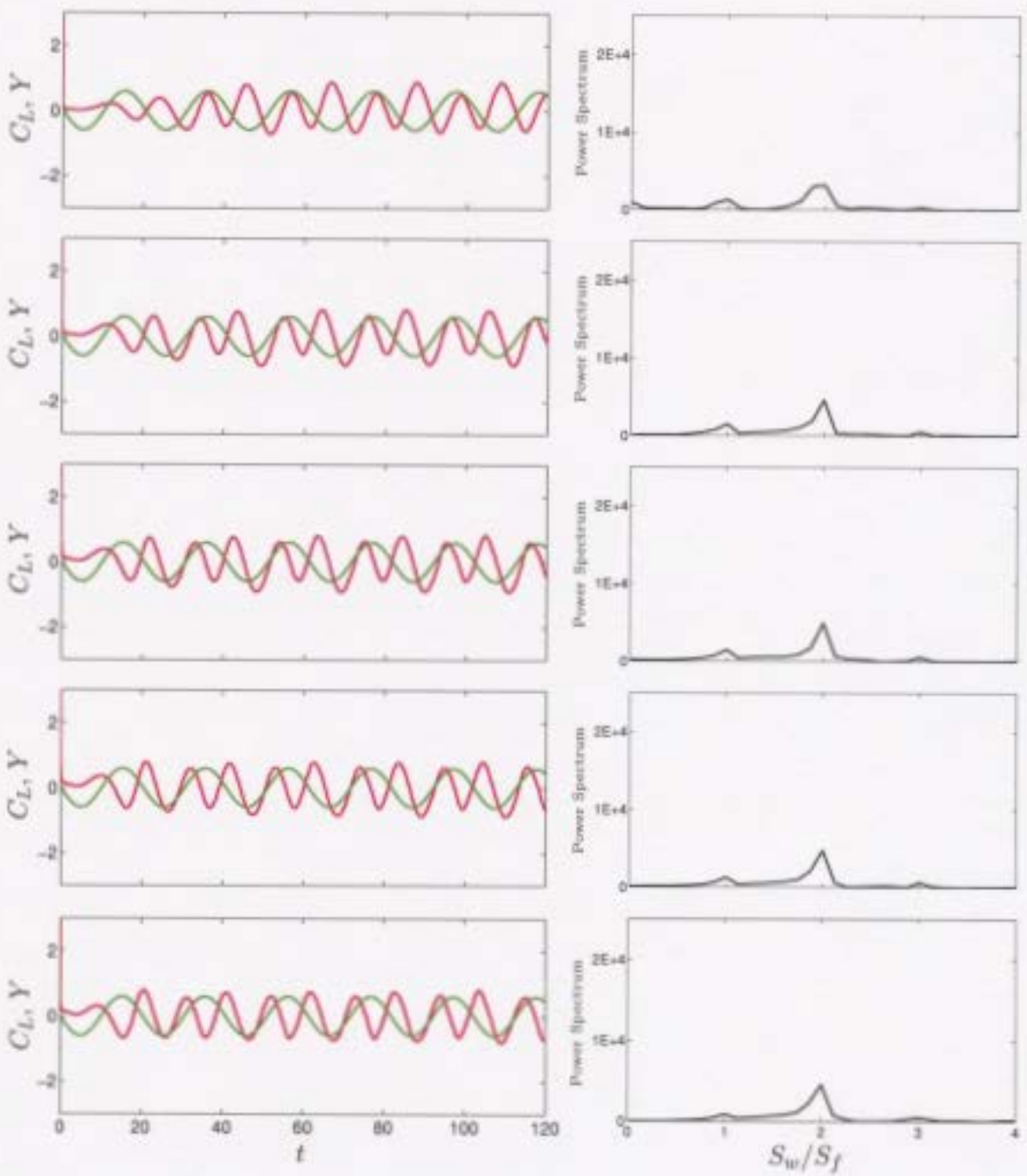

Figure 5.6: Lift coefficient (—) and cylinder displacement (—) with power spectrum of lift coefficient (right) for $R = 200$, $A = 0.6$, $S_f/S_0 = 0.5$ for angles of oscillation $\eta = 15°$, $30°$, $45°$, $60°$ and $75°$ (from top to bottom).

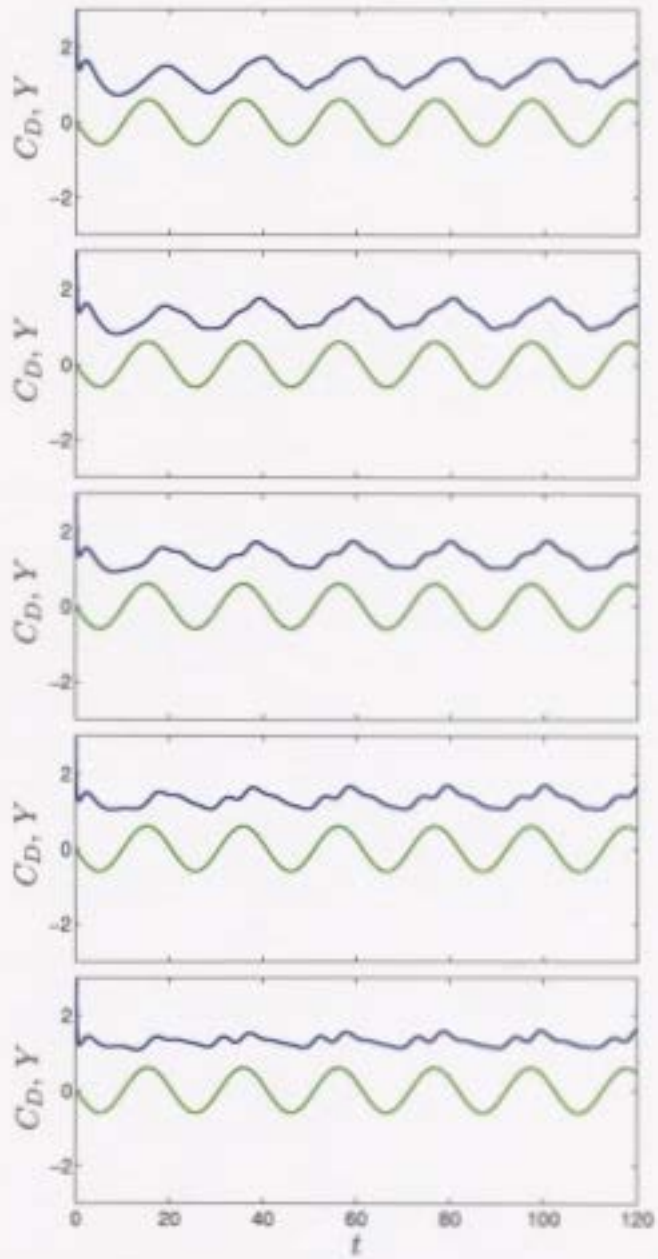

Figure 5.7: Drag coefficient (—) and cylinder displacement (—) for $R = 200$, $A = 0.6$, $S_f/S_0 = 0.5$ for angles of oscillation $\eta = 15°$, $30°$, $45°$, $60°$ and $75°$ (from top to bottom).

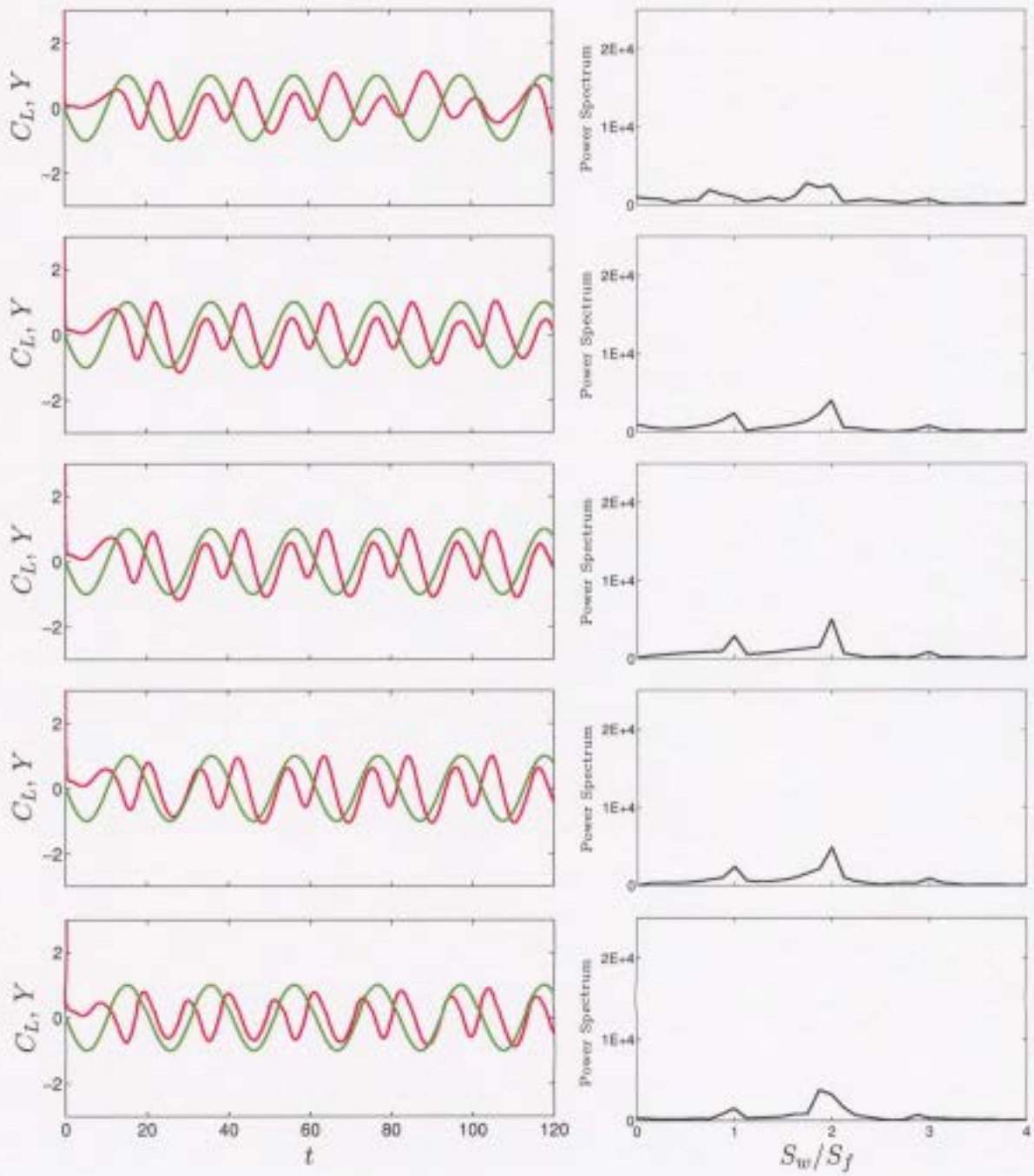

Figure 5.8: Lift coefficient (—) and cylinder displacement (—) with power spectrum of lift coefficient (right) for $R = 200$, $A = 1.0$, $S_f/S_0 = 0.5$ for angles of oscillation $\eta = 15°$, $30°$, $45°$, $60°$ and $75°$ (from top to bottom).

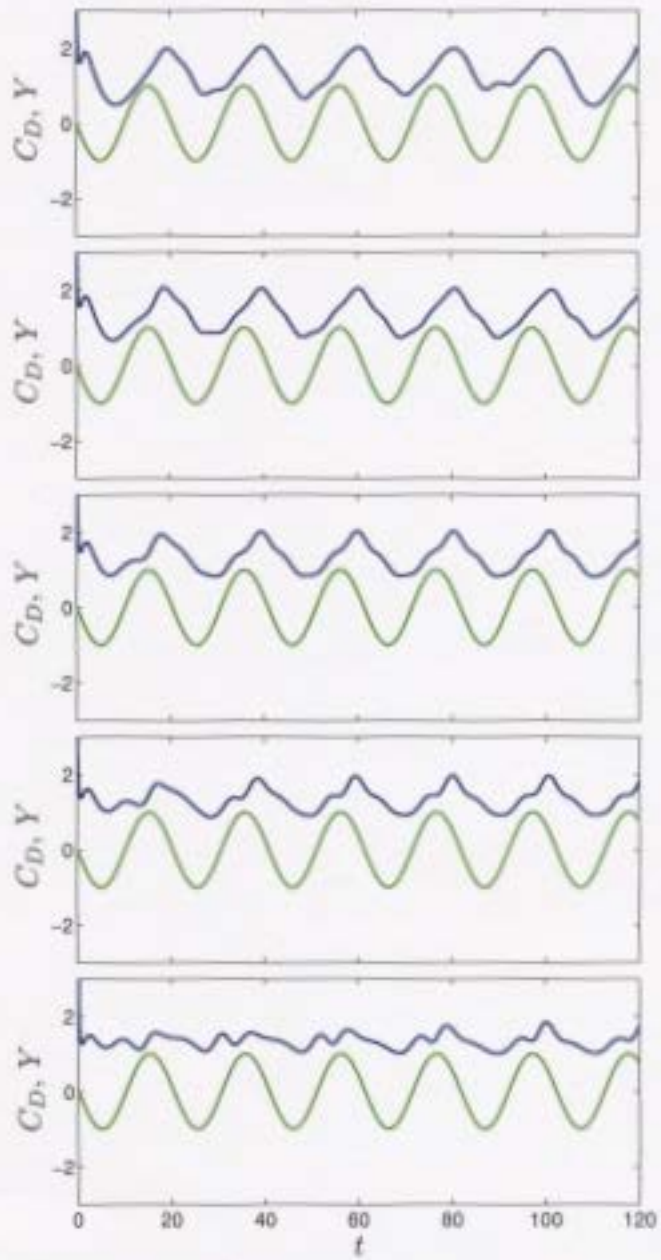

Figure 5.9: Drag coefficient (—) and cylinder displacement (—) for $R = 200$, $A = 1.0$, $S_f/S_0 = 0.5$ for angles of oscillation $\eta = 15°$, $30°$, $45°$, $60°$ and $75°$ (from top to bottom).

the lift in Figures 5.4, 5.6, and 5.8, the near wake is not in a locked-on state at $A = 0.2$, 0.6, or 1.0 when $S_f/S_0 = 0.5$. In all three of these figures, and at all angles $15° \leq \eta \leq 75°$ of oscillation, the dominant frequency in the spectrum is at $S_w/S_f = 2.0$ which yields $S_w = 2.0S_f = S_0$. That is, the dominant frequency in the near wake is the natural shedding frequency, S_0. However, by comparing each of figures 5.4, 5.6, and 5.8, we observe that the effect of the forcing frequency distinguished by the growing peak at $S_w/S_f = 1.0$ is increasing with an increase of the oscillation amplitude. However, the peak at the forcing frequency is not large enough yet to control the development of the hydrodynamic characteristics.

5.2 Effect of the angle of oscillation and amplitude of oscillation on vortex modes and force coefficients at $R = 200$ and $S_f/S_0 = 1.0$

As the frequency increases to $S_f/S_0 = 1.0$, the near wake features are no longer resulting from the natural shedding frequency. The instability in the wake created by the oscillation of the cylinder results in more interesting and developed flow features. Consequently, we investigate the effect of the oblique oscillation of a cylinder on the flow field characteristics for the case of $R = 200$, $S_f/S_0 = 1.0$, and $15° \leq \eta \leq 75°$ in much more detail. In addition, in each successive subsection the amplitude of oscillation is increased from $A = 0.2$ to 0.6 and then from $A = 0.6$ to 1.0. In this manner the effect of the increasing amplitude is also addressed to some extent.

5.2.1 Vortex modes at $A = 0.2$: $15° \leq \eta \leq 75°$

Previous work by Kocabiyik, Mahfouz, and Al-Mdallal (2004) has been completed for $R = 855$, $A = 0.26$, $0.5 \leq S_f/S_0 \leq 4.0$, and $15° \leq \eta \leq 75°$. This range of parameters is close to that which we choose here but our intent is simply to use the results of low amplitude inclined oscillations of a circular cylinder as a basis for comparison at

higher amplitudes.

To see the effect of the angle of oscillation we choose several interesting cases to exhibit key changes in the flow field. Firstly, the angle of oscillation drastically changes the timing of vortex shedding. Consider for instance the vorticity contours for $\eta = 15°, 30°$, 45°, 60°, and 75° when $A = 0.2$, $S_f/S_0 = 1.0$ given in Figure 5.10 . The snapshots correspond to half a period of cylinder oscillation when the cylinder is moving upward from its maximum negative displacement (position C) to maximum positive displacement (position G). From left to right at the top of this figure we observe a successive lengthening of the vortex formation length with an increase of the angle on both the top and bottom of the cylinder. These lengths, calculated at the moment when the cylinder is moving downward from its positive to negative displacement passing through the origin at position A, are recorded in Table 5.1. Notice

	Formation Length
η \ S_f/S_0	1.0
15°	2.59
30°	3.58
45°	4.21
60°	4.63
75°	4.89

Table 5.1: Horizontal location of vortex behind cylinder for $R = 200$, $A = 0.2$, $S_f/S_0 = 1.0$ when cylinder is at the origin moving downward.

that the vortex formation length increases with the increase of the angle. However, for the present case ($A = 0.2$, $S_f/S_0 = 1.0$), it is the result of this increase that is more interesting. During the upward movement of the cylinder, we observe for the smallest angle of $\eta = 15°$ that a single vortex is completely shed from the bottom of the cylinder, whereas, at the largest angle of $\eta = 75°$ the vortex is completely shed from the top of the cylinder. A timeline representing the approximate location of the cylinder when each vortex was shed during a single oscillation period is given

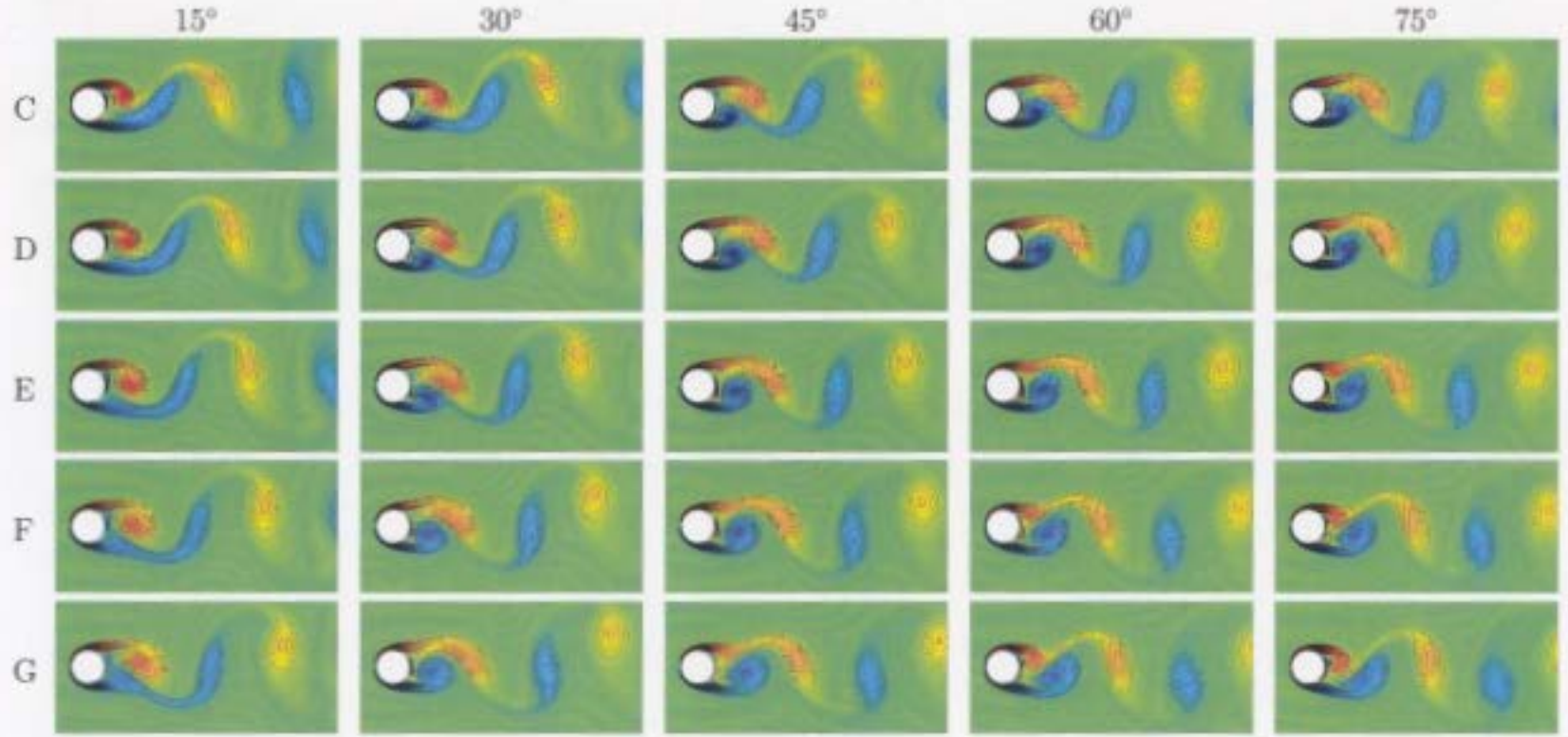

Figure 5.10: Vorticity contours for $R = 200$, $S_f/S_0 = 1.0$, $A = 0.2$ with $\eta = 15°$, $30°$, $45°$, $60°$, and $75°$ over half a period of cylinder oscillation from the minimum (position C) to maximum (position G) displacement of the cylinder [$T = 10.24$, $84.48 \leq t \leq 94.72$].

in Figure 5.11. The blue circles give the location of the cylinder when a vortex was shed from the bottom and the green circles indicate the location when a vortex was shed from the top. Note that the location of the blue and green circles are nearly reversed when $\eta = 15°$ and $\eta = 75°$, indicating that the time of shedding of vortices is completely reversed. For these extreme angles, bottom vortices are shed when the cylinder is moving downward and top vortices are shed when the cylinder is moving upward. In contrast, for the three other intermediate angles ($\eta = 30°$, $45°$, $60°$), the bottom vortex sheds during the upward movement of the cylinder from $r = -A$ to $r = A$ and from $r = -A$ to $r = A$ the top vortex is shed. Thus, the location and timing during one period, T, of the cylinder oscillation where each vortex is shed is severely altered as we increase the angle of oscillation. This phenomenon was also

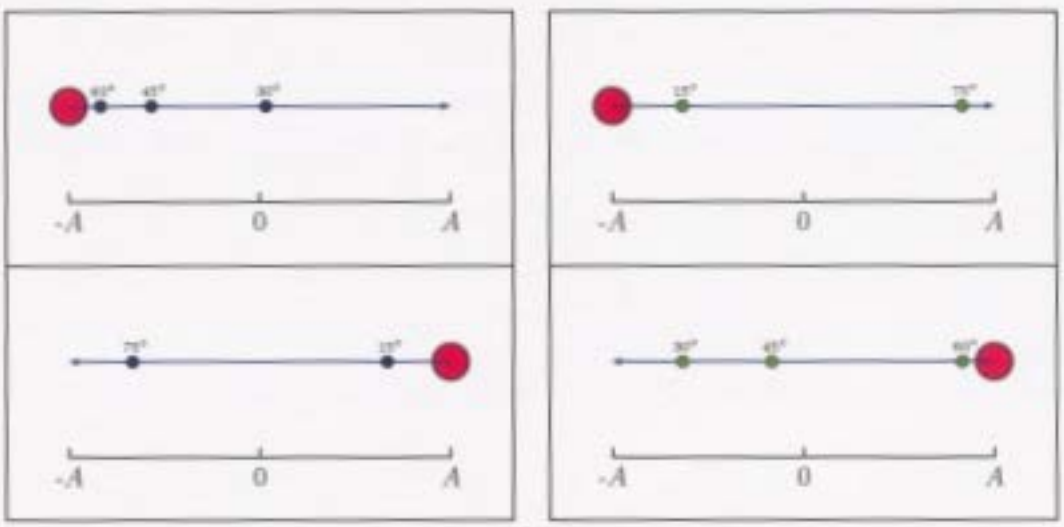

Figure 5.11: The location of the cylinder when each the vortices are shed from the bottom (right) and top (left) during one period of cylinder oscillation for $R = 200$, $A = 0.2$, $S_f/S_0 = 1.0$.

observed but not discussed at $S_f/S_0 = 0.5$ for $A = 0.2, 0.6$, and 1.0.

The 2S mode of vortex shedding persists in the near wake with a cycle equal to one period, T, of cylinder oscillation for $\eta = 15°$, $30°$, $45°$, $60°$, and $75°$. Thus, at this amplitude and frequency, the mode of vortex shedding is not altered by the varying

angle.

5.2.2 Force coefficients at $A = 0.2$: $15° \leq \eta \leq 75°$

The drag and lift coefficients for this case are presented in Figures 5.12-5.13 along with the power spectra of the lift coefficient. It is evident that both coefficients have a period which is equal to that of the cylinder oscillation period, T, but the power spectra of the lift coefficient in Figure 5.12 suggests that the vortex shedding is not locked onto the cylinder oscillation frequency in all cases. At $\eta = 15°$, we observe that the peak at $S_w/S_f = 1.0$ in the spectrum is actually a combination of two peaks, corresponding to the natural and forcing frequencies. For all other angles, $\eta = 30°$, 45°, 60°, and 75° there is a single peak in the power spectra which suggests that fundamental lock-on does occur at $S_f/S_0 = 1.0$ for $\eta \geq 30°$. Previous results by Ongoren and Rockwell (1988b), as mentioned earlier, stated that the near wake was not locked-on for oscillations performed at $\eta = 0°$ while for the transverse case, ($\eta = 90°$), fundamental lock-on was observed. The results discussed here indicate that even for small angles of oscillation, $\eta \leq 15°$, lock-on is not achieved near $S_f/S_0 = 1.0$ when $A = 0.2$. Then, for $\eta \geq 30°$, which is not a strict bound, the fundamental lock-on regime exists up until the extensively studied case of transverse oscillations of a circular cylinder.

Using the force coefficients in Figures 5.12-5.13 we also calculate various quantitative results such as the average drag, $\bar{C}_D$, the maximum lift, $C_{L,\max}$, and the amplitude of the drag and lift coefficients, $AMP(C_D)$ and $AMP(C_L)$, which are recorded in Table 5.2. With the exception of the first column for $\eta = 15°$, the results are in general consistent with one another. The $\eta = 15°$ column is an exception because of the fact that lock-on is not observed at this angle which, consequently, causes the results to vary depending on the period. Nonetheless, the effect of increasing the angle of oscillation is to increase the average drag but decrease the amplitude of the drag coefficient. Further, we observe an increase of the maximum lift, $C_{L,\max}$, and

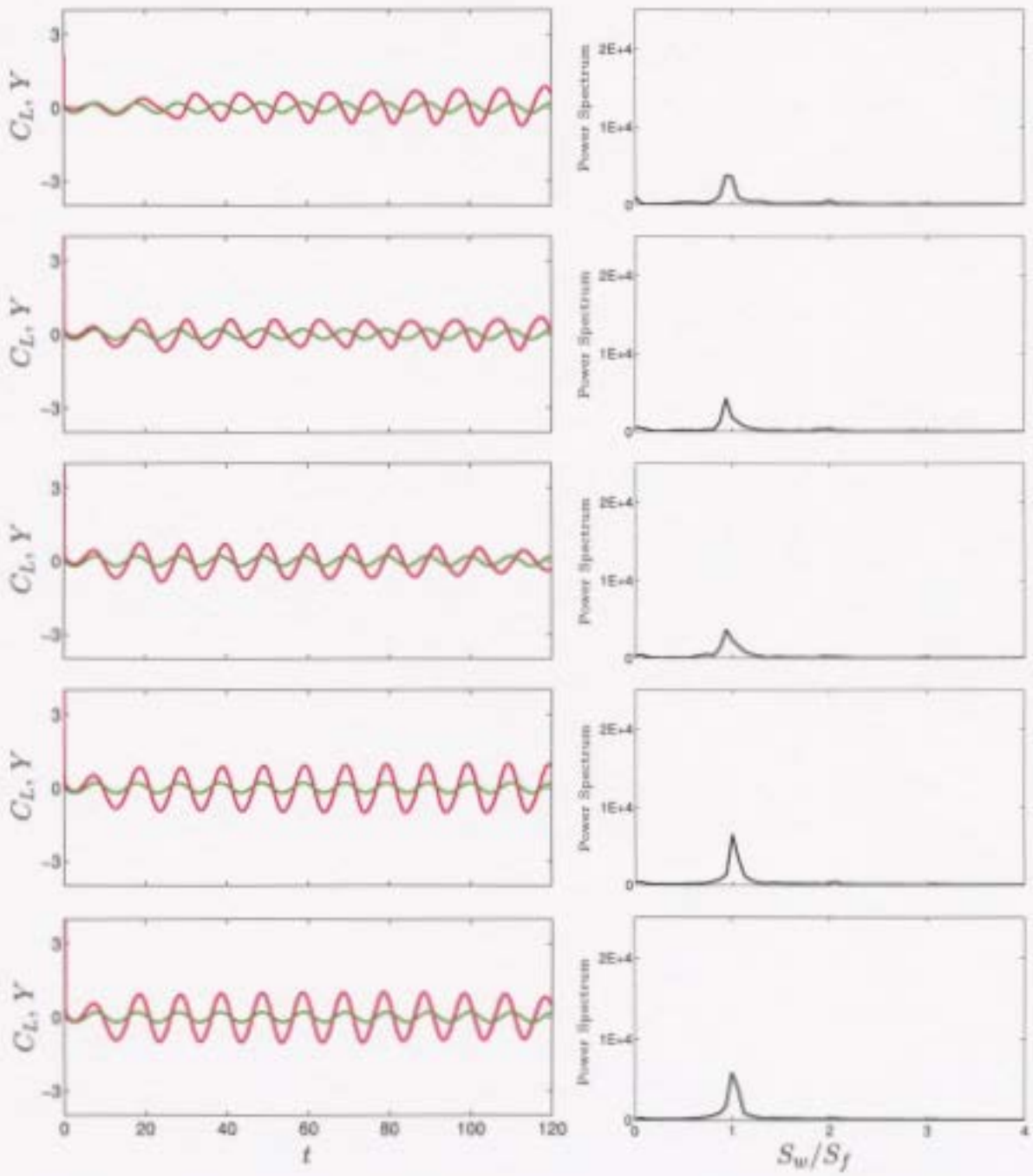

Figure 5.12: Lift coefficient (—) and cylinder displacement (—) with power spectrum of lift coefficient (right) for $R = 200$, $A = 0.2$, $S_f/S_0 = 1.0$ for angles of oscillation $\eta = 15°$, $30°$, $45°$, $60°$ and $75°$ (from top to bottom).

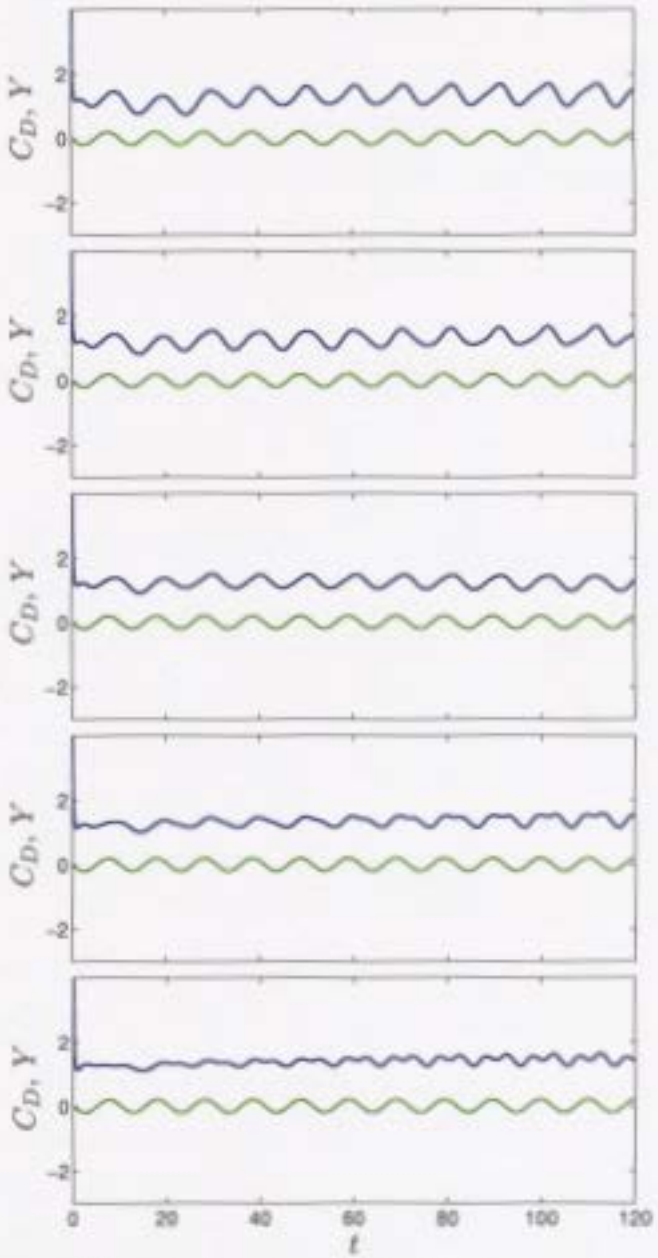

Figure 5.13: Drag coefficient (—) and cylinder displacement (—) for $R = 200$, $A = 0.2$, $S_f/S_0 = 1.0$ for angles of oscillation $\eta = 15°$, $30°$, $45°$, $60°$ and $75°$ (from top to bottom).

η	15°	30°	45°	60°	75°
$\bar{C}_D$	1.34	1.26	1.24	1.38	1.44
$C_{L,\max}$	0.68	0.54	0.61	0.98	1.01
$AMP(C_D)$	0.65	0.54	0.44	0.38	0.34
$AMP(C_L)$	1.36	1.13	1.25	1.98	1.97

Table 5.2: Average drag $\bar{C}_D$, maximum lift, and amplitude $AMP(\cdot)$ of drag and lift coefficients for $R = 200$, $A = 0.2$, $S_f/S_0 = 1.0$ when $15° \leq \eta \leq 75°$.

amplitude of the lift coefficient at $S_f/S_0 = 1.0$, $A = 0.2$ for $\eta \geq 30°$. These changes are justified since the increased upward movement, $Y(t)\sin(\eta)$, of the cylinder results in larger stress and pressure forces on the surface of the cylinder in the transverse direction and smaller contributions to the inline drag force.

5.2.3 Vortex modes at $A = 0.6$: $15° \leq \eta \leq 75°$

In Figure 5.14 we present the vorticity contours for the increased amplitude of $A = 0.6$. Note that the 2S mode of vortex shedding still dominates the near wake at $\eta = 15°$, 30°, 45°, 60°, and 75°, but the clearly defined shedding of each vortex is not as evident as it is for $A = 0.2$. For $\eta \geq 45°$, it is clear that one distinct vortex is shed from the top and one is shed from the bottom. However, for the smaller angles of $\eta = 15°$ and 30°, the now three times larger oscillation amplitude creates a natural transition to a symmetric-like mode. Obviously, the near wake is not symmetric, but this is the first step in a transition to symmetry. To support this claim, observe that for $\eta = 15°$ the vortices form/grow on top and bottom of the cylinder almost simultaneously. As in the previous section, the approximate location of the cylinder when the vortices are shed from the top and bottom of the cylinder are given in Figure 5.15. Notice that the vortices shedding from the top and bottom do not shed at opposite times in the shedding cycle as was the case for $A = 0.2$. However, the time between the shedding of the vortices from the top and bottom of the cylinder has decreased dramatically for $\eta < 45°$. Approximately half a period had separated the shedding of vortices from top and bottom for $\eta = 15°$ and $A = 0.2$ whereas for $A = 0.6$ the two counter-rotating

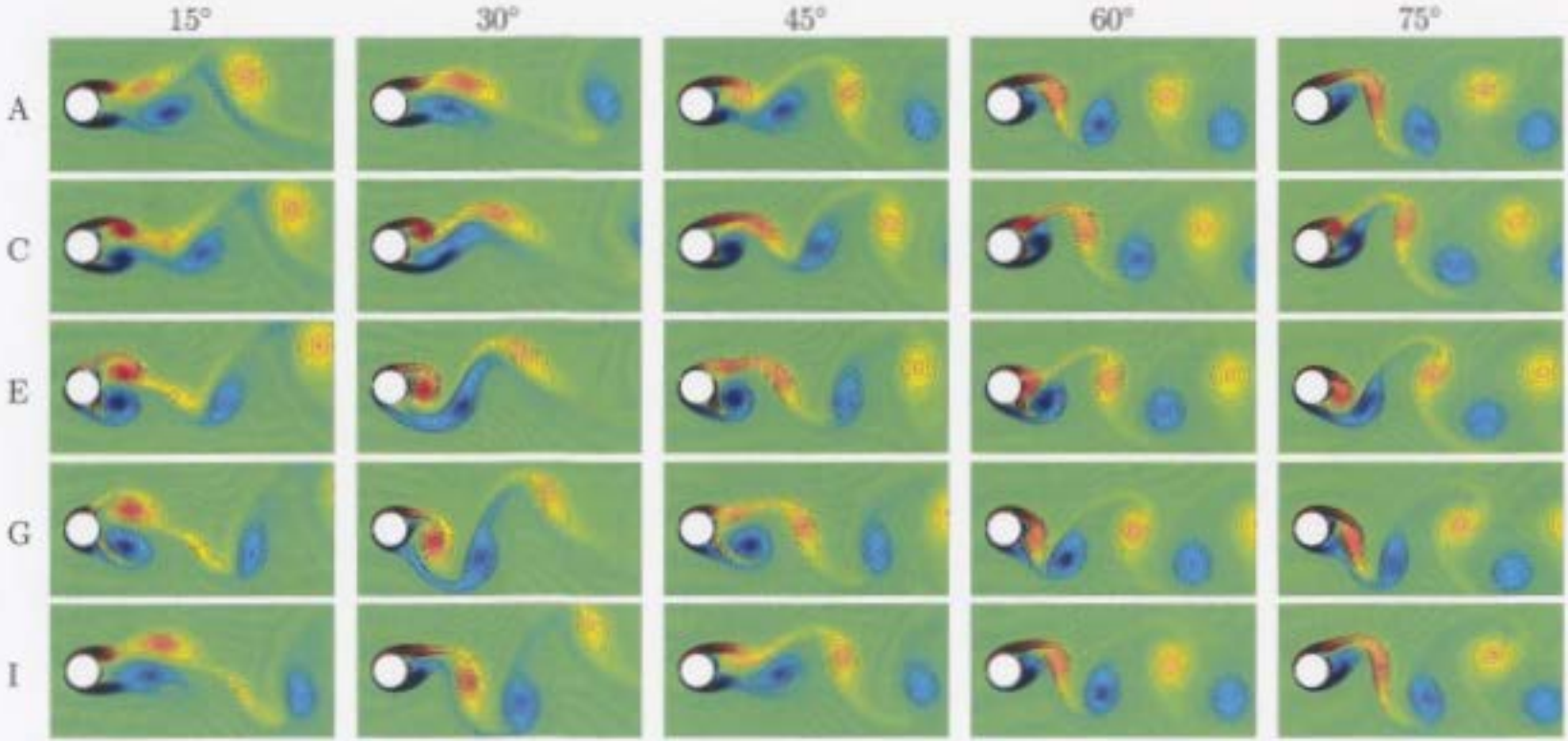

Figure 5.14: Vorticity contours for $R = 200$, $S_f/S_0 = 1.0$, $A = 0.6$ with $\eta = 15°$, $30°$, $45°$, $60°$, and $75°$ over one period of cylinder oscillation [$T = 10.24$, $81.92 \leq t \leq 92.16$].

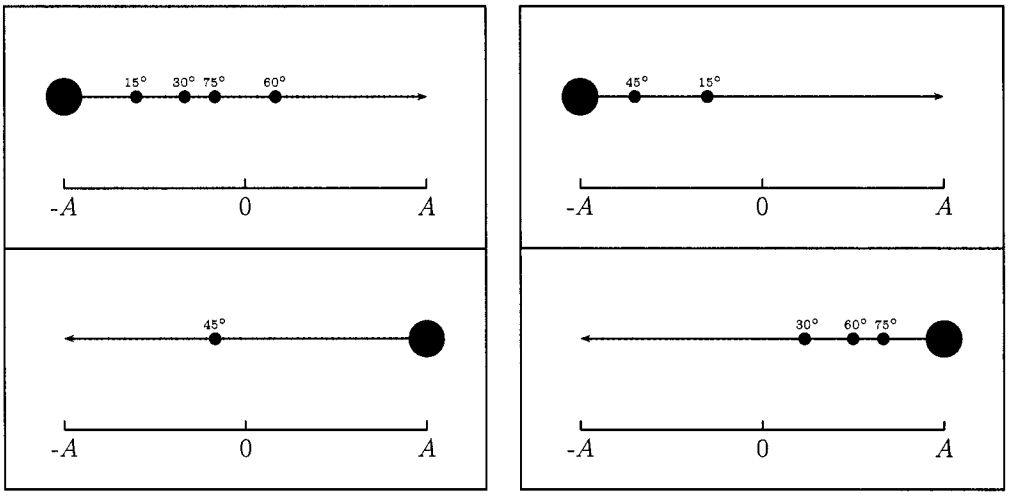

Figure 5.15: The location of the cylinder when each the vortices are shed from the bottom (right) and top (left) during one period of cylinder oscillation for $R = 200$, $A = 0.6$, $S_f/S_0 = 1.0$.

vortices are shed very close together.

5.2.4 Force coefficients at $A = 0.6$: $15° \leq \eta \leq 75°$

The highly competitive nature of the flow due to a transition to symmetry is also quite evident in the lift and drag coefficients with corresponding lift spectra shown in Figures 5.16-5.17. For $\eta < 45°$, the competition between the symmetric-asymmetric modes is suggested by the aperiodic nature of the lift coefficient and corresponding spectra in Figure 5.16. For $\eta = 15°$ and $30°$, as suggested by the two irregularly positioned peaks in the spectra, the vortex shedding frequency has not locked-on to the cylinder oscillation frequency. This phenomenon is again explained by the increased symmetrical component of the forced cylinder displacement.

However, as the angle of oscillation increases above $\eta = 45°$, at $A = 0.6$, the lift and drag curves become periodic over one period, T, of cylinder oscillation and thus is in a locked-on state. It is now evident that both the angle and amplitude of oscillation are extremely important in determining the near wake flow properties. We

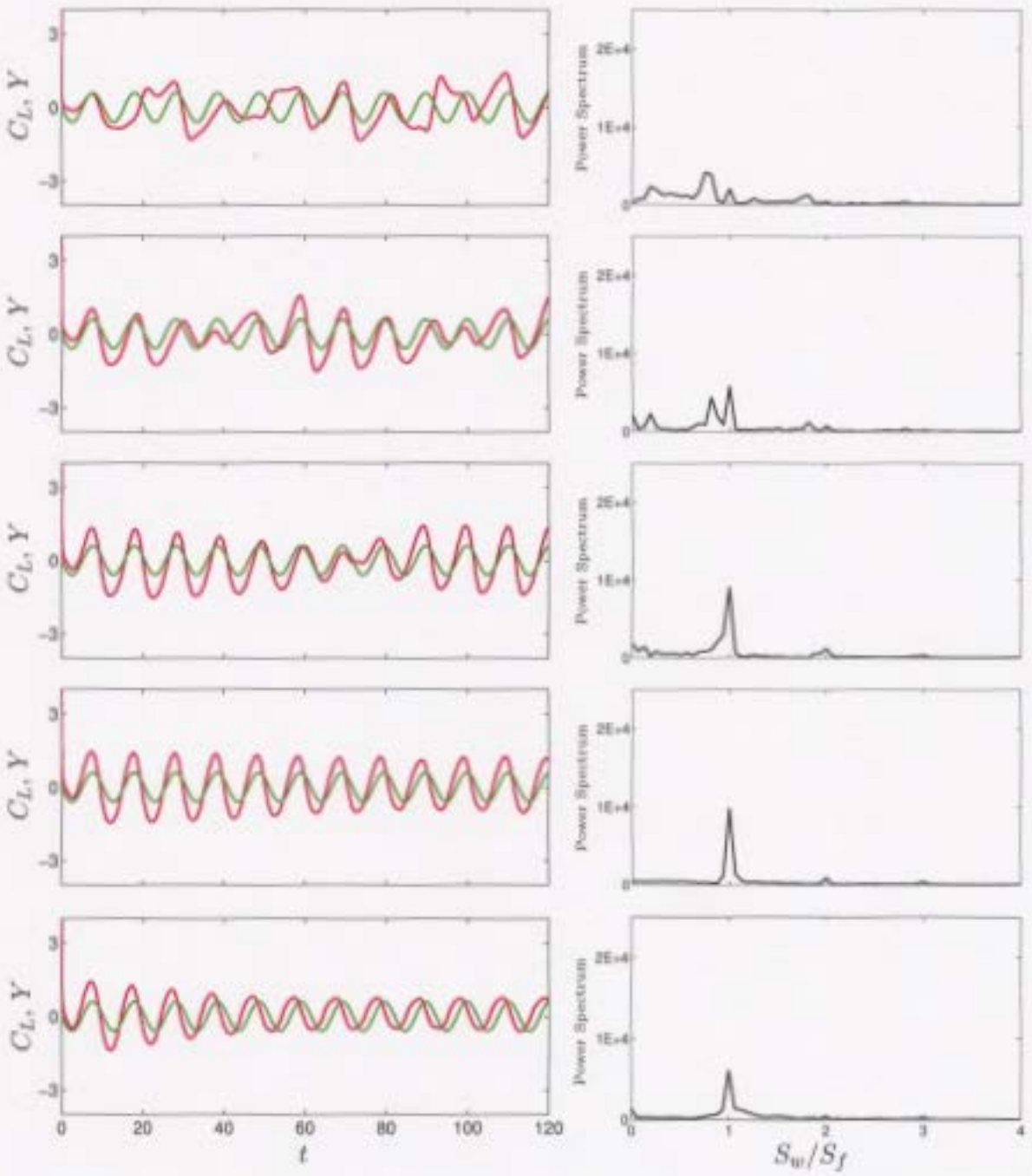

Figure 5.16: Lift coefficient (—) and cylinder displacement (—) with power spectrum of lift coefficient (right) for $R = 200$, $A = 0.6$, $S_f/S_0 = 1.0$ for angles of oscillation $\eta = 15°$, $30°$, $45°$, $60°$ and $75°$ (from top to bottom).

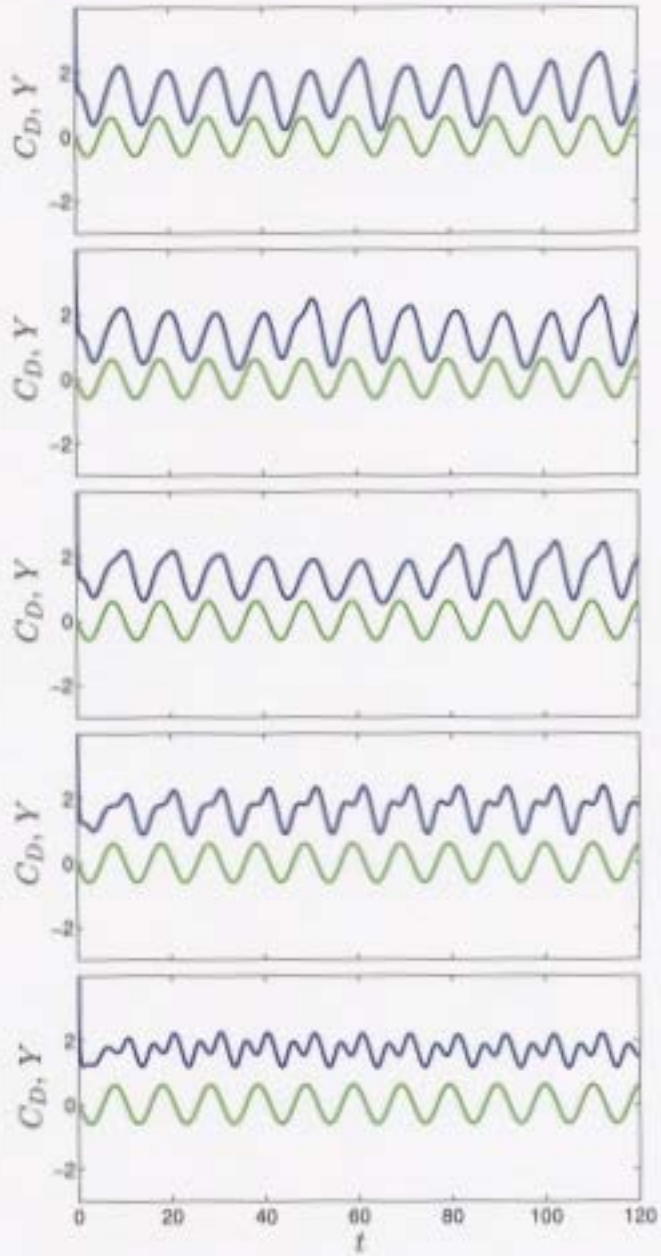

Figure 5.17: Drag coefficient (—) and cylinder displacement (—) for $R = 200$, $A = 0.6$, $S_f/S_0 = 1.0$ for angles of oscillation $\eta = 15°$, $30°$, $45°$, $60°$ and $75°$ (from top to bottom).

calculate the important flow quantities ($\bar{C}_D$, $C_{L,\max}$, $AMP(C_D)$, $AMP(C_L)$ as before and record these values in Table 5.3. Neglecting the first two columns it is evident

η	15°	30°	45°	60°	75°
$\bar{C}_D$	1.29	1.31	1.32	1.71	1.69
$C_{L,\max}$	0.72	0.56	1.44	1.13	0.73
$AMP(C_D)$	1.94	1.49	1.85	1.42	1.00
$AMP(C_L)$	1.66	1.72	2.30	2.04	1.20

Table 5.3: Average drag $\bar{C}_D$, maximum lift, and amplitude $AMP(\cdot)$ of drag and lift coefficients for $R = 200$, $A = 0.6$, $S_f/S_0 = 1.0$ when $15° \leq \eta \leq 75°$.

that we do not have the same behavior as in the case for $A = 0.2$. In fact, for $A = 0.6$ the amplitude of the lift $AMP(C_L)$ and the maximum value of the lift coefficient, $C_{L,\max}$, actually decreases in contrast to its behavior at lower amplitudes. The average drag coefficient $\bar{C}_D$ increases, in general, and the amplitude of the drag coefficient decreases which is consistent with the results for $A = 0.2$, $S_f/S_0 = 1.0$. The results for $\eta = 15°$ and 30° are not consistent with these general remarks for all quantities since the flow is not locked-on at these angles.

5.2.5 Vortex modes at $A = 1.0$: $15° \leq \eta \leq 75°$

The vorticity contours for the largest amplitude under consideration, $A = 1.0$, are given in Figure 5.18 for $15° \leq \eta \leq 75°$. In this figure our initial observation about a transition to a symmetric-like wake is confirmed. At this increased amplitude, the vortex shedding modes are recorded in Table 5.4 and the location of the cylinder at which each vortex is shed is recorded in Figure 5.19. The notation 2S* is used to indicate that the two vortices are shed at nearly the same instant. The vortices in this case may not be the same strength or size as is the case for a symmetric vortex shedding mode, but they are shed almost simultaneously. In fact, Figure 5.19 shows that a little more than a quarter of one period separates the shedding of the top and bottom vortices for all angles of oscillation with the largest difference being at $\eta = 75°$. For an angle of $\eta = 0°$, this increased amplitude would result in a symmetric

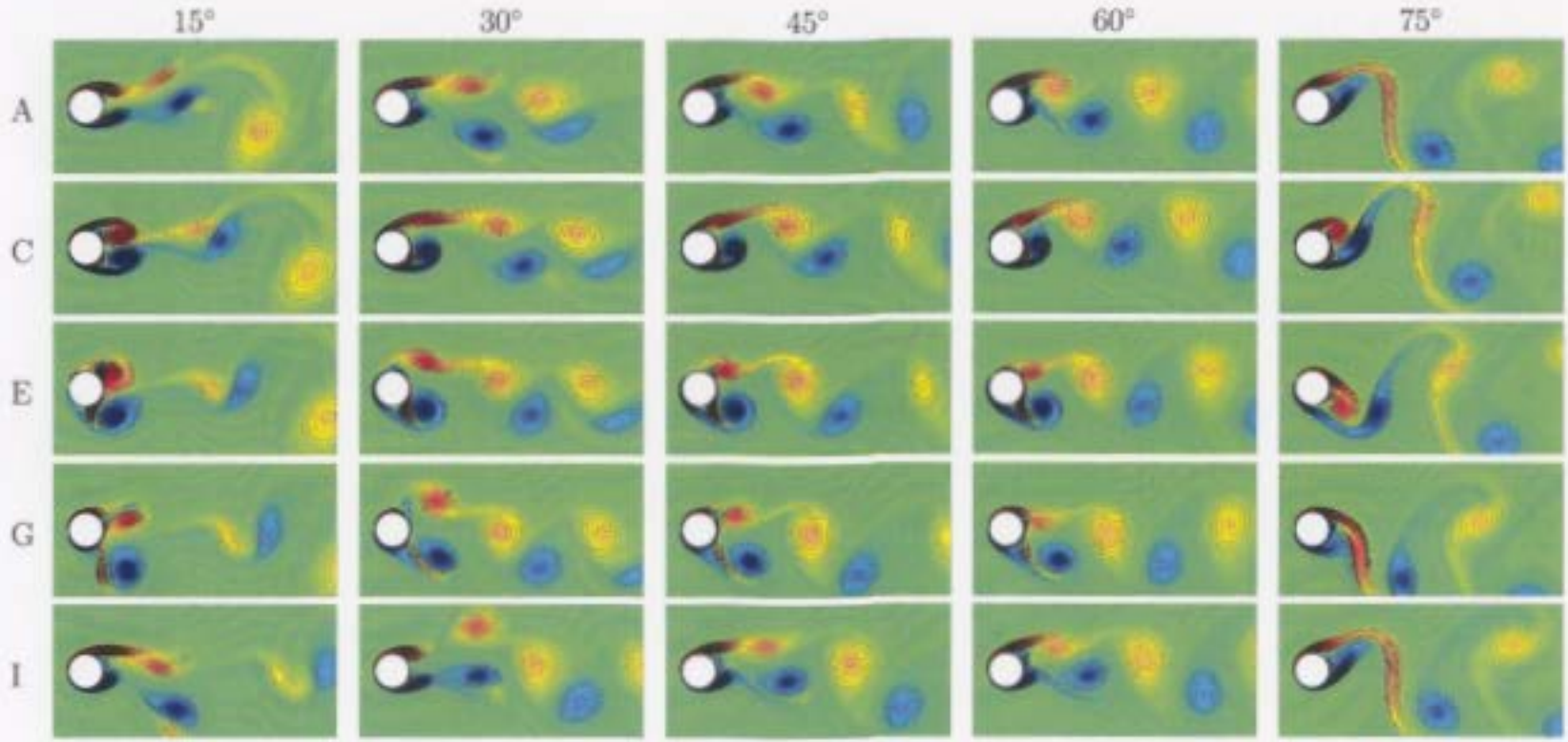

Figure 5.18: Vorticity contours for $R = 200$, $S_f/S_0 = 1.0$, $A = 1.0$ with $\eta = 15°$, $30°$, $45°$, $60°$, and $75°$ over one period of cylinder oscillation [$T = 10.24$, $81.92 \leq t \leq 92.16$].

η \ A	1.0
15°	2S* [T]
30°	2S* [T]
45°	2S [T]
60°	2S [T]
75°	2S [T]

Table 5.4: Dominant modes and periods of vortex formation in the near wake for $R = 200$, $S_f/S_0 = 1.0$, $A = 0.2$, and $\eta = 15°, 30°, 45°, 60°, 75°$.

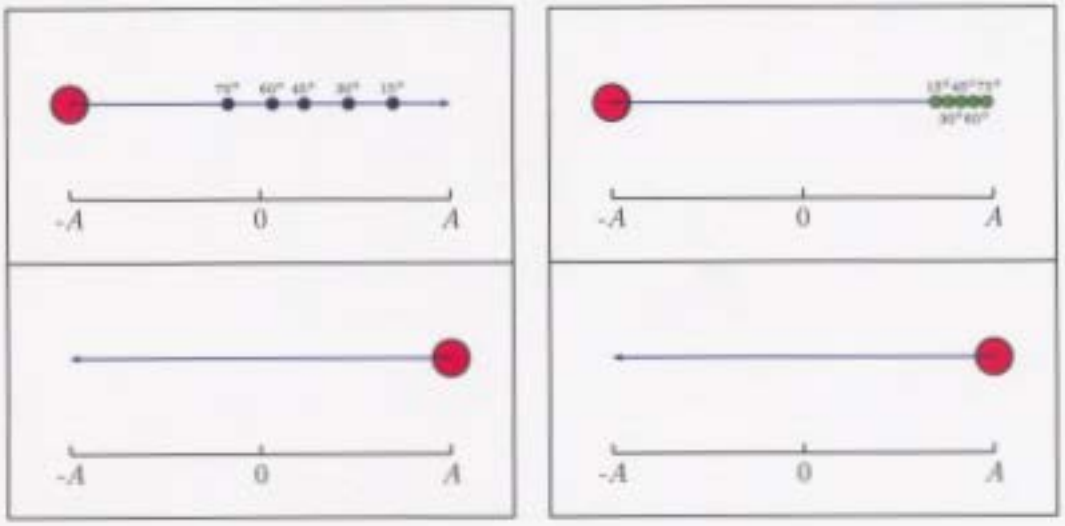

Figure 5.19: The location of the cylinder when each the vortices are shed from the bottom (right) and top (left) during one period of cylinder oscillation for $R = 200$, $A = 1.0$, $S_f/S_0 = 1.0$.

mode of vortex shedding and a completely symmetric wake. However, the asymmetry introduced by the angle of oscillation prevents any symmetric development of the near wake but produces what we refer to as the 2S* mode in which the time between the alternate shedding of vortices has decreased significantly.

5.2.6 Force coefficients at $A = 1.0$: $15° \leq \eta \leq 75°$

The lift and drag coefficients with corresponding lift spectra for $A = 1.0$ and $15° \leq \eta \leq 75°$ at $S_f/S_0 = 1.0$ are given in Figures 5.20-5.21. It is noted that for $\eta < 45°$ the lift is not a smooth periodic curve due to the occurrence of more than one dominant frequency in the near wake, as suggested by the spectra. For $\eta = 15°$ and 30° the results again indicate a non-lock-on regime. The smaller peaks in the spectra are suppressed significantly as we increase the angle to $\eta \geq 45°$ where the smooth periodic nature of the lift and drag coefficients has been reestablished.

The average drag, maximum lift, and amplitude of drag and lift coefficients are recorded in Table 5.5 Disregarding the first two columns, where the vortex shed-

η	15°	30°	45°	60°	75°
$\bar{C}_D$	1.84	1.84	1.47	1.48	1.92
$C_{L,\max}$	2.16	1.92	0.70	1.68	0.44
$AMP(C_D)$	3.53	3.47	3.07	2.18	1.68
$AMP(C_L)$	3.75	2.99	2.77	3.61	0.55

Table 5.5: Average drag $\bar{C}_D$, maximum lift, and amplitude $AMP(\cdot)$ of drag and lift coefficients for $R = 200$, $A = 1.0$, $S_f/S_0 = 1.0$ when $15° \leq \eta \leq 75°$.

ding frequency is not locked onto the cylinder oscillation frequency, we observe a very interesting phenomenon from these results. For $\eta \geq 45°$, the average drag increases while the amplitude of the drag coefficient decreases, as before. However, the maximum lift and amplitude of the lift coefficient increases for $\eta = 45°$ and 60°, but at $\eta = 75°$ these quantities are reduced significantly. To understand why this occurs we first direct our attention to the vorticity contours which were displayed in Figure

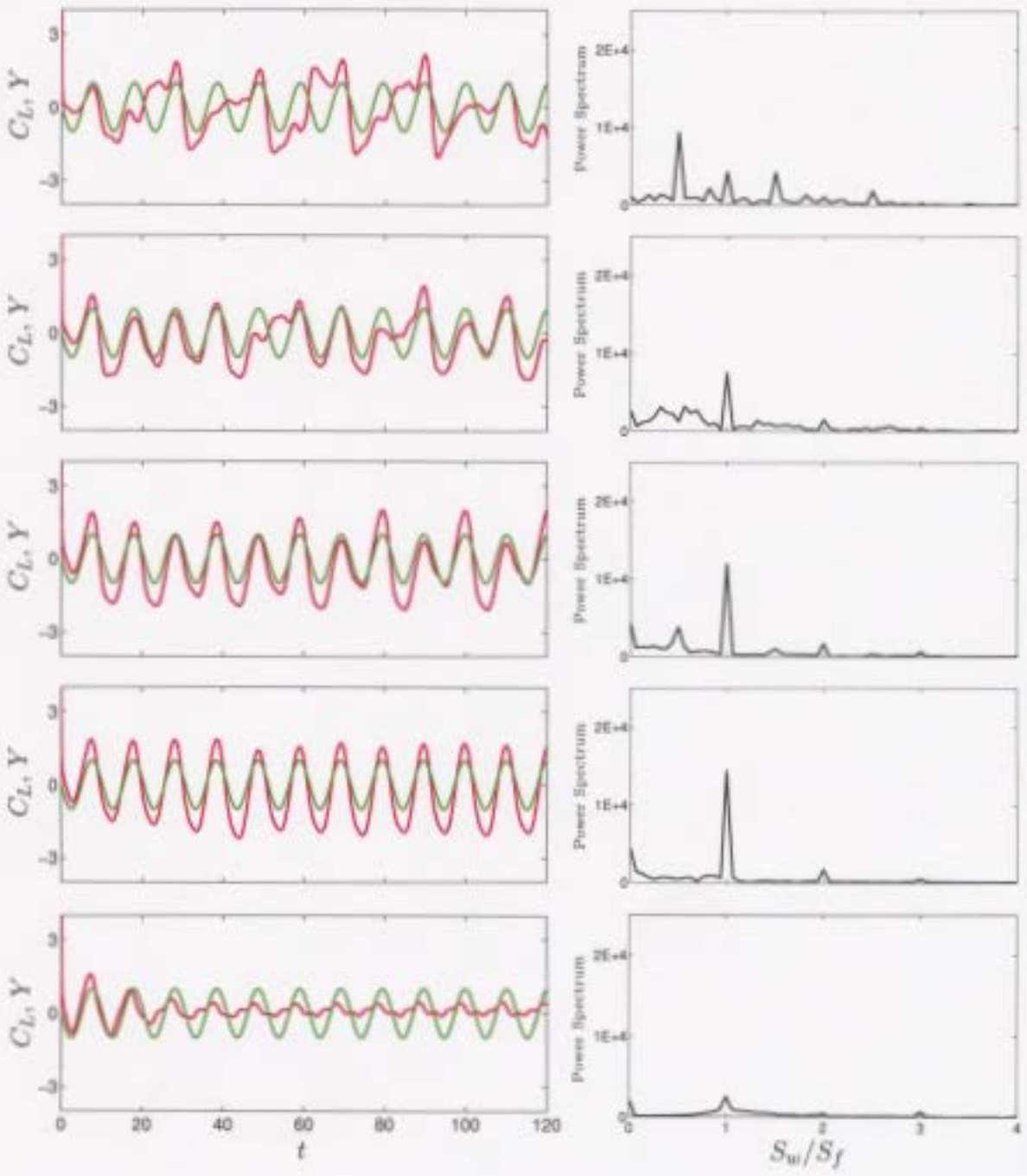

Figure 5.20: Lift coefficient (—) and cylinder displacement (—) with power spectrum of lift coefficient (right) for $R = 200$, $A = 1.0$, $S_f/S_0 = 1.0$ for angles of oscillation $\eta = 15°$, $30°$, $45°$, $60°$ and $75°$ (from top to bottom).

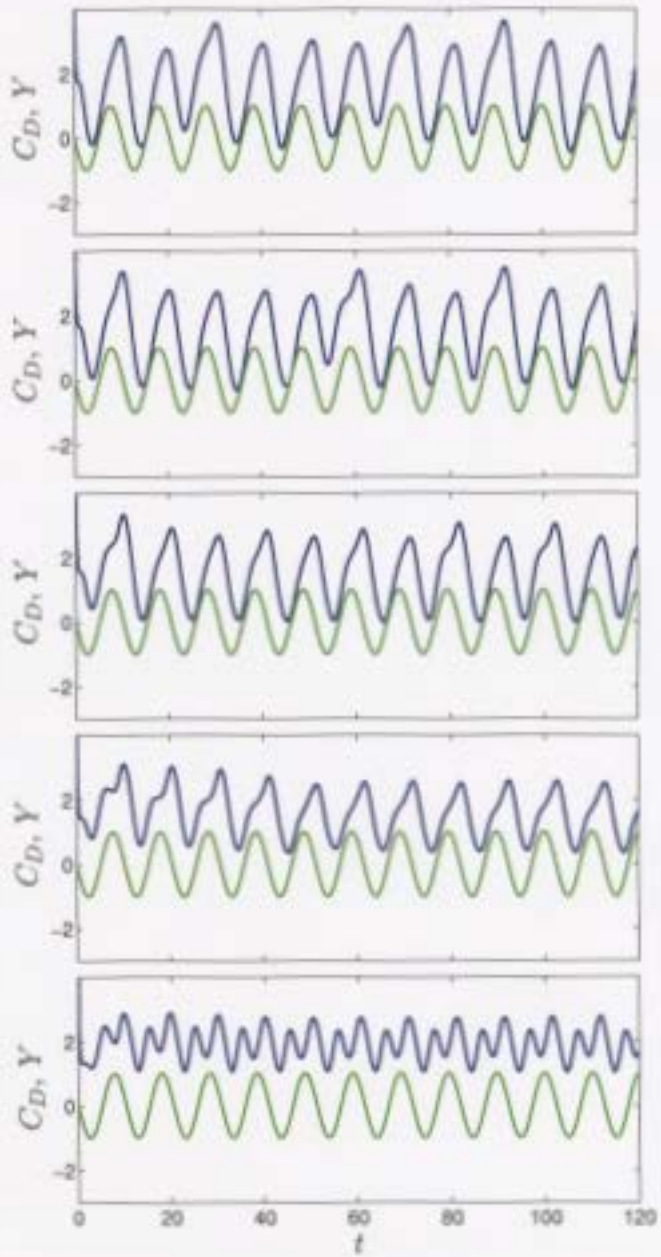

Figure 5.21: Drag coefficient (—) and cylinder displacement (—) for $R = 200$, $A = 1.0$, $S_f/S_0 = 1.0$ for angles of oscillation $\eta = 15°$, $30°$, $45°$, $60°$ and $75°$ (from top to bottom).

5.18. Let us fix our attention on the first row, position A, of vorticity contours and observe the effect of the increasing angle. At this large amplitude, $A = 1.0$, we do not see a lengthening of the vortex formation length as for the case when $A = 0.2$. Instead, the vortex on top of the cylinder seems to move closer to the cylinder surface as η is increased from $\eta = 45°$ to $60°$ while the vortex on bottom remains relatively fixed in size and location.

With the increase of the angle from $\eta = 60°$ to $75°$ the vertical movement of the cylinder over the oscillation period increases while the vortex formation length is decreasing. The result is an increased interaction between the top and bottom vortices which consequently effects the size of each developing vortex. Comparing the two figures at position A for $\eta = 60°$ and $\eta = 75°$ we observe that the area of major concentration of vorticity has switched from the top to the bottom of the cylinder. This phenomenon is referred to as switching and is usually discussed in the context of increasing the forcing frequency through the fundamental lock-on range [see Guilmineau and Queutey (2002)] in which the area of major concentration of vorticity switches from one side of the cylinder to the other. In our analysis we observe a switching of the major concentration of vorticity as we increase the angle of oscillation. In addition, instead of reducing to zero as the in case for transverse oscillations, the top vortex for which we observed a decreasing formation length with increasing angle has been pushed away from the cylinder surface. In this context, the switching is different than it is for the case of a transversely oscillating cylinder. The combination of the increasing angle and faster generation of vorticity on the bottom of the cylinder both combine in this case to cause the phenomenon for increasing angles of oscillation. We are not certain at which angle the switch occurs, but it is somewhere between $\eta = 60°$ and $\eta = 75°$.

To determine the effect of the switching on the force coefficients we present the friction and pressure components of the lift coefficient for $\eta = 60°$ and $\eta = 75°$ at $A = 1.0$,

$S_f/S_0 = 1.0$ in Figure 5.22. These curves indicates that this switching phenomenon

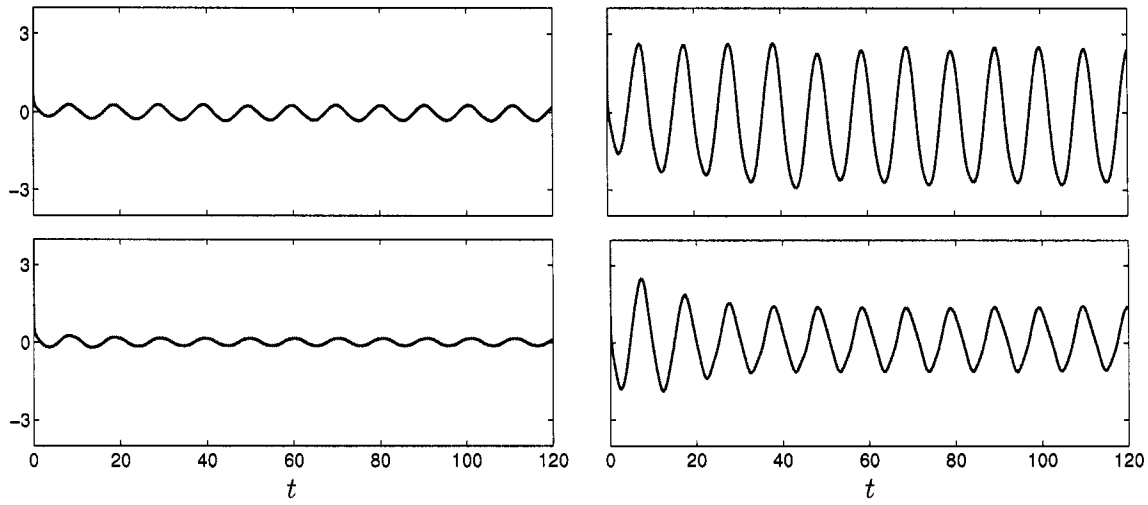

Figure 5.22: Friction (left) and pressure (right) contributions to the lift coefficient for $\eta = 60°$ (top) and $\eta = 75°$ (bottom) when $R = 200$, $A = 1.0$, $S_f/S_0 = 1.0$.

causes a large decrease in the amplitude of the pressure contribution to the lift coefficient. This large decrease is reflected in the results of Table 5.5.

In addition to the amplitude decrease, another effect of the switching is the phase difference that is observed in the lift curve for $\eta = 75°$, as compared to other angles, in Figure 5.20. Notice that neither the friction or the pressure contributions in Figure 5.22 are aperiodic waveforms for $\eta = 75°$. In fact, the period does not look to be that much different than it is for $\eta = 60°$. Moreover, the third term which contributes to the lift (due to non-intertial reference frame) is simply a trigonometric sine function. For $\eta = 60°$, the lift curve is a period sinusoidal curve. However, the switching of the major concentration of vorticity creates a phase difference between the terms contributing to the lift curve, resulting in the aperiodic waveform observed in Figure 5.20 for $\eta = 75°$.

5.3 Effect of the angle and amplitude of oscillation on vortex modes and force coefficients when $R = 200$ and $S_f/S_0 = 2.0$

As we increase the forcing frequency to $S_f/S_0 = 2.0$ the timing alteration effect of the oscillation angle is eliminated. For example, at $S_f/S_0 = 2.0$, $A = 0.2$, the vorticity contours over two periods, $2T$, of cylinder oscillation from position A to Q are shown in Figure 5.23. For each of the angles in this figure we see that a single vortex is shed from the bottom of the cylinder over the first of the two oscillation periods. Hence the angle of oscillation has a large influence on the timing of vortex shedding only at the smaller frequencies of $S_f/S_0 = 0.5$ and 1.0.

The lift (with corresponding spectra) and drag coefficients are shown in Figures 5.24-5.25 for $A = 0.2$. Several clearly defined peaks in the spectra of the lift coefficient at $S_w/S_f = 1.0$ and 0.5 are reminiscent of the peaks which we encountered in Chapter 4 corresponding to the forcing and natural shedding frequencies, respectively. Thus, at $S_f/S_0 = 2.0$, the 2-superharmonic lock-on is observed at all angles of oscillation. This statement is confirmed by considering again the vorticity contours in Figure 5.23 which show a periodic locked-on wake over two periods, $2T$, of cylinder oscillation. At $\eta = 15°$, the peak corresponding to the forcing frequency at $S_w/S_f = 1.0$ is smaller than the peak at $S_w/S_f = 0.5$ corresponding to the natural shedding frequency, but the vorticity contours indicate that the wake is locked-on. In Table 5.6 we observe

η	15°	30°	45°	60°	75°
$\bar{C}_D$	1.48	1.52	1.49	1.45	1.40
$C_{L,\max}$	1.46	1.70	1.85	1.94	1.96
$AMP(C_D)$	2.14	1.88	1.58	1.19	0.74
$AMP(C_L)$	2.33	3.03	3.35	3.55	3.57

Table 5.6: Average drag $\bar{C}_D$, maximum lift, and amplitude $AMP(\cdot)$ of drag and lift coefficients for $R = 200$, $A = 0.2$, $S_f/S_0 = 2.0$ when $15° \leq \eta \leq 75°$.

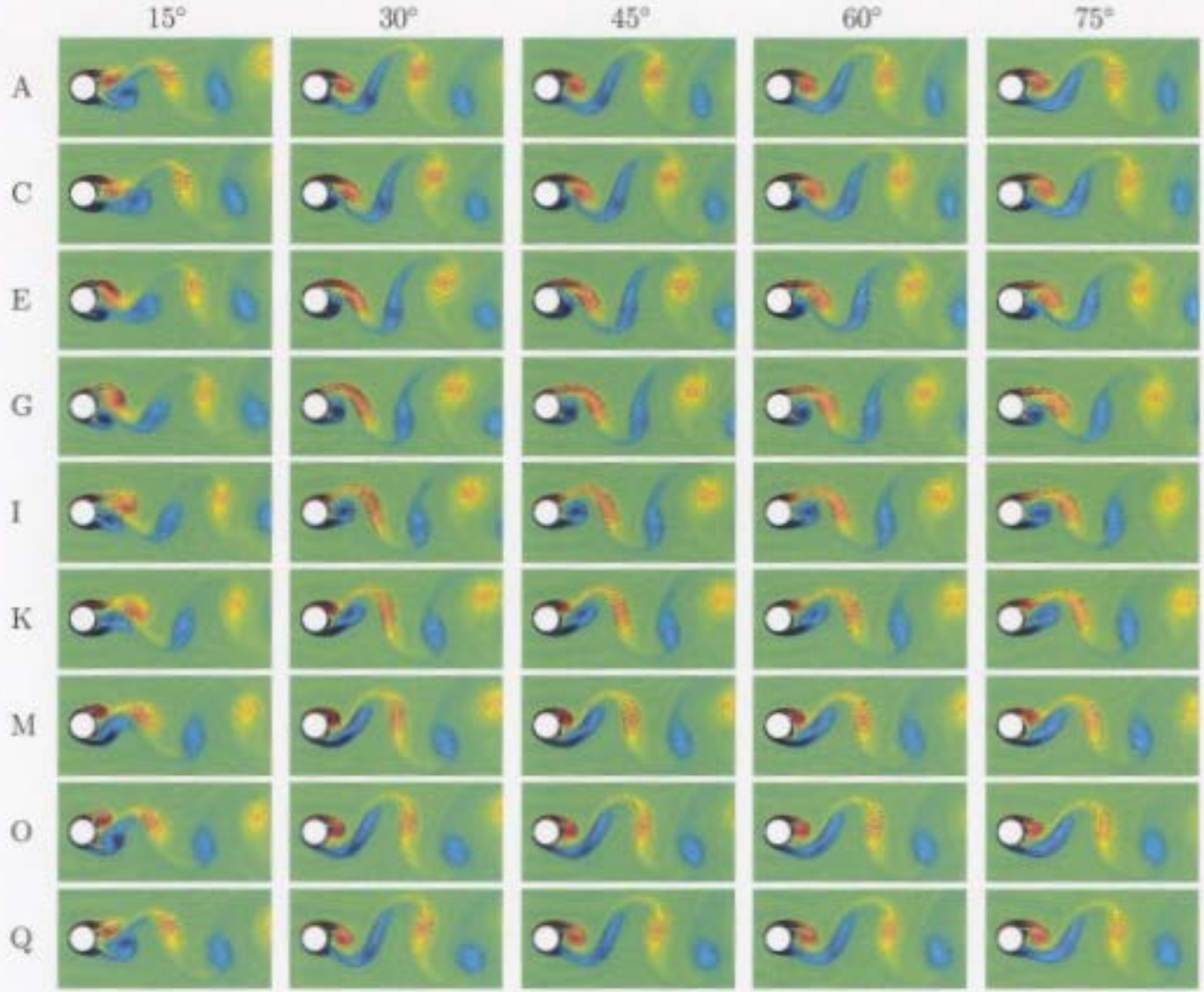

Figure 5.23: Vorticity contours for $R = 200$, $S_f/S_0 = 2.0$, $A = 0.2$ with $\eta = 15°$, $30°$, $45°$, $60°$, and $75°$ over one period of cylinder oscillation [$T = 5.12$, $81.88 \leq t \leq 92.12$].

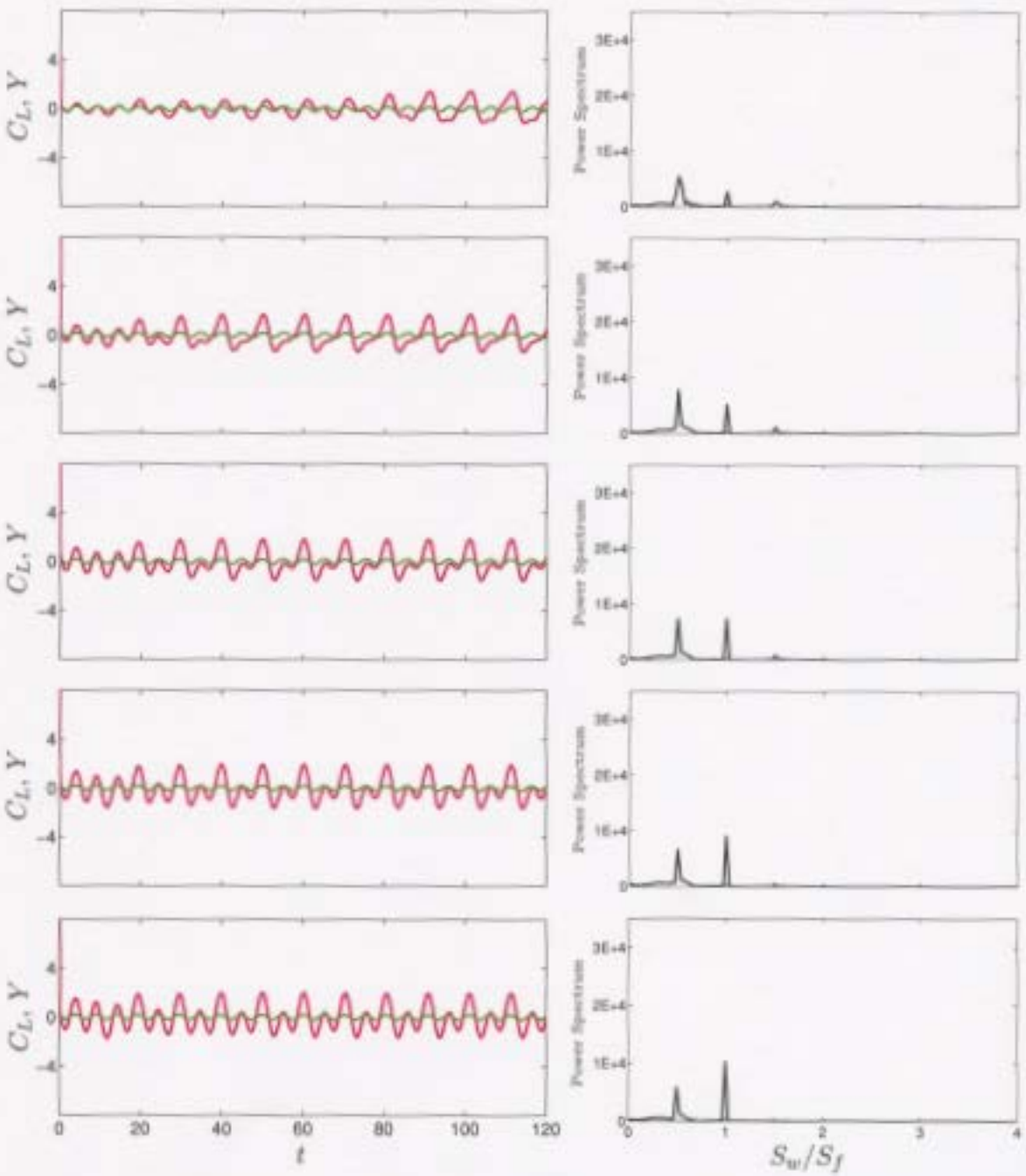

Figure 5.24: Lift coefficient (—) and cylinder displacement (—) with power spectrum of lift coefficient (right) for $R = 200$, $A = 0.2$, $S_f/S_0 = 2.0$ for angles of oscillation $\eta = 15°$, $30°$, $45°$, $60°$ and $75°$ (from top to bottom).

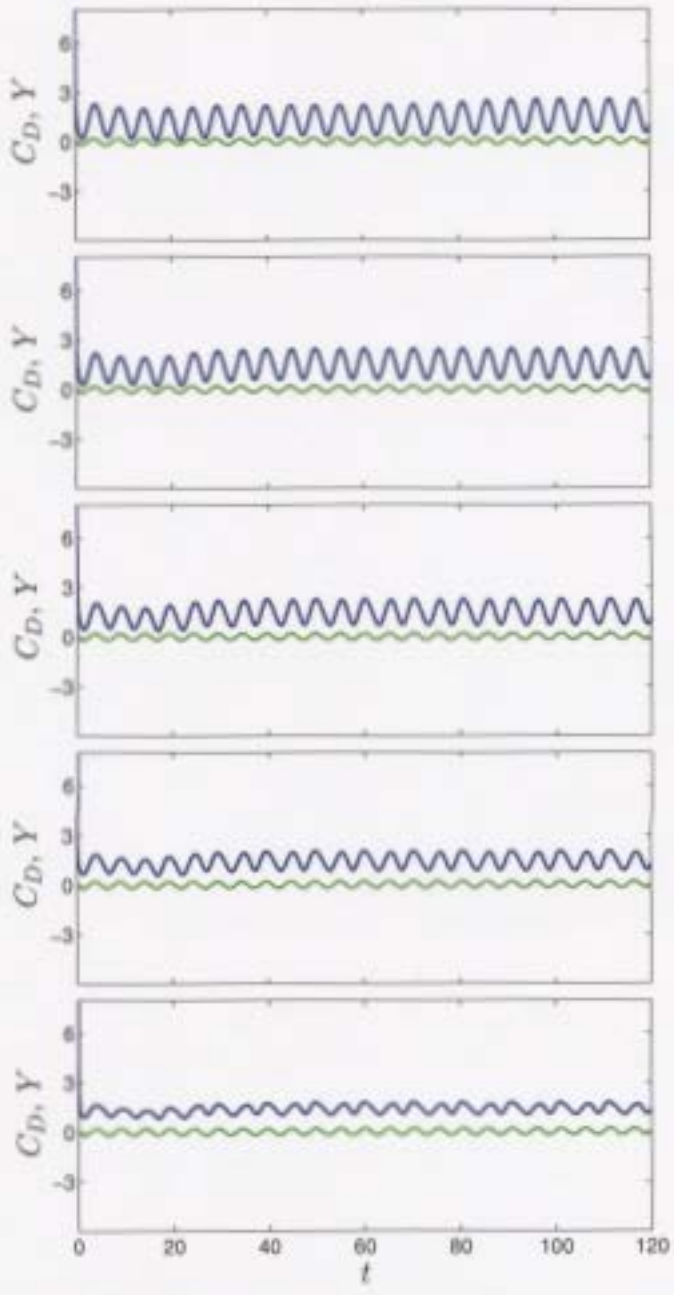

Figure 5.25: Drag coefficient (—) and cylinder displacement (—) for $R = 200$, $A = 0.2$, $S_f/S_0 = 2.0$ for angles of oscillation $\eta = 15°$, $30°$, $45°$, $60°$ and $75°$ (from top to bottom).

that the effect of the angle at $S_f/S_0 = 2.0$ is to increase the maximum lift coefficient and amplitude of the lift coefficient while decreasing the amplitude of the drag coefficient. Also, in general, the average drag coefficient decreases with increasing angle.

As a final note on the fluid forces at this amplitude, we note that a repeated pattern of two local maxima in the lift develops with the increase of the angle and each of these maxima occur when the cylinder is at its maximum positive displacement (position G, position O). As the angle of oscillation increases, the smaller of the two local maxima increases as an implicit consequence of the increased vortex formation length which is tabulated in Table 5.7. With the concentration of vorticity moving

	Formation Length
η \ S_f/S_0	2.0
15°	2.09
30°	2.19
45°	2.22
60°	2.26
75°	2.27

Table 5.7: Horizontal location of vortex behind cylinder for $R = 200$, $A = 0.2$, $S_f/S_0 = 2.0$ when cylinder is at the origin moving downward (position A).

further away from the surface on one side of the cylinder, the developing vortex on other side of the cylinder plays a larger role in the calculation of the lift coefficient. This growing difference in the magnitude of the vorticity at the surface of the cylinder causes an increase of the smaller maxima in the lift coefficient.

Although the timing of vortex shedding is not altered by the angle of oscillation at larger forcing frequencies, the effect of the angle on the near wake vortex shedding mode is amplified greatly. The vorticity contours over two periods of oscillation from position A to Q are given in Figure 5.26 for $A = 0.6$ and $15° \leq \eta \leq 75°$. For $\eta = 15°$, we see that the pattern of vortex shedding is nearly symmetric about the

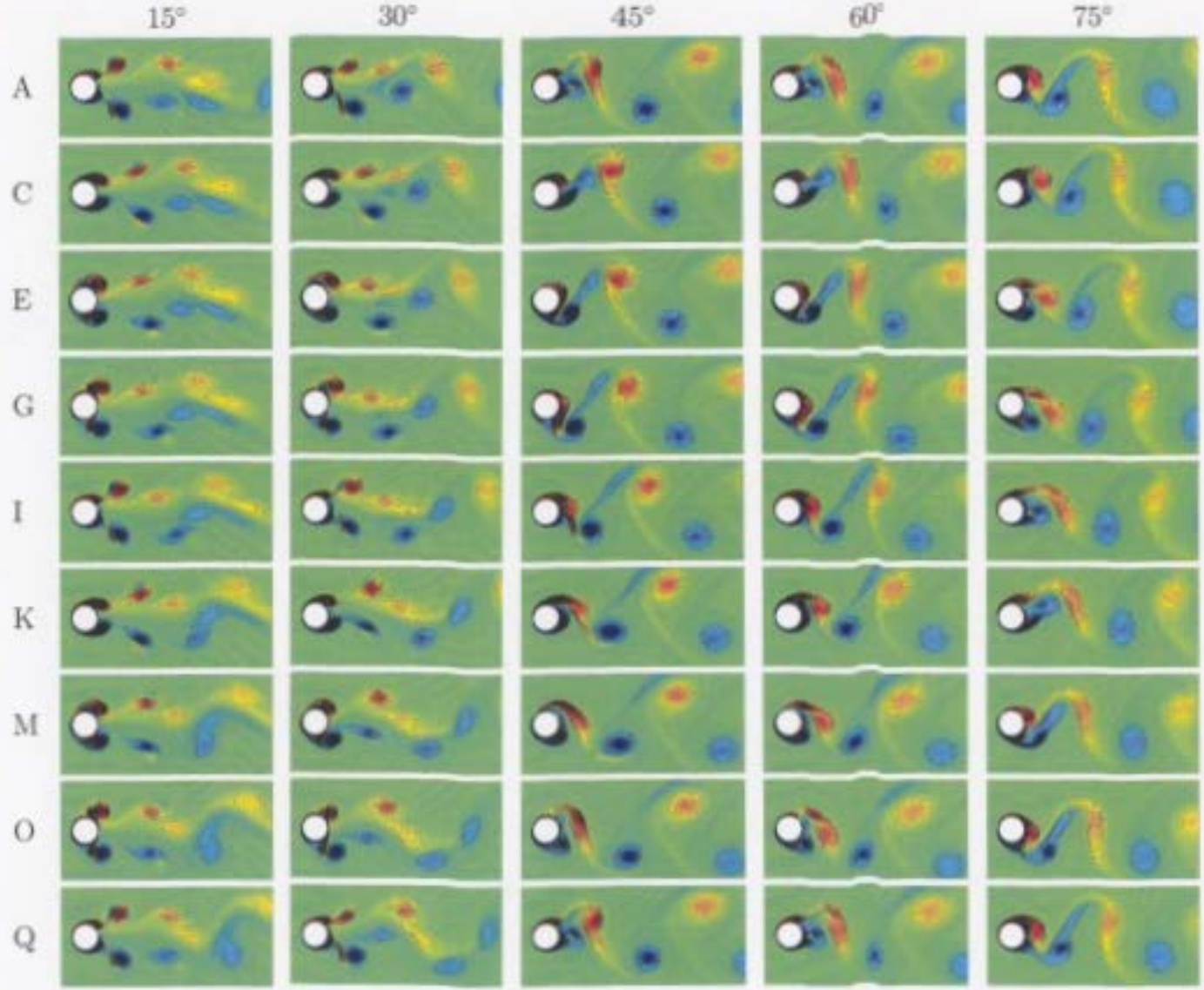

Figure 5.26: Vorticity contours for $R = 200$, $S_f/S_0 = 2.0$, $A = 0.6$ with η = 15°, 30°, 45°, 60°, and 75° over two periods of cylinder oscillation [$T = 5.12$, $81.88 \leq t \leq 92.12$].

x-axis and is repeated over T, not $2T$. As we increase the angle to 30° we observe that the near wake region is rapidly loosing its symmetry as the horizontal spacing between shedding vortices increases. At $\eta = 45°$ the wake has lost all its symmetry and the period of vortex shedding has doubled to $2T$. A complete record of vortex shedding modes and periods of oscillation is recorded in Table 5.8 for $S_f/S_0 = 2.0$ and $A = 0.6$, where we observe a transition from a nearly symmetric $2S^*_+$ mode to

η \ A	0.6
15°	$2S^*_+$[T]
30°	2S*[2T]
45°	P+S[2T]
60°	P+S[2T]
75°	2S[2T]

Table 5.8: Dominant modes and periods of vortex formation in the near wake for $R = 200$, $S_f/S_0 = 2.0$, $A = 0.6$, and $\eta = 15°$, 30°, 45°, 60°, 75°.

the asymmetric P+S and 2S modes. The +-subscript indicates that smaller vortices accompany the larger vortices when shed, but do not develop individually as seen in Figure 5.8 for $\eta = 15°$. This near symmetry is also suggested by the smallest amplitude lift coefficient at $\eta = 15°$ in Figure 5.27 This corresponding power spectra in this figure shows one dominant peak in the spectra representing the forcing frequency along with other smaller peaks which are not as significant; an observation that also indicates a locked-on state. Using the fluid forces given in Figures 5.27-5.28 we are then able to calculate several flow quantities which are recorded in Table 5.9. The

η	15°	30°	45°	60°	75°
$\bar{C}_D$	1.30	1.37	1.59	1.71	1.81
$C_{L,\max}$	0.90	1.75	2.98	3.88	4.20
$AMP(C_D)$	5.78	5.28	4.69	3.80	2.49
$AMP(C_L)$	2.18	4.16	6.26	7.69	8.20

Table 5.9: Average drag $\bar{C}_D$, maximum lift, and amplitude $AMP(\cdot)$ of drag and lift coefficients for $R = 200$, $A = 0.6$, $S_f/S_0 = 2.0$ when $15° \leq \eta \leq 75°$.

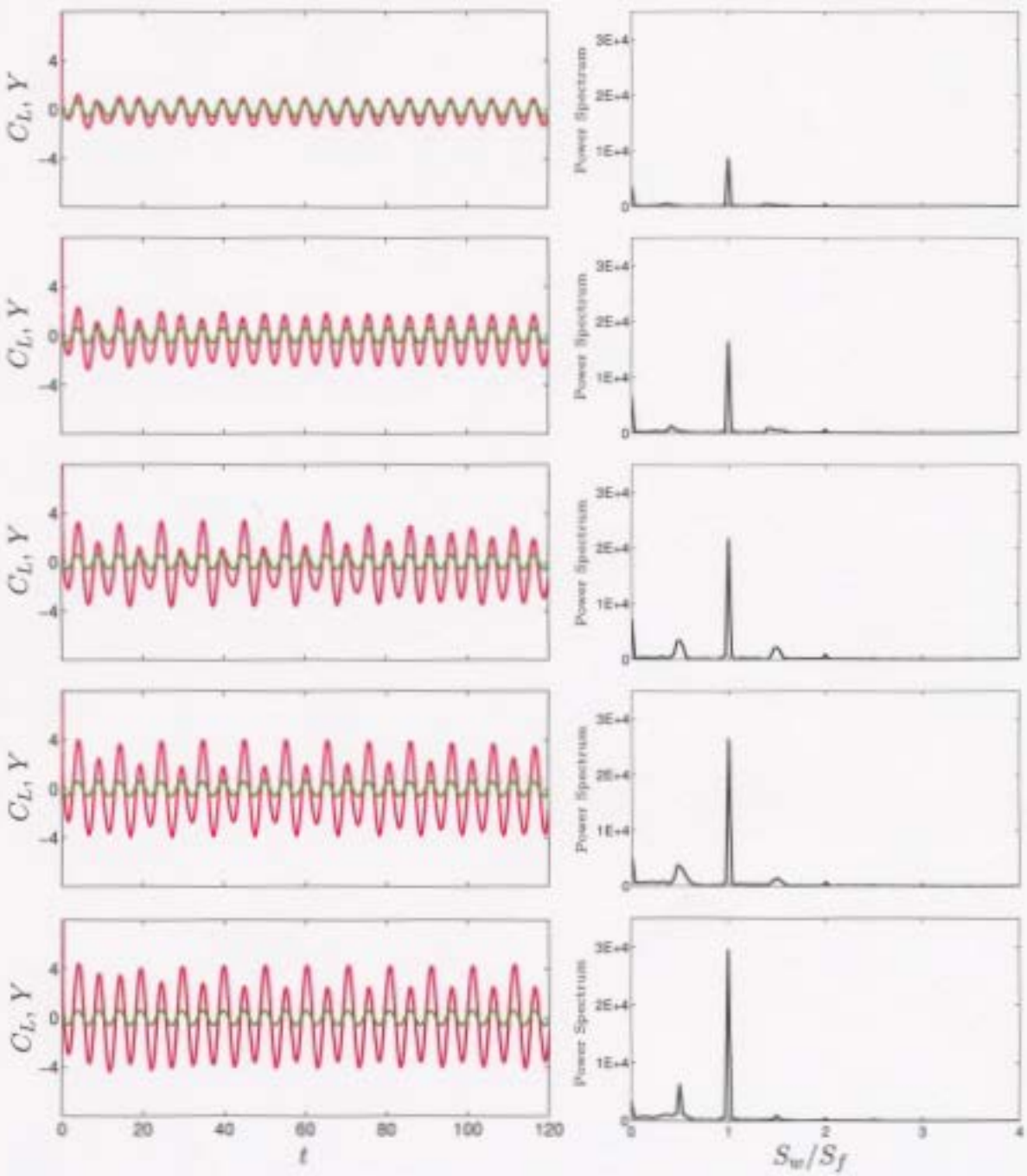

Figure 5.27: Lift coefficient (—) and cylinder displacement (—) with power spectrum of lift coefficient (right) for $R = 200$, $A = 0.6$, $S_f/S_0 = 2.0$ for angles of oscillation $\eta = 15°$, $30°$, $45°$, $60°$ and $75°$ (from top to bottom).

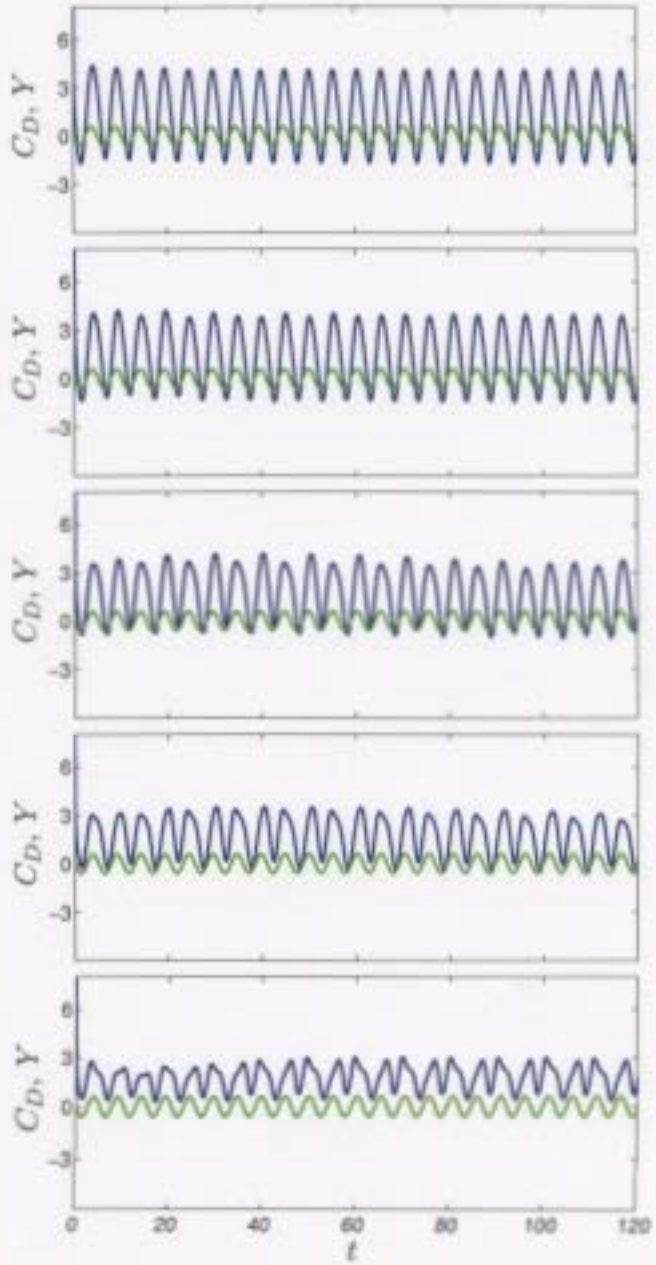

Figure 5.28: Drag coefficient (—) and cylinder displacement (—) for $R = 200$, $A = 0.6$, $S_f/S_0 = 2.0$ for angles of oscillation $\eta = 15°$, $30°$, $45°$, $60°$ and $75°$ (from top to bottom).

forces are characterized by an increasing average drag and maximum lift coefficient. However, the amplitudes of drag curve is decreasing whereas an increase in the lift coefficient amplitude is observed.

5.4 Effect of the oscillation amplitude on vortex modes and force coefficients when $R = 200$ and $15° \leq \eta \leq 75°$

In this section, we focus on how the flow characteristics change with increasing amplitude for $A = 0.2$, 0.6, and 1.0 at $R = 200$. At $S_f/S_0 = 0.5$ and 1.0 the increasing amplitude of oscillation did not play a significant role in the modification of the near wake flow features. All effects that were observed have been reported in Sections 4.1-4.2. At $S_f/S_0 = 2.0$, however, the amplitude is very important in determining the nature of the near wake structure. To better illustrate this we consider again $S_f/S_0 = 2.0$ and vary the amplitude from $A = 0.2$ to 1.0 for $15° \leq \eta \leq 75°$.

The vorticity contours over two periods, $2T$, of oscillation from position A to Q as the amplitude increases from $A = 0.2$ to $A = 0.6$ and finally to $A = 1.0$ are given in Figures 5.29-5.31 for $\eta = 15°$, 45°, and 75°, respectively. In each of these figures we plot the vorticity contours for increasing amplitude for a fixed angle in order to determine how the amplitude changes the vortex shedding patterns at this frequency. First, Figure 5.29 gives the contours for $\eta = 15°$. At $A = 0.2$, the contours display an asymmetric $2S$ mode of vortex shedding. However, with the increase of the amplitude to $A = 0.6$, the symmetric-like mode $2S^*_+$ is observed in the near wake. This symmetry is amplified even more when we increase A to 1.0. Note that for this largest amplitude at $\eta = 15°$, not only do the vortices shed at nearly the same instant, but

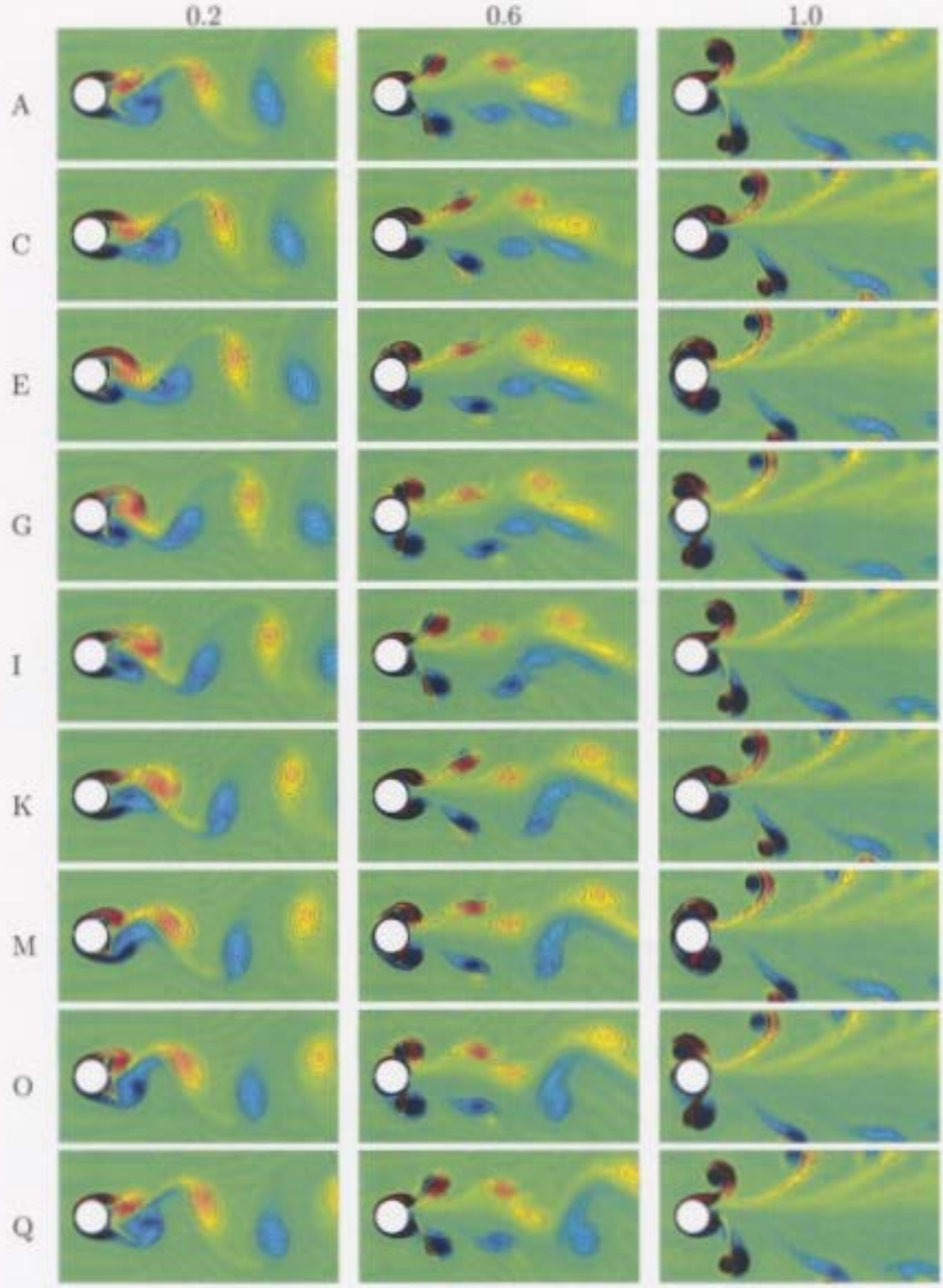

Figure 5.29: Equi-vorticity contours for $R = 200$, $S_f/S_0 = 2.0$, $\eta = 15°$ and amplitudes $A = 0.2$, 0.6, and 1.0 [$T = 5.12$, $81.88 \leq t \leq 92.12$].

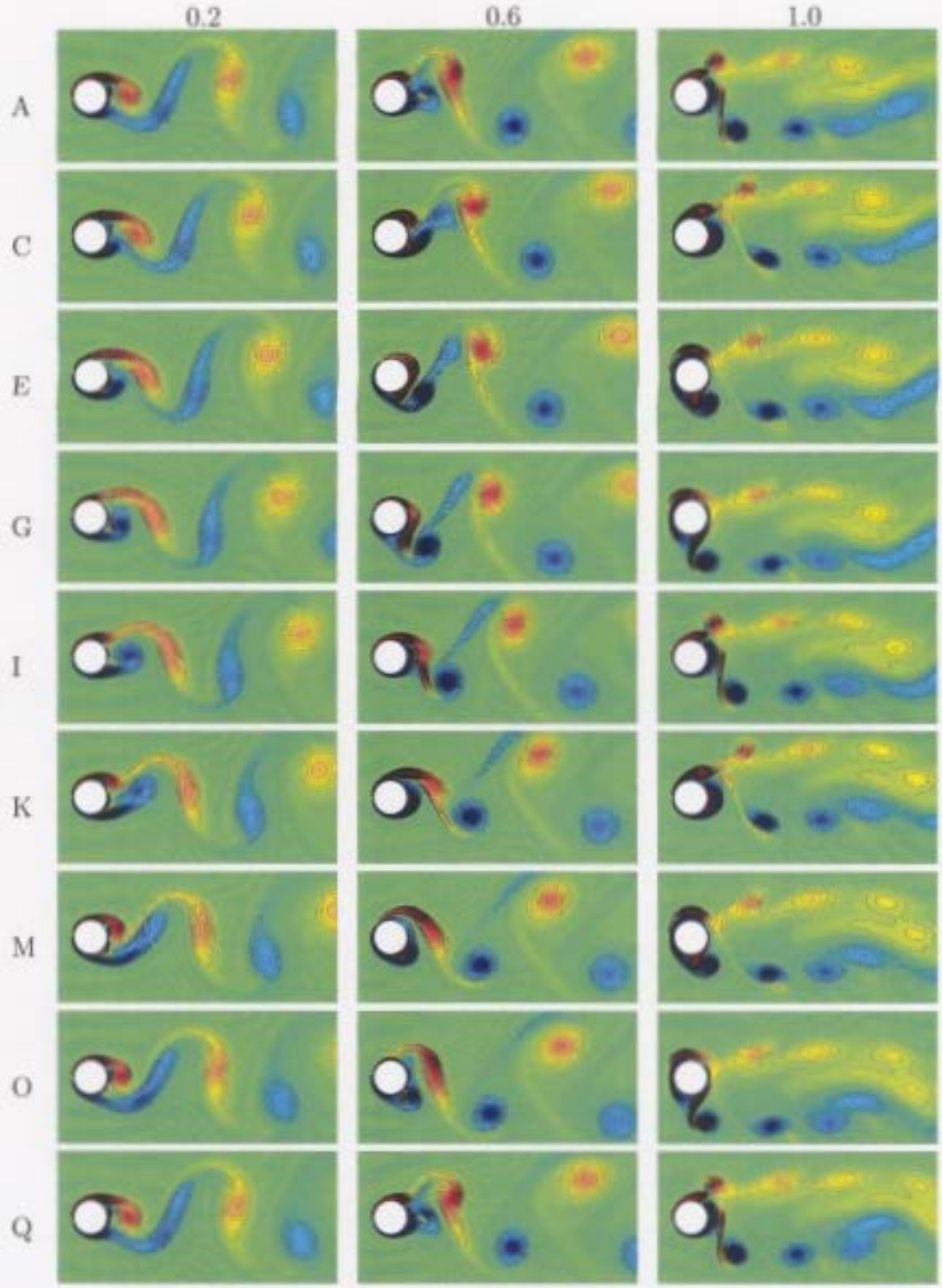

Figure 5.30: Equi-vorticity contours for $R = 200$, $S_f/S_0 = 2.0$, $\eta = 45°$ and amplitudes $A = 0.2$, 0.6, and 1.0 [$T = 5.12$, $81.88 \leq t \leq 92.12$].

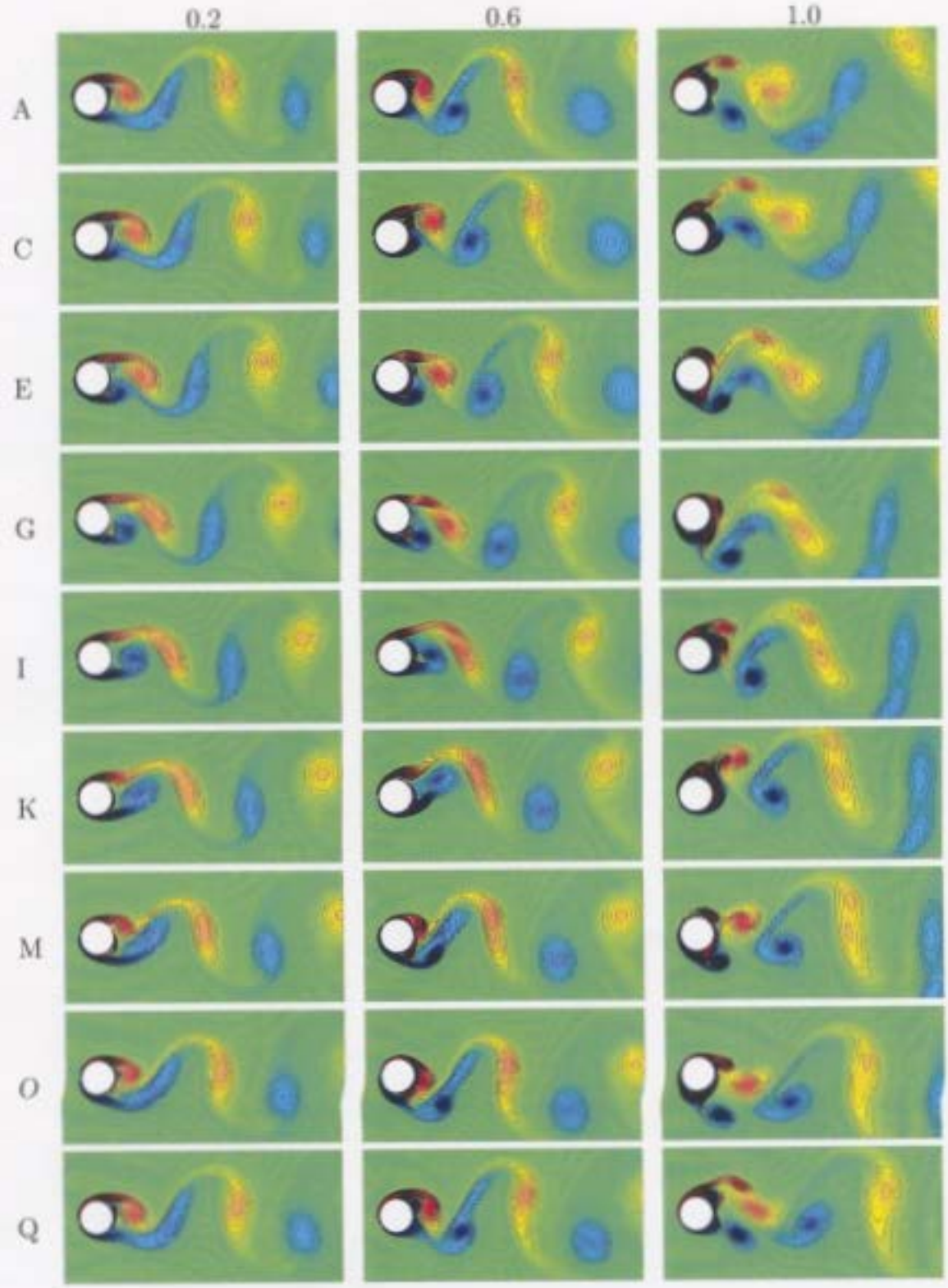

Figure 5.31: Equi-vorticity contours for $R = 200$, $S_f/S_0 = 2.0$, $\eta = 75°$ and amplitudes $A = 0.2$, 0.6, and 1.0 [$T = 5.12$, $81.88 \leq t \leq 92.12$].

this alignment of the vortices persists downstream of the cylinder. Also, the period of vortex shedding changes from $2T$ at $A = 0.2$ to T at $A = 0.6$ and 1.0.

Increasing the angle slightly to $\eta = 45°$ we obtain the equi-vorticity contours in Figure 5.30 where a symmetric-like mode is observed, but not at an amplitude of $A = 0.6$. At the smallest amplitude, $A = 0.2$, the 2S mode persists in the near wake over two periods, $2T$, of cylinder oscillation. A dramatic difference in the wake is then observed when the vorticity contours are compared to those for $A = 0.6$. During the formation of the vortex on the top of the cylinder we see that at location G the vortex completely engulfs the rear side of the cylinder. This is obviously caused by the fact that the increased upward motion of the cylinder is intruding on the location of the forming vortex. The vortex forming on the top of the cylinder then sheds in the second period of oscillation. During this first period, however, the vortex developing on the bottom of the cylinder is being pushed away from the cylinder surface towards the vortex which was shed from the top in the previous shedding period. The strong interaction of these two vortices causes a weak vortex to break away from the lower vortex which then accompanies the upper vortex downstream yielding the asymmetric P+S mode of vortex shedding. Finally, then, at $A = 1.0$ the symmetric-like 2S* mode is observed. The transition to this mode of vortex shedding occurs at a larger amplitude in this case because of the increase angle of oscillation. The period of vortex shedding is $2T$ for $A = 0.2$ and 0.6 but only T for $A = 1.0$.

At $\eta = 75°$ the wake is completely asymmetric for all the amplitudes considered in this thesis as shown in Figure 5.31. The 2S mode persists in the wake for all amplitudes over two periods, $2T$, of cylinder oscillation.

Hence, increasing the amplitude of oscillation at a fixed angle will create a natural transition to a symmetric mode. At smaller angles, this symmetric mode appears at lower values of the amplitude due to the reduced asymmetrical movement of the

cylinder. Then, as the angle increases, the threshold amplitude required for the observance of this symmetric mode increases. However, there is also a threshold angle for which no symmetry will be observed as suggested by the results for $\eta = 75°$. The key observation is that there is an undetermined boundary in the (A, η)-plane which divides the near wake into symmetrical and asymmetrical form. The determination of this boundary requires a simulations for a finer interval spacing in the parameter range and is beyond the scope of this thesis.

The complete classification of periods and modes of vortex formation in the near wake for the various angles, amplitudes, and frequencies discussed in this thesis are summarized in Table 5.10. Recall that the 2S* refers to a symmetric-like mode where the vortices are shed at nearly the same instant and the +-subscript on the mode indicates a smaller insignificant vortex is attached to the larger shedding vortex. This smaller vortex decays rapidly as the two vortices move away from the cylinder surface.

Several key observations can be made from the data in Table 5.10. First, for the lowest values of the amplitude and frequency, the 2S mode of vortex formation persists in the near wake for all angles but with different periods. For $S_f/S_0 = 0.5, 1.0,$ and 2.0 the periods of vortex shedding are approximately $T/2$, T, and $2T$, respectively. The doubling of the period of vortex shedding from $S_f/S_0 = 0.5$ to 1.0 is a result of the fact that the wake is controlled by natural shedding frequency and not the forcing frequency at $S_f/S_0 = 0.5$. However, the doubling of the period from T to $2T$ at $S_f/S_0 = 2.0$ results from the competition of the fundamental (S_0) and forcing ($S_f = 2S_0$) frequencies. This phenomenon is referred to as period doubling. Notice that for $\eta \leq 60°$, this period doubling phenomenon has been eliminated as the amplitude of oscillation is increased to $A = 1.0$. At smaller angles ($\eta = 15°$ and $30°$), it was eliminated at even smaller amplitudes. This phenomenon is explained by considering the magnitude of asymmetrical cylinder movement. Since the angles are smaller, the vertical displacement of the cylinder, $Y(t)\sin(\eta)$, from the origin is

S_f/S_0 \ A	0.2	0.6	1.0
	$\eta = 15°$		
0.5	2S $[T/2]$	2S $[T/2]$	2S $[T/2]$
1.0	2S $[T]$	2S $[T]$	2S* $[T]$
2.0	2S $[2T]$	$2S^*_+$ $[T]$	$2S^*_+$ $[T]$
	$\eta = 30°$		
0.5	2S $[T/2]$	2S $[T/2]$	2S $[T/2]$
1.0	2S $[T]$	2S $[T]$	2S* $[T]$
2.0	2S $[2T]$	2S* $[2T]$	$2S^*_+$ $[T]$
	$\eta = 45°$		
0.5	2S $[T/2]$	2S $[T/2]$	2S $[T/2]$
1.0	2S $[T]$	2S $[T]$	2S $[T]$
2.0	2S $[2T]$	P+S $[2T]$	2S* $[T]$
	$\eta = 60°$		
0.5	2S $[T/2]$	2S $[T/2]$	2S $[T/2]$
1.0	2S $[T]$	2S $[T]$	2S $[T]$
2.0	2S $[2T]$	P+S $[2T]$	2S $[T]$
	$\eta = 75°$		
0.5	2S $[T/2]$	2S $[T/2]$	2S $[T/2]$
1.0	2S $[T]$	2S $[T]$	2S $[T]$
2.0	2S $[2T]$	2S $[2T]$	2S $[2T]$

Table 5.10: Dominant modes and periods of vortex formation in the near wake for $R = 200$, $\eta = 15°$, $30°$, $45°$, $60°$, $75°$, $A = 0.2$, 0.6, 1.0, and $S_f/S_0 = 0.5$, 1.0, 2.0.

less than it is at higher angles. Thus, the transition to the symmetric-like 2S* mode occurs at smaller amplitudes.

Chapter 6

Summary and Conclusions

The flow of a viscous incompressible fluid past a cylinder performing oblique rectilinear oscillations has been investigated in this thesis. The model, described by the two-dimensional non-linear Navier-Stokes equations in vorticity-stream function form, was solved numerically using a finite difference method with implicit Crank Nicholson time-stepping. The numerical method is an extension of the work by Collins and Dennis (1973b) and Badr and Dennis (1985). At small times, a series expansion solution is obtained numerically following the work of Collins and Dennis (1973a) which is then used to verify the accuracy of the numerical scheme in the initial stages of motion. Modifications to the numerical method were introduced by way of parallel computations which showed computational improvement at a fairly minimal cost. By switching to the slower converging Gauss-Jacobi iterative scheme, execution times decreased by a factor of nearly seven on just eight processors. In a practical sense, the parallel implementation of the code has reduced the execution time from approximately 3.8 days (for $\eta = 45°$, $A = 0.2$, $S_f/S_0 = 2.0$, $0 \leq t \leq 300$) to approximately 15 hours. In addition, a maximum increase of only a single iteration was observed after the change of iterative schemes. Thus, performing computations in parallel were extremely effective in improving the algorithm.

To verify the accuracy of the algorithm, simulations to produce comparisons with

previous experimental findings and numerical results using alternate schemes were conducted. At both small and large values of the time the results indicate good qualitative agreement. In particular, verification of recti-linear oscillations of a circular cylinder at $\eta = 0°$ and $\eta = 90°$ to the oncoming uniform stream, the most extensively studied cases to date, were conducted. The experimental study of Ongoren and Rockwell (1988b) served as a comparison for the case of a cylinder performing oblique oscillations at $\eta = 45°$.

The flow properties for an obliquely oscillated circular cylinder were then studied at a Reynolds number of $R = 200$. One of the main objectives was to address the phenomenon of lock-on for oscillations performed at $\eta = 45°$ to the oncoming flow. The power spectra of the lift coefficient and isolines in the near wake were used as a means of lock-on determination. Lock-on was observed in the fundamental and 2-superharmonic excitation regimes for $0.92 \leq S_f/S_0 \leq 1.02$ and $1.5 \leq S_f/S_0 \leq 2.06$, respectively, when $\eta = 45°$ and $A = 0.5$ whereas no sub-harmonic lock-on in the near wake was observed. Another superharmonic excitation regime near $S_f/S_0 = 3.0$ was determined to be locked-on to the cylinder oscillation frequency, but precise bounds could not be calculated due to the complexity of the near wake structure. At lower values of the frequency $S_f/S_0 \leq 1.2$, the asymmetric 2S mode of vortex shedding dominated the near wake. As the frequency increased to $S_f/S_0 \geq 1.5$, the P+S mode persisted. However, through the 2-superharmonic lock-on range the asymmetric mode changed from P+S for $1.5 \leq S_f/S_0 \leq 1.8$ to 2P at $S_f/S_0 = 1.9$ and then back to P+S at $S_f/S_0 = 2.0$. Hence, the frequency of oscillation was important in determining the structure of the near wake.

The second major focus of the results was on determining the effect of the angle and amplitude of oscillation on the near wake structure and flow properties. At $S_f/S_0 = 0.5$, since the near wake was still dominated by the natural shedding frequency, the varying amplitude and angle did not display a large effect. At

$S_f/S_0 = 1.0$, the increasing angle led to the lock-on of the vortex shedding, with no lock-on at smaller angles. This observation suggested that there was a transition from the existence of the previously confirmed fundamental lock-on regime at $\eta = 90°$ to the non-existence of the regime at $\eta = 0°$. Moreover, the lengthening of the vortex formation length at $A = 0.2$, $S_f/S_0 = 1.0$ resulted in the shedding of vortices at opposite times in the cylinder oscillation period at small, $\eta = 15°$, and large, $\eta = 75°$, values of the angle of oscillation. The time between shed vortices was decreased, however, as the amplitude of oscillation increased. In addition, increasing the amplitude of oscillation to $A = 1.0$ resulted in a faster generation of vorticity from the surface of the cylinder and thus a decreasing vortex formation length. For the most extreme angle considered in this thesis, $\eta = 75°$, a phenomenon similar to switching, which was observed during the fundamental excitation regime for transverse oscillations with increasing frequency, was noted. However, the combination of the increased angle and amplitude of oscillation caused the switching in this case, not the frequency variation.

At higher values of the frequency, $S_f/S_0 = 2.0$, the amplitude of oscillation had a larger effect on the near wake flow properties. At this frequency, we observed a transition from an asymmetric arrangement of vortices in the near wake to a symmetric-like arrangement, denoted 2S*. At smaller angles the symmetry was observed at smaller amplitudes. As the angle was increased, a larger amplitude was required in order for this symmetric-like mode of vortex shedding to develop. For this mode, the vortices shed during one cycle are not staggered, as before, but aligned almost vertically, which is characteristic of a symmetric wake. As a result of the tendency to a symmetric mode, the period doubling phenomenon was also suppressed. That is, the period of vortex shedding cycle was reduced from two periods, $2T$, of cylinder oscillation to a single period, T, of oscillation.

In this thesis, the results were shown to be in good agreement with a small-time

series expansion, and previous numerical and experimental findings for fixed and oscillating cylinders. The method works well in capturing the important boundary-layer development of the flow, especially for large values of the Reynolds number. Consequently, it was extremely effective in resolving the near wake flow characteristics for the case of an obliquely oscillating circular cylinder.

Appendix A. The governing equations in the non-inertial frame of reference

The continuum equations governing the flow are the unsteady incompressible Navier-Stokes equations together with the continuity equation given by

$$\frac{\partial \mathbf{v}_I^*}{\partial t^*} + (\mathbf{v}_I^* \cdot \nabla)\mathbf{v}_I^* = -\frac{1}{\rho}\nabla \mathbf{p}^* + \nu \nabla^2 \mathbf{v}_I^* \tag{A.1}$$

$$\nabla \cdot \mathbf{v}_I^* = 0, \tag{A.2}$$

in cylindrical $(r^*,\ \theta, z^*)$ coordinates where $\mathbf{v}_I$ is the velocity in the inertial or lab frame of reference defined as

$$\mathbf{v}_I^* = u_I^*\, \mathbf{e}_{r^*} + v_I^*\, \mathbf{e}_\theta + (0)\, \mathbf{e}_{z^*} = (u_I^*,\ v_I^*,\ 0),$$

$\mathbf{p}^*$ is the pressure, and ρ and ν are constants representing the density and kinematic viscosity of a particular fluid.

For convenience in this analysis, we choose to use a non-inertial frame of reference which is fixed with the cylinder translation and oscillation. Mathematically, to introduce this non-inertial reference frame we define the velocity of a fluid particle in the stationary frame $\mathbf{v}_I^*$ as

$$\mathbf{v}_I^* = \mathbf{v}^* + \mathbf{v}_{NI}^* \tag{A.3}$$

where $\mathbf{v}^*$ is the velocity of a fluid particle in the moving frame and $\mathbf{v}^*_{NI}$ is the velocity of the moving frame defined as

$$\mathbf{v}^*_{NI} = \begin{bmatrix} u^*_{NI} \\ v^*_{NI} \end{bmatrix} = \begin{bmatrix} -(U + V^*(t^*)\cos(\eta))\cos(\theta) - V^*(t^*)\sin(\eta)\sin(\theta) \\ (U + V^*(t^*)\cos(\eta))\sin(\theta) - V^*(t^*)\sin(\eta)\cos(\theta) \end{bmatrix}. \quad \text{(A.4)}$$

Here we have used the relationship between the Cartesian and polar unit vectors that

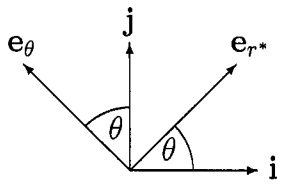

Figure A.1: Relationship between coordinate unit vectors.

$$\begin{aligned} \mathbf{e}_{r^*} &= \cos(\theta)\mathbf{i} + \sin(\theta)\mathbf{j} \\ \mathbf{e}_\theta &= -\sin(\theta)\mathbf{i} + \cos(\theta)\mathbf{j}. \end{aligned}$$

as seen in Figure A.1. Through this definition, we introduce the forced oscillations into our equations so that downward motion along the axis of oscillation corresponds to positive U_m, with the maximum velocity attained as the cylinder travels downward through the origin at $t = 0$ and every full cycle thereafter. Substituting the expressions contained in (A.3) and (A.4) into equations (A.1)-(A.2) yields in the non-inertial frame of reference

$$\frac{\partial \mathbf{v}^*}{\partial t^*} + (\mathbf{v}^* \cdot \nabla)\mathbf{v}^* = -\frac{1}{\rho}\nabla \mathbf{p}^* + \nu \nabla^2 \mathbf{v}^* + \mathbf{a}^* \quad \text{(A.5)}$$

$$\nabla \cdot \mathbf{v}^* = 0, \quad \text{(A.6)}$$

where

$$\mathbf{a}^* = \begin{bmatrix} a^*_r \\ a^*_\theta \end{bmatrix} = \begin{bmatrix} \dot{V}^*(t^*)\cos(\eta)\cos(\theta) + \dot{V}^*(t^*)\sin(\eta)\sin(\theta) \\ -\dot{V}^*(t^*)\cos(\eta)\sin(\theta) + \dot{V}^*(t^*)\sin(\eta)\cos(\theta) \end{bmatrix}$$

Appendix B. Tri-diagonal matrix algorithm (TDMA)

We are given the $N \times N$ tri-diagonal matrix equation

$$\mathbf{Ax} = \mathbf{b}$$

which has vectors α, β, and γ along the lower, main, and upper diagonals (with elements α_i, β_i, and γ_i). To reduce this equation to bi-diagonal form we implement the following procedure:

```
Set Λ_0 = 0 and Π_0 = x_0
for i = 1 : N − 1
    Λ_i = −γ_i/(α_i + β_i Λ_{i−1})
    Π_i = (b_i − β_i Π_{i−1})/(α_i + β_i Λ_{i−1})
end
```

using the convention that $\alpha_N = 0$. Then, we solve using back-substitution, or

```
for i = N − 1 : 1
    x_i = Λ_i x_{i+1} + Π_i
end
```

since we know that $x_N = \Pi_N$.

Appendix C. Composite integration formula

Assuming that a function $f(x)$ is defined at a set of discrete grid points $x_0 \leq x_1 \leq x_2 \leq \cdots \leq x_M \leq x_{M+1}$, to perform the integration

$$I = \int_{x_i}^{x_j} f(x)dx$$

we may use the following algorithm:

(1) *If* $[(j-i) \bmod 6] = 1$

$$I = \frac{h}{24}(9f_i + 19f_{i+1} - 5f_{i+2} + f_{i+3})$$

Add 1 to i

Else if $[(j-i) \bmod 6] = 2$

$$I = \frac{h}{3}(f_i + 4f_{i+1} + f_{i+2})$$

Add 2 to i

Else if $[(j-i) \bmod 6] = 3$

$$I = \frac{3h}{8}(f_i + 3f_{i+1} + 3f_{i+2} + f_{i+3})$$

Add 3 to i

Else if $[(j-i) \bmod 6] = 4$

$$I = \frac{2h}{45}(7f_i + 32f_{i+1} + 12f_{i+2} + 32f_{i+3} + 7f_{i+4})$$

Add 4 to i

Else $[(j-i) \bmod 6] = 5$

$$I = \frac{h}{24}\left(9f_i + 27f_{i+1} + 27f_{i+2} + 9f_{i+3} + 8f_{i+4} + 24f_{i+5} + 8f_{i+6}\right)$$

Add 5 to i

(2) *For l from i to $j-1$ by 6*

$$I = I + \frac{3h}{10}\left(f_l + 5f_{l+1} + f_{l+2} + 6f_{l+3} + f_{l+4} + 5f_{l+5} + f_{l+6}\right).$$

Appendix D. Summation terms - small-time series solution

The summation terms, X_n and Y_n, used in equations (2.5.5)-(2.5.6) are

$$X_n = \sum_{m=0}^{j-1} \sum_{s} 2s \sum_{r} \sum_{p=0}^{i} \left[A_1 \left(f_s^{(p,m)} \frac{dg_n^{(i-p,j-m-1)}}{dx} - g_s^{(p,m)} \frac{df_n^{(i-p,j-m-1)}}{dx} \right) \right.$$
$$\left. + A_2 \left(F_s^{(p,m)} \frac{dG_n^{(i-p,j-m-1)}}{dx} - G_s^{(p,m)} \frac{dF_n^{(i-p,j-m-1)}}{dx} \right) \right]$$
$$+ 2 \sum_{p=0}^{i-1} \frac{(2x)^{i-p}}{(i-p)!} \left\{ [2j+p-1] g_n^{(p,j)} - x \frac{dg_n^{(p,j)}}{dx} \right\}$$

$$Y_n = \sum_{m=0}^{j-1} \sum_{s} 2s \sum_{r} \sum_{p=0}^{i} \left[A_3 \left(f_s^{(p,m)} \frac{dG_n^{(i-p,j-m-1)}}{dx} - g_s^{(p,m)} \frac{dF_n^{(i-p,j-m-1)}}{dx} \right) \right.$$
$$\left. + A_4 \left(F_s^{(p,m)} \frac{dg_n^{(i-p,j-m-1)}}{dx} - G_s^{(p,m)} \frac{df_n^{(i-p,j-m-1)}}{dx} \right) \right]$$
$$+ 2 \sum_{p=0}^{i-1} \frac{(2x)^{i-p}}{(i-p)!} \left\{ [2j+p-1] G_n^{(p,j)} - x \frac{dg_n^{(p,j)}}{dx} \right\}$$

where a negative superscript indicates a zero function and the subscript n ranges over the values

$$n = 1, 3, 5, ..., j+1 \quad , \quad \text{for } j \text{ even},$$
$$n = 2, 4, 6, ..., j+1 \quad , \quad \text{for } j \text{ odd}.$$

The summation of s extends over the values

$$s = 1, 3, 5, ..., m+1 \quad , \quad \text{for } m \text{ even},$$
$$s = 2, 4, 6, ..., m+1 \quad , \quad \text{for } m \text{ odd}.$$

and the summation over r is defined by

$$\begin{aligned} r &= n+s, n-s && \text{for } s-n < 1, \\ r &= n+s, s-n && \text{for } s-n \geq 1, (1 \leq r \leq j-m) \\ r &= 2n && \text{for } s = n, \end{aligned}$$

with

$$A_1 = \begin{cases} -1 & \text{for } r = s-n, \\ 1 & \text{otherwise.} \end{cases} \qquad A_2 = \begin{cases} -1 & \text{for } r = s-n \text{ or } r = n-s, \\ 1 & \text{otherwise.} \end{cases}$$

$$A_3 = \begin{cases} 1 & \text{for } r = n-s, \\ -1 & \text{otherwise.} \end{cases} \qquad A_4 = 1.$$

Bibliography

Anagnostopoulos, P. (1989). Numerical solution for laminar two-dimensional flow about a fixed and transversely oscillating cylinder in a uniform stream. *Journal of Computational Physics*, 85:434–456.

Anagnostopoulos, P. (1997). Computer-aided flow visualization and vorticity balance in the laminar wake of a circular cylinder. *Journal of Fluids and Structures*, 11:33–72.

Anagnostopoulos, P. (2000). Numerical study of the flow past a cylinder excited transversely to the incident stream. Part 1: Lock-in zone, hydrodynamic forces, and wake geometry. *Journal of Fluids and Structures*, 14:819–851.

Armstrong, B. J., Barnes, F. H., and Grant, I. (1986). The effect of a perturbation on the flow over a cylinder. *Physics of Fluids*, 29:2095–2102.

Armstrong, B. J., Barnes, F. H., and Grant, I. (1987). A comparison of the structure of the wake behind a circular cylinder in a steady flow with that in a perturbed flow. *Physics of Fluids*, 30:19–26.

Ascher, U. M., Mattheij, R. M. M., and Russell, R. D. (1995). *Numerical solution of boundary-value problems for ordinary differential equations.* SIAM, Philadelphea.

Badr, H. M. and Dennis, S. C. R. (1985). Unsteady flow past a rotating and translating circular cylinder. *Journal of Fluid Mechanics*, 158:447–488.

Badr, H. M., Dennis, S. C. R., and Kocabiyik, S. (1995). The initial oscillatory flow past a circular cylinder. *Journal of Engineering Mathematics*, 29:255–269.

Badr, H. M., Dennis, S. C. R., and Kocabiyik, S. (1996). Symmetrical flow past an

accelerated circular cylinder. *Journal of Fluid Mechanics*, 308:97–110.

Barbi, C., Favier, D. P., Maresca, C. A., and Telionis, D. P. (1986). Vortex shedding and lock-on of a circular cylinder in oscillatory flow. *Journal of Fluid Mechanics*, 170:527–544.

Blackburn, H. M. and Henderson, R. D. (1999). A study of two-dimensional flow past an oscillating cylinder. *Journal of Fluid Mechanics*, 385:255–286.

Cetiner, O. and Rockwell, D. (2001). Streamwise oscillations of a cylinder in a steady current. Part 1. Locked-on states of vortex formation and loading. *Journal of Fluid Mechanics*, 427:1–28.

Chang, C.-C. and Chern, R.-L. (1991). A numerical study of flow around an impulsively started circular cylinder by a deterministic vortex method. *Journal of Fluid Mechanics*, 233:243–263.

Cheng, M., Chew, T., and Luo, S. C. (1997). A hybrid vortex method for flows over a bluff body. *International Journal for Numerical Methods in Fluids*, 24:253.

Collins, W. M. (1973). PhD thesis, University of Western Ontario, London, Ontario, Canada.

Collins, W. M. and Dennis, S. C. R. (1973a). Flow past an impulsively started circular cylinder. *Journal of Fluid Mechanics*, 60:105–127.

Collins, W. M. and Dennis, S. C. R. (1973b). The initial flow past an impulsively started circular cylinder. *Quarterly Journal of Mechanics and Applied Mathematics*, 26:53–75.

Collins, W. M. and Dennis, S. C. R. (1974). Symmetrical flow past a uniformly accelerated circular cylinder. *Journal of Fluid Mechanics*, 65:461–480.

Dennis, S. C. R. and Chang, G. Z. (1969). Numerical integration of the Navier-Stokes equations, technical summary, report no. 859. *Mathematical Research Center, University of Wisconsin.*

Dennis, S. C. R., Nguyen, P., and Kocabiyik, S. (2000). The flow induced by a rotationally oscillating and translating circular cylinder. *Journal of Fluid Mechanics*,

407:123–144.

Dennis, S. C. R. and Quartapelle, L. (1989). Some uses of Green's theorem in solving the Navier-Stokes equations. *International Journal of Numerical Methods in Fluids*, 9:871–890.

Eaton, B. E. (1987). Analysis of laminar vortex shedding behind a circular cylinder by computer-aided flow visualization. *Journal of Fluid Mechanics*, 180:117–145.

Franke, R., Rodi, W., and Schoenung, B. (1990). Numerical calculation of laminar vortex-shedding flow past cylinders. *Journal of Wind Engineering and Industrial Aerodynamics*, 35:237–257.

Gresho, P. M., Lee, R. L., and Sani, R. L. (1980). *On the time-dependent solution of the incompressible Navier-Stokes equations in two and three dimensions in Recent Advances in Numerical Methods in Fluids.* Pineridge, Swansea.

Griffin, O. M. (1971). The unsteady wake of an oscillating cylinder at low reynolds number. *Journal of Applied Mechanics*, pages 729–738.

Griffin, O. M. and Hall, M. S. (1991). Review - vortex shedding lock-on and flow control in bluff body wakes. *Journal of Fluids Engineering*, 113:526–537.

Griffin, O. M. and Ramberg, S. E. (1974). The vortex street wakes of vibrating cylinders. *Journal of Fluid Mechanics*, 66:553–576.

Griffin, O. M. and Ramberg, S. E. (1976). Vortex shedding from a cylinder vibrating in line with an incident uniform flow. *Journal of Fluid Mechanics*, 75:257–271.

Guilmineau, E. and Queutey, P. (2002). A numerical simulation of vortex shedding from an oscillating circular cylinder. *Journal of Fluids and Structures*, 16:773–794.

Hall, M. S. and Griffin, O. M. (1993). Vortex shedding lock-on in a perturbed flow. *Journal of Fluids Engineering*, 115:283–291.

Henderson, R. D. (1997). Nonlinear dynamics and pattern formation in turbulent wake transition. *Journal of Fluid Mechanics*, 352:65–112.

Herfjord, K. (1995). *A study of two-dimensional separated flow by a combination of the finite element method and Navier-Stokes equations.* PhD thesis, The Norwegian

Institute of Technology, Trondheim, Norway.

Irvine, T. (2003). Tacoma narrows bridge failure revision A. Available at http://www.vibrationdata.com/Tacoma.htm.

Jordin, S. K. and Fromm, J. E. (1972). Oscillatory drag, lift, and torque on a circular cylinder in a uniform flow. *Physics of Fluids*, 15:371–376.

Kármán, T. von (1911). Über den Mechanismus des Widerstandes , den ein bewegter Körper in einer Flüssigkeiterfährt. *mathematik-physik*, K1:547.

Karniadakis, G. E. and Triantafyllou, G. S. (1989). Frequency selection and asymptotic states in laminar wakes. *Journal of Fluid Mechanics*, 199:441–469.

Kocabiyik, S. and Al-Mdallal, Q. (2003a). A numerical study on rectilinear oscillations of a circular cylinder. *Proceedings of the 2003 International Union of Theoretical and Applied Mechanics (IUTAM) Symposium on Integrated Modeling of Fully Coupled Fluid Structure Interactions Using Analysis, Computations, and Experiments (Eds: H. Benaroya and T. Wei)*, Kluwer Academic Publishers, 163-173.

Kocabiyik, S. and Al-Mdallal, Q. (2003b). Numerical simulation of laminar flow past an oscillating circular cylinder. *Proceedings of the 11th Annual Conference of the Computational Fluid Dynamics Society of Canada (CFDSC)*, Vancouver, British Columbia, 2:191-198.

Kocabiyik, S., Mahfouz, F. M., and Al-Mdallal, Q. (2004). Numerical simulation of the flow behind a circular cylinder subject to small-amplitude recti-linear oscillations. *Advances in Engineering Software (in press).*

Kocabiyik, S. and Nguyen, P. (1996). A finite difference calculation for a transverse superimposed oscillation. *Canadian Applied Mathematics Quarterly*, 4:97–107.

Kocabiyik, S. and Nguyen, P. (1999). On a translating and transversely oscillating cylinder. Part 2 - Effect of the velocity ratio on the hydrodynamic forces and the near-wake structure. *Ocean Engineering*, 26:21–45.

Koopman, G. H. (1967). The vortex wakes of vibrating cylinders at low reynolds numbers. *Journal of Fluid Mechanics*, 28:501–512.

Koumoutsakos, P. and Leonard, A. (1995). High resolution simulations of the flow around an impulsively started cylinder using vortex methods. *Journal of Fluid Mechanics*, 296:1.

Krishnamoorthy, S., Price, S. J., and Paidoussis, M. P. (2001). Cross-flow past an oscillating circular cylinder: synchronization phenomena in the near wake. *Journal of Fluids and Structures*, 15:955–980.

Li, L., Sherwin, S. J., and Bearman, P. W. (2002). A moving frame of reference algorithm for fluid/structure interaction of rotating and translating bodies. *International Journal for Numerical Methods in Fluids*, 38:187–206.

Lu, X.-Y. and Dalton, C. (1996). Calculation of the timing of vortex formation from an oscillating cylinder. *Journal of Fluids and Stuctures*, 10:527–541.

Matsumoto, M. (1999). Vortex shedding of bluff bodies: a review. *Journal of Fluids and Structures*, 13:791–811.

Meneghini, J. R. (1993). *Numerical simulation of bluff flow control using a discrete vortex method.* PhD thesis, University of London, England.

Nguyen, P. and Kocabiyik, S. (1997). On a translating and transversely oscillating cylinder. Part 1 - The effect of the Strouhal number on the hydrodynamic forces and the near-wake structure. *Ocean Engineering*, 24:677–693.

Ongoren, A. and Rockwell, D. (1988a). Flow structure from an oscillating cylinder Part 1. Mechanisms of phase shift and recovery in the near wake. *Journal of Fluid Mechanics*, 191:197–225.

Ongoren, A. and Rockwell, D. (1988b). Flow structure from an oscillating cylinder Part 2. Mode competition in the near wake. *Journal of Fluid Mechanics*, 191:225–245.

Panton, R. L. (1984). *Incompressible Flow.* John Wiley and Sons, New York.

Qian, L. and Vezza, M. (2001). A vorticity-based method for incompressible unsteady viscous flows. *Journal of Computational Physics*, 172:515–542.

Rengel, J. E. and Sphaier, S. H. (1999). A projection method for unsteady navier-stokes equations with finite volume method and collocated grid. *Hybrid Methods in Heat and Mass Transfer*, 1.

Sarpkaya, T. (1979). Vortex-induced oscillations. *Journal of Applied Mechanics*, 46:241–258.

Smith, S. L. and Brebbia, C. A. (1977). Improved stability techniques for the solution of Navier-Stokes equations. *Applied Mathematical Modelling*, 1:241–260.

Sphaier, S. H. (1991). Application of random vortex method for the computation of hydrodynamic forces about circular cylinders. XI Latin American Congress on Compuational Methods in Engineering, Rio de Janeiro, RJ, Brazil (in Portuguese).

Stojkovic, D., Breuer, M., and Durst, F. (2002). Effect of high rotation rates on laminar flow around a circular cylinder. *Physics of Fluids*, 14:3160–3178.

Strouhal, V. (1878). Uber eine besondere art der tonerregung. *Ann. Physik. Chem*, 5(10):216–251.

Sumer, B. M. and Fredsøe, J. (1997). *Hydrodynamics around cylindrical structures.* World Scientific, New York.

Swanson, J. C. and Spaulding, M. L. (1978). *Three dimensional numerical model of vortex shedding from a circular cylinder in Symposium on Non-Steady Fluid Dynamics.* ASME, New York.

Williamson, C. H. K. and Govardhan, R. (2004). Vortex-induced vibrations. *Annual Review of Fluid Mechanics*, 36:413–455.

Williamson, C. H. K. and Roshko, A. (1988). Vortex formation in the wake of an oscillating cylinder. *Journal of Fluids and Structures*, 2:355–381.